Aerodynamic modelling of open rotor-wing-flap interactions with low-fidelity methods

E.A. Ebbens

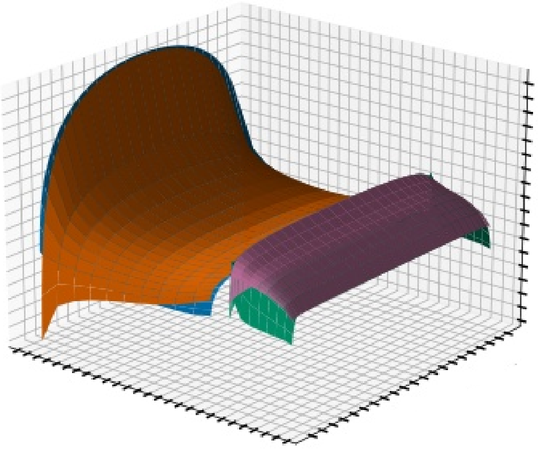

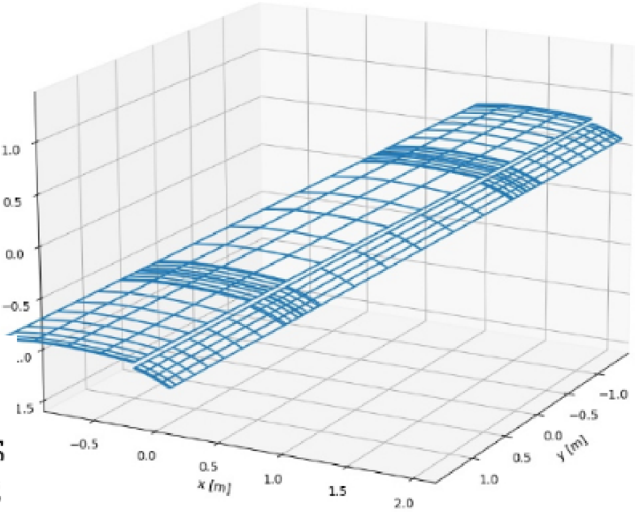

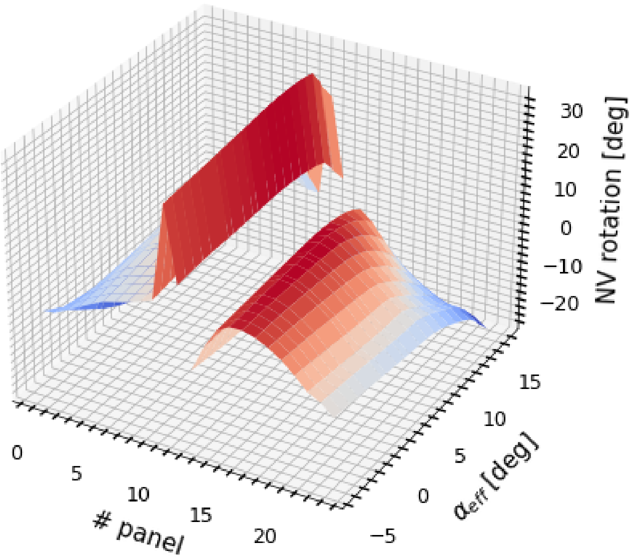

Aerodynamic modelling of open rotor-wing-flap interactions with low-fidelity methods

by

E.A. Ebbens

to obtain the degree of Master of Science
at the Delft University of Technology,
to be defended publicly on Friday September 21, 2022 at 15:00.

Student number:	4492277	
Project duration:	September, 2020 – September, 2022	
Thesis committee:	Prof. dr. ir. L.L.M. Veldhuis,	TU Delft, supervisor
	Dr. ir. T. Sinnige,	TU Delft, chairman
	Dr. ir. D.A.M. De Tavernier,	TU Delft

Preface

This thesis marks the end of my Masters program in Aerospace Engineering at Delft University of Technology. My studies here made me find my passion for aerospace and engineering, for which I will always be grateful. Completing the Masters program throughout the coronavirus pandemic has been the most challenging task I have ever faced in my academic career, making this my greatest accomplishment. While the program has been challenging, it has also been entirely fulfilling, and I am grateful that I could study the field that interests me the most daily.

I would like to thank my daily supervisor, Prof. Leo Veldhuis, for all the discussions and feedback on my work and for his patience during my thesis project. Furthermore, I would like to thank Ramon Duivenvoorden for the invaluable discussions, feedback, and support along the way.

Lastly, I would like to thank my parents, Bob and Punk, for always being there for me and supporting me along the way in the past years. I would like to thank my close friends for all the distractions that made this period so much more enjoyable and for their understanding of the times I had to cancel any plans because of an exam, assignment, or thesis. Lastly, I would like to thank my girlfriend, Masja, who always encouraged me to achieve my goals and was always there for me in both the worst and the best of times.

E.A. Ebbens
Delft, September 2022

Summary

The rapid increase in air traffic and stringent environmental targets necessitates radical new aircraft configurations that are quieter, environmentally friendly, and capable of landing on regional airports to relieve the major European hubs. One solution that is investigated by the scientific community and industry is (hybrid-)electric aircraft with distributed open rotors (propellers) along the leading edge. The open rotors exploit synergistic interactions with the wing to augment the lifting capability aside from its function of providing thrust to the aircraft. The lift augmentation allows for increased short take-off and landing (STOL) capabilities and a reduced wing size for further cruise drag reduction.

The closely-coupled nature of the rotors and wings necessitates novel physics-based analysis methods for researching and designing these aircraft configurations. The present thesis developed a fast numerical method to analyze wings with closely-coupled leading edge rotors and deflected flaps. The main research question is, therefore, answering how fast aerodynamic analysis methods can be applied to predict the aerodynamic performance of an open rotor-wing-flap configuration?

The developed numerical analysis tool ORWFIS (Open Rotor-Wing-Flap Interactions Solver) is a quasi-3D viscous analysis tool consisting of an integrated framework of a separate rotor, slipstream, inviscid three-dimensional wing, and viscous two-dimensional wing analysis methods. The tool is written for the analysis of arbitrary rotor and wing geometries.

A Blade Element method adapted for a non-uniform inflow is utilized for the rotor analysis. The method calculates the rotor thrust, torque, and normal force. The slipstream is modeled by a cylindrical slipstream tube model derived from the rotor blade circulation distribution. The slipstream tube models axial and azimuthal variations of vorticity, contraction, and deflection. A custom non-planar Vortex Lattice Method (VLM) is developed, which models the main wing and the flap as separate coupled lifting surfaces to analyze the aerodynamic forces of the wing. The two-dimensional viscous multi-element analysis method MSES is coupled to the VLM using a novel decambering method to correct for viscous, compressibility, and thickness effects.

The rotor inflow and the slipstream deflection are calculated from the wing-induced velocities. Likewise, the wing's circulation depends on the slipstream position and its vorticity strength. Therefore, the rotor, slipstream, and wing analysis modules are solved iteratively to resolve the interactions. Convergence on the rotor and wing interactions was obtained for the case of a moderate thrust and angle of attack. Furthermore, convergence was reached on the mesh. The computational time for analysis at one angle of attack was found to be around 10 minutes.

The validation of the analysis tool has been performed for a wing in an unpowered (rotor-less) high-lift configuration with deflected single-slotted flaps, a powered cruise configuration with a leading edge rotor with retracted flaps, and finally, a wing in a powered high-lift configuration with a leading edge rotor and deflected single-slotted flaps.

The validation of the unpowered high-lift configuration has shown a good agreement between the analysis tool and the lift coefficient of a wall-to-wall wing at low angles of attack between 0 and 7 degrees. At lower and higher angles of attack, the lift coefficient was overestimated compared to the measured values. This is attributed to the lack of MSES data in these regions of the angle of attack due to the inability of the method to converge. The non-linear part, including the stall point, could not be predicted. For a different dataset at an angle of attack of six degrees, excellent agreement was found between the ORWFIS predicted chordwise lift distribution and pressure measurement derived distribution of the experiment.

In the validation of the powered cruise configuration, it was observed that the predicted lift polar matches well with the measurements from the experiment. The zero-lift angle of attack is slightly underestimated, which is attributed to nacelle effects. The lift augmentation due to the rotor and the wing is shown to agree well with the measurements. The drag is observed to be slightly underestimated for the unpowered case compared to the experiments, which are attributed to the nacelle and three-

dimensional effects. Furthermore, the drag is thought to be overestimated in prop-on conditions as slipstream interaction effects on the viscous boundary layer are not modeled in the present method.

The analysis method was for an ORWF configuration with a 30-degree flap deflection and with sectional lift measurements at two spanwise stations. Excellent agreement is found at the blade-up going side for the lift coefficients and the lift curve slope at low angles of attack. The lift was overestimated at higher angles of attack due to the inability of MSES to converge in this range. The lift at the blade-down going side is overestimated over the entire angle of attack range. This has been attributed to the slipstream distortion, which was unable to be modeled by the slipstream model. The slipstream distortion makes it difficult to compare sectional lift predictions and is expected to reduce the lift on the flap.

The analysis of the effect of modeling the full interaction between the rotor and a wing compared to merely the one-way coupling of the rotor on the wing revealed has been investigated. The results revealed that the effects of the wing on the rotor could not be neglected as it leads to a notable underestimation of rotor thrust and normal force, as well as the lift augmentation on the wing.

It is concluded that the rotor, wing, and flap can be effectively coupled using low-fidelity methods. The finite slipstream correction allows for the coupling of the slipstream with the wing but is shown to be sensitive to deviations in the flap positions. The effect of modeling the full interaction between the rotor and a wing compared to merely the one-way coupling of the rotor on the wing revealed that the effects of the wing on the rotor can not be neglected. The one-way coupling leads to a notable underestimation of rotor thrust and normal force, as well as the lift augmentation on the wing.

Furthermore, it is concluded that the dynamic pressure effect and swirl effect can be captured and yield acceptable predictions. However, the lack of slipstream distortion can reduce the accuracy of flapped wings. It was further concluded that thickness could not be neglected with multi-element airfoils but that the decamber method effectively corrects the VLM for thickness effects. Furthermore, MSES is concluded to be a significant limiter in the accuracy of the results at higher angles of attack. It has unreliable convergence for multi-element airfoils and cannot model the slipstream effects on the boundary layer.

Investigating the effect and modeling of slipstream distortion around flapped wings is recommended. Furthermore, developing a higher-fidelity finite slipstream correction is recommended as it greatly influences the quality of the results while being sensitive to geometry changes. Lastly, further research into non-uniform slipstreams on two-dimensional airfoils at high angles of attack is recommended, and methods to implement two-dimensional viscous solvers with integrated slipstream effects in three-dimensional VLMs.

Contents

List of Figures

List of Tables

Nomenclature

C_L	Lift coefficient [-]
C_l	Sectional lift coefficient [-]
C_{D_i}	Induced drag coefficient [-]
C_{D_p}	Profile drag coefficient [-]
C_{L_α}	Lift curve slope [1/rad]
$C_{L_{max}}$	Maximum lift coefficient [-]
dC_l	Local lift coefficient [-]
D	Drag [N]
D_r	Rotor diameter [m]
J_{mod}	Modified advance ratio [-]
L	Lift [N]
m, m_r	Amount of spanwise panels in VLM mesh outside and within slipstream immersed wing section, respectively.
n	Rotor rotational speed [RPM]
n_w, n_f	Amount of chordwise panels in VLM mesh on wing and flap, respectively.
Q	Local rotor torque [N]
r	Rotor radius [m]
T	Thrust [m/s]
u_e	Local external velocity [m/s]
V_0	Axial freestream velocity at the rotor blade element [m/s]
V_R	Local inflow velocity at rotor blade element without induced velocities [m/s]
V_∞	Freestream velocity [m/s]
V_a	Axial induced velocity at the rotor plane [m/s]
V_e	Local inflow velocity at rotor blade element with induced velocities [m/s]
V_p	Developed axial induced velocity [m/s]
u_{max}	Maximum external velocity on airfoil element [m/s]
w	Induced velocity [m/s]
X_f	Horizontal flap position [m]
X_p	Horizontal rotor position [m]
Y_f	Vertical flap position [m]
Y_p	Vertical rotor position [m]

α	Angle of attack [deg]
α_0	Zero-lift angle of attack [deg]
α_i and α_g	Geometric angle of attack [deg]
α_p and α_r	Rotor angle of attack [deg]
α_{stall}	Stall angle of attack [deg]
β	Geometric pitch at local blade element [deg]
δ_f	Flap deflection angle [deg]
ϵ_s	Slipstream deflection angle [deg]
ζ	z-coordinate non-dimensionalized with jet radius [-]
Γ	Circulation [m^2/s]
η	y-coordinate non-dimensionalized with jet radius [-]
θ	azimuth angle with respect to jet center [rad]
ξ	x-coordinate non-dimensionalized with jet radius [-]
ω	Rotor rotational speed [rad/s]
ϕ	Angle of local inflow velocity at rotor blade element without induced velocities with rotor rotation plane [deg]
ρ_∞	Freestream density [kg/m^3]
Subscript: ind	Wing-induced velocities
Subscript: ss	Slipstream
Subscript: v	Viscous

1

Introduction

The rapid increase in air traffic introduces a need for quieter aircraft and due to the increasingly pressing issue of global warming also a need for less polluting aircraft. Stringent environmental targets such as specified in the vision for aviation by the European Advisory Council for Aeronautics Research in Europe (ACARE) [1] are pushing for radical new aircraft configurations to improve fuel efficiency and limit the perceived noise.

The growth of air traffic also requires changes in the commercial air transportation system such as the integration of regional airports to relieve the already at maximum capacity major European Hubs [2]. For the integration of regional airports quiet regional aircraft with Short Take-Off and Landing (STOL) capabilities are required to operate on the smaller runways without sacrificing passenger capacity.

One radical new aircraft configuration that is considered to reduce greenhouse gas emissions and to allow for the integration of regional airports are distributed (hybrid-)electric propulsion aircraft with lift augmenting leading edge propellers. For example, the 70 PAX regional concept aircraft of the SynergIE project of Airbus and DLR [3] shown in Figure 1.1. These aircraft configurations contain multiple collections of closely coupled rotors, wings and flaps. The present thesis focuses on the analysis of such a collection of a tractor rotor with a trailing wing and deflected flap, from hereon referred to as an Open Rotor-Wing-Flap (ORWF) configuration, as shown in the schematic of Figure 1.2. The motivation behind the research on distributed (hybrid-)electric propulsion with an ORWF configuration is described in section 1.1. Thereafter, the outline of the thesis is presented in section 1.2.

Figure 1.1: The DEP-12 regional aircraft from the SynergIE project with 70 PAX capability featuring distributed hybrid propulsion (turboelectric) with twelve leading-edge open rotors. [3]

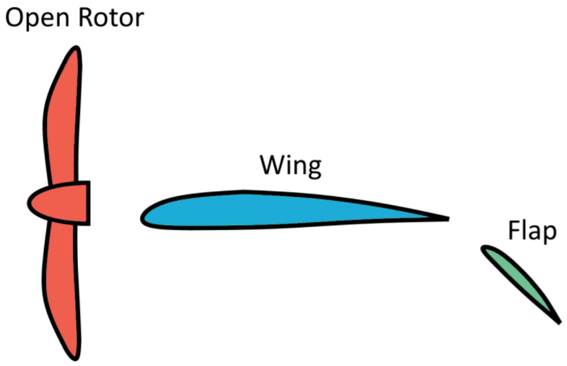

Figure 1.2: The three elements of the ORWF configuration: open rotor (red), wing (blue) and the flap (green). Modified from Sinnige [4].

1.1. Motivation

Distributed (hybrid-)electric propulsion

Electric or hybrid-electric propulsion for aircraft is one of these innovations with the potential to reduce emissions, reduce perceived noise and allow for STOL capability. Contrarily to reciprocating or turbine engines, electric motors have an extremely high efficiency, low weight, few moving parts and can be scaled with negligible effects on their efficiency and power-to-weight ratio [5]. The unique scale independence characteristic of electric motors allows therefore for the opportunity to distribute the propulsion around the airframe with multiple smaller electric motors without penalizing the total efficiency or weight of the propulsion system. The distribution of the propulsion opens up the opportunity for synergistic interactions between the open rotor flow fields and the airframe. The exploitation of this synergy improves the aircraft performance [5].

Electric and hybrid-electric aircraft are still at an infant stage of technology development and can not readily be implemented into larger and longer range aircraft until the technology has sufficiently progressed in its capabilities. Moore [5] states that Distributed Electric Propulsion (DEP) aircraft will first be adopted into the General Aviation (GA) market and then progressively into larger and longer range aircraft such as regional commuter aircraft. Although it is true that the energy density of batteries is considerably less compared to current aviation fuels, the higher efficiency of electric motors and the propulsion integration benefits still allow for a net increase in total efficiency and reduction in operating costs for short-haul full electric aircraft, where the mass penalty is less pronounced [5].

Lift augmentation through leading-edge rotors

There are multiple types of beneficial propulsion integration concepts explored in literature such as capturing tip-vortex energy [6][7], boundary-layer ingestion [8], high-lift augmentation [9] and other concepts [10].

The high-lift augmentation is a promising option that has been a point of interest for research institutions in the last couple of years. The open-rotors used for the propulsion are placed in close vicinity of the wing, locally accelerating the air. The slipstream of the open rotor alters the flow conditions surrounding the wing by increasing the dynamic pressure and, depending on the rotor location, increasing the circulation. The slipstream interactions allows the wing to achieve a higher maximum lift coefficient than the isolated wing. As a result, a reduction in wing area [9] and increase in STOL capabilities can be realized [11]. It is for this reason that the high-lift augmentation concept the focus is of this literature study and from hereon meant when referring to distributed (hybrid-)electric propulsion.

Moore [5] differentiates between three rotor installation concepts to increase the dynamic pressure and circulation of a wing with closely-coupled rotors as shown in Figure 1.3. The left concept features an over-the-wing rotor configuration near the trailing-edge to maximize the impact on the circulation. However, the configuration results in structural complications for the mounting of the rotor and transfer of loads to the wing, especially if placed near the trailing-edge. Furthermore, the mounting structure obstructs the rotor inflow, increasing the noise, and can cause difficult to predict aerodynamic penalties. The concept in the center of the figure shows a trailing-edge rotor configuration which is structurally less complex but has even worse inflow characteristics which increases the noise further. The right concept is the leading-edge rotor configuration which has the cleanest inflow, is structurally the simplest, and allows for more certainty in the analysis of the interaction on the wing performance. However, this concept is the least effective in inducing circulation. Despite this, Moore et al. have chosen the leading-edge rotor configuration for the use in the NASA LEAPTech (Leading Edge Asynchronous Propeller Technology) DEP demonstrator project not because it is the optimum but because it allows for the least uncertainty. The analysis of the leading-edge rotor configuration is, therefore, also the focus in the present work.

Analysis needs for ORWF configurations in DEP concepts

The emergence of distributed (hybrid-)electric propulsion aircraft with highly coupled aero-propulsive features raises the need for a multi-disciplinary design approach and rapid analysis tools to capture the aerodynamic interactions [5].

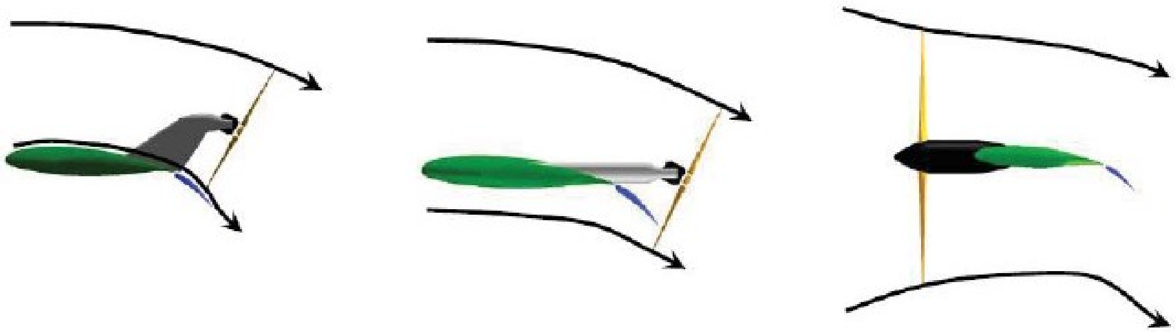

Figure 1.3: Three open rotor installation concepts on a wing. Arrows depict streamlines. Left: over-the-wing configuration. Center: Trailing-edge (or pusher) configuration. Right: Leading-edge (or tractor) configuration. [5]

Traditionally, the design of conventional propeller aircraft limited aero-propulsive coupling and designed the isolated airframe and propulsion system separately. After the design, the effect of the mutual interaction is measured during the performance analysis as a penalty for the assumed isolated systems [12]. The need for physics-based tools was therefore not required, justifying the use of simpler regression methods [5].

However, the high-lift augmentation integration benefit that is studied here requires sophisticated analysis tools that can analyse the open rotor-wing interactions at low speeds with moderate to large flap deflections. As the modelling of the interactions in the high-lift configuration are far from elementary and highly dependent on the local geometry, new physics-based aerodynamic analysis tools are required for the use in the optimization of the closely-coupled open rotor, wing and high-lift configuration. These analysis tools can provide valuable insights into the effects of the geometry on the aero-propulsive interactions. Furthermore, the analysis tools can aid as a stepping-stone for multidisciplinary design and optimization suites for (hybrid-)electric propulsion aircraft, therefore contributing to the clean sky revolution.

1.2. Thesis outline

The present thesis is divided into three parts. The first part covers the literature study on the governing aerodynamic effects in an ORWF configuration in chapter 2. Following the insights from the literature study, the research scope and questions are formulated in chapter 3.

The second part covers the methodology of the numerical analysis tool for ORWF configurations developed in the present research. chapter 4 provides a brief overview of the methodology and the different analysis modules. The methodology part further contains chapters each describing the different analysis modules. The integration and convergence of these modules into the complete analysis tool is, thereafter, described in chapter 10.

The final part covers the validation of the complete analysis tool in chapter 11 as well as the analysis of the coupling effects between the rotor and wing in chapter 12. Lastly, the final conclusions and recommendations are presented in chapter 13.

I

Literature study

2

Aerodynamic phenomena of open rotor-wing-flap configuration

For the design of a low- to medium-fidelity analysis tool for an OWRF configuration, the aerodynamic phenomena governing the flow field surrounding this configuration have to be understood first. Therefore, in this chapter the governing aerodynamic phenomena found in literature are presented and discussed.

First, the aerodynamic phenomena that are common on all ORWF elements are presented in section 2.1. Following, the phenomena for each isolated element and the interactions are presented. First, the isolated rotor and the rotor in proximity of a wing and flap are discussed in section 2.2 and section 2.3, respectively. After the rotor, the aerodynamic phenomena of an isolated wing and of the wing and flap under influence of the rotor slipstream are treated in section 2.4 and section 2.5, respectively. Finally, the interactions effects between a wing and a flap are presented in section 2.6.

2.1. General lifting surface phenomena

Physically, the forces on the lifting surfaces are generated by the pressure and shear stress applied on the geometry by the flow. However, for convenience the flow is commonly divided into inviscid and viscous flow. While inviscid flow does not exist in nature, the division allows for a more intuitive understanding of the flow phenomena. For high Reynolds number flows, such as for aircraft, the viscous phenomena govern especially in the boundary layer surrounding the geometry whilst the flow outside the boundary layer behaves more like an inviscid fluid [13] .

The lift is mainly an inviscid phenomena and a result of the circulation around the geometry, providing a lower pressure on the upper surface than on the lower surface. Both inviscid and viscous effects contribute to the drag of the body. Inviscid induced drag appears due to the induced downwash by the vorticity in the wake and is a result of the lifting surface being finite in span. Friction drag appears due to the shear stresses in the boundary layer. Form drag or pressure drag due to separation appears as a result of low pressure regions near the trailing edge due to boundary layer separation.

The boundary layer thickness grows as it develops along a surface. The external flow is displaced by this growing boundary layer with as a result that the effective shape of the lifting surface changes. The change in the effective shape is called the decambering effect and reduces the lift.

2.2. Isolated rotor phenomena

The rotor has as main function to provide thrust by rotating its blades to produce aerodynamic forces. In the ORWF configuration, the rotor is placed in front of the leading-edge of the wing in a so-called tractor configuration. The rotor is generally powered by a conventional turboshaft or an electric motor that is inside a nacelle next to the rotor. The isolated rotor effects can be divided into the effects at the rotor plane and the effects at the slipstream behind the rotor.

2.2.1. Rotor blade effects

The rotor imparts rotational momentum and linear momentum on the flow, the former resulting in torque to be overcome and the latter producing useful thrust. As a result, a total pressure, static pressure and tangential velocity jump occurs across the rotor plane.

Induced velocities are present on the rotor blades and are a natural result of the finite span of the rotor blades. Like a wing, the rotor blades can be represented by lifting lines. Consequently, change in the circulation along the span has to be accompanied by trailing free vortices to adhere to the Helmholtz theorem which states that a vortex filament can not end in the fluid [13]. A result is a helical vortex sheet that is shed from the rotor blades, which is further discussed in subsection 2.2.2. This vortex sheet induces velocities at the rotor plane.

For axial inflow conditions, that is to say that the rotor is not at a sideslip angle or angle of attack, the blade loading is independent of the azimuth angle. However, for non-axial inflow conditions the effective angle of attack of the rotor blade changes with the azimuthal angle. For a rotor at a positive angle of attack for instance, the down-going blade experiences an increase in local angle of attack while the up-going blade experiences a decrease in local angle of attack as is shown in Figure 2.1. As a result, the thrust and torque increase at the down-going blade and decrease at the up-going blade. This causes an imbalance in the forces and moments normal to the rotor axis such that a normal force, and pitch and yaw moments are produced. The normal force contributes directly to the lift of the aircraft. The forces and moment normal to the rotation axis have been experimentally observed in wind tunnel tests in various studies [14, 15].

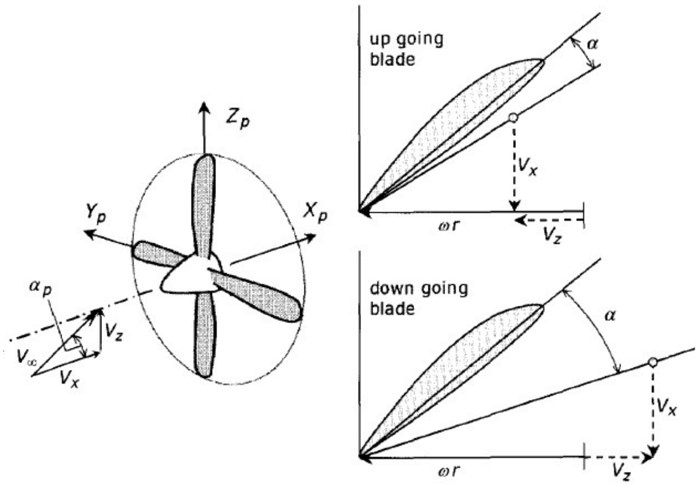

Figure 2.1: The effect on the blade loading of a rotor at different azimuth locations when placed at an incidence with the incoming flow. The up-going blade sees a lower angle of attack, resulting in a lower thrust and torque force, while the down-going blade sees a higher angle of attack, resulting in a higher thrust and torque force. The net result is an addition of forces and moments normal to the rotation axis. [16]

The rotor blades rotate periodically with as result that the loading changes in azimuthal direction with time, making the forces and moments inherently unsteady.

2.2.2. Isolated slipstream effects

The rotational and linear momentum that is imparted on the flow by the rotor causes a complex three-dimensional wake to develop behind the rotor, the so-called slipstream. The slipstream is formed by the helical vortex sheet that is shed from the rotor blades due to the spanwise circulation distribution. Most of the vorticity is concentrated at the tip as a result of the sharp gradient in the blade circulation at this location and because the vortex sheet rolls up into a concentrated tip vortex. A sketch of the helical vortex sheet is shown in Figure 2.2.

Velocity development

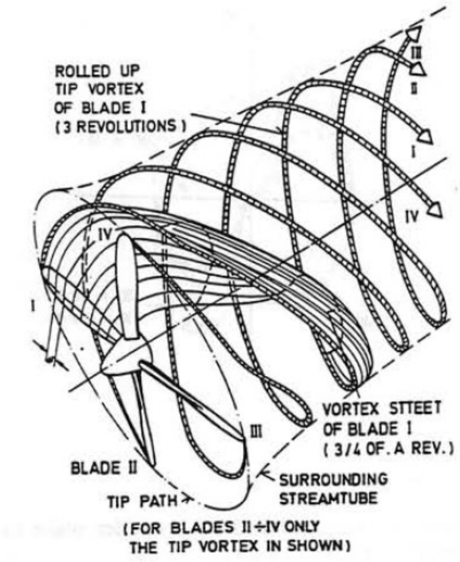

Figure 2.2: A schematic of the helical vortex sheet that is shed from a rotor. A rolled up tip vortex appears at each of the blade tips. Furthermore, the surrounding streamtube contracts. [17]

The helical vortex sheet increases the axial velocity in the slipstream as it develops along the streamwise direction. This axial velocity development is continuous and occurs ahead of the rotor and behind the rotor. In line with the classical momentum theory, the induced axial velocity at the far-field is twice the induced axial velocity at the rotor and zero infinitely far ahead of the rotor [18].

The tangential velocity in the slipstream is zero ahead of the rotor and jumps to a fixed value across the rotor plane. This tangential velocity jump causes a swirl in the slipstream. The swirl angle, ratio of tangential velocity and axial velocity, changes in streamwise direction as the induced axial velocity changes while the tangential velocity remains constant. The axial and tangential velocity development are shown in Figure 2.3.

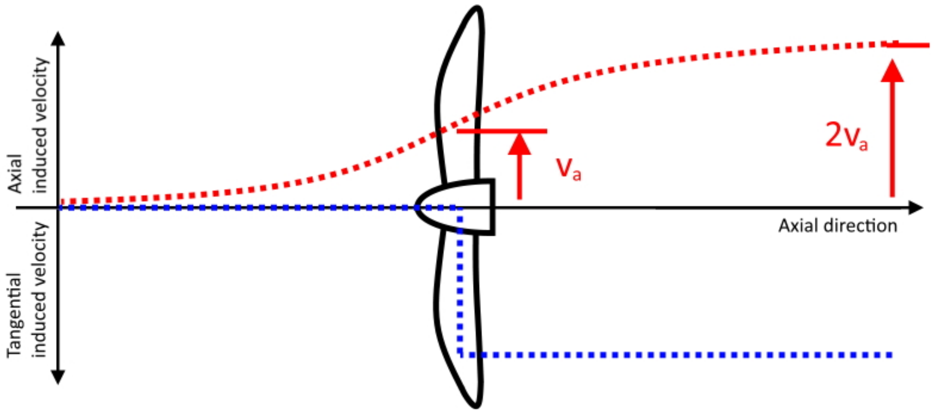

Figure 2.3: Axial and tangential induced velocity development along the rotor axis. The axial induction velocity gradually increase and at infinity reaches a value twice of the value at the rotor plane. The tangential velocity jumps to a constant value at the rotor plane. [16]

The induced axial and tangential velocities vary along the radius as related to the the spanwise circulation distribution along the rotor blades. The time-averaged slipstream velocities is, therefore, varying along the radius. The velocity profile of the slipstream shows therefore the largest axial and induced velocities in the middle segment of the blade. The axial induced velocities drop to zero near the tip and hub while the induced tangential velocities drop to zero at the tip and to a low value at the hub. The result is a donut shaped dynamic pressure increase for a time-averaged slipstream with the lowest dynamic pressure increase near the hub and tip and largest in between the hub and tip. An example of such axial and tangential induced velocity profile in the slipstream is shown in Figure 2.4.

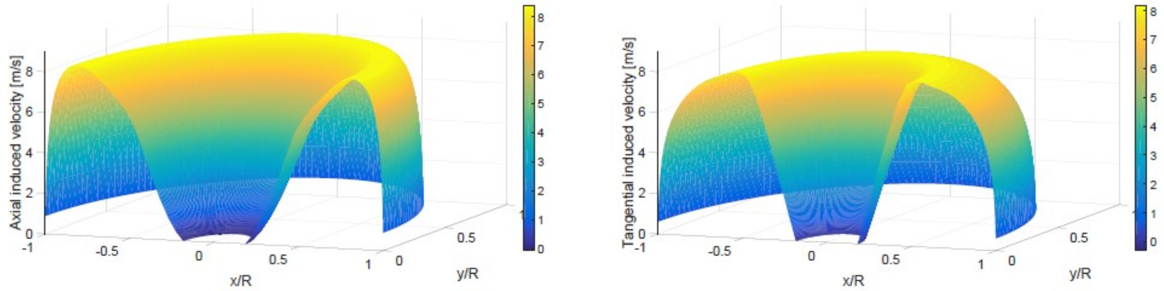

Figure 2.4: Distribution of the time-averaged axial (left) and tangential (right) induced velocities at the rotor plane forms a donut shape. [19]

Contraction and deflection

As the axial velocity gradually increases in the slipstream, the slipstream itself contracts. The slipstream area has to decrease for an increase in the velocity through the area to keep the mass flux constant according to the conservation of mass. The contraction for lightly loaded rotors is only a few percent [20]. However, highly loaded rotors can theoretically experience contraction of up to 30% or more [21]. The contraction also induces a radial velocity component in the slipstream, which is largest near the rotor disk and decreases to zero as the slipstream contracts to its far-field area [21].

Unlike for the axial inflow case, the slipstream deflects when the rotor is at an angle with the freestream velocity. The freestream velocity will tend to deflect the slipstream to align with the freestream while the normal force of the rotor will tend to deflect the rotor to align with the rotor axis. The resulting slipstream deflects at an angle that is dependent on the thrust coefficient and is in between the rotor axis and freestream velocity [22]. The contraction and deflection effect of the slipstream for a rotor at incidence is shown in Figure 2.5.

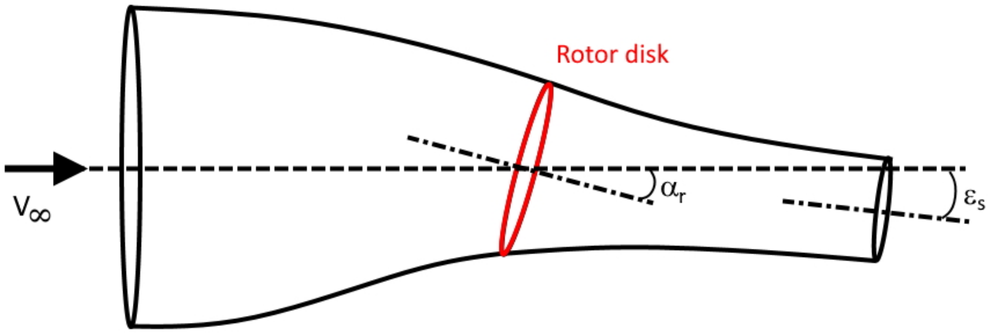

Figure 2.5: Streamtube of the flow through the rotor disk contracts ahead and behind the rotor. The streamtube deflects by a certain angle due to the incidence angle of the rotor with the freestream velocity.

2.3. Wing and flap interaction phenomena on rotor and slipstream

Placing a rotor in a rotor-wing-flap configuration introduces a set of interaction effects that change the flow field surrounding the rotor. These interactions change the rotor performance and the slipstream characteristics compared to the isolated rotor conditions. Three main interaction phenomena are identified from literature: the wing upwash effect, the slipstream turning effect, the slipstream distortion effect and the swirl reduction effect.

2.3.1. Wing upwash effect

The circulation of the wing and flap introduces an upwash component at the rotor plane. The upwash at the rotor plane can be seen analogous to an isolated rotor at an increased incidence with the incoming flow according to Veldhuis [16].

Heidelberg and Woodward [23] investigated the change in the propeller inflow conditions due to the presence of a wing. It was observed that the wing caused a nearly uniform inflow angle across the propeller disk. Furthermore, it was observed that the propeller inflow angle increased at a rate of 150% of the wing angle of attack. The upwash of the wing can therefore severely change the inflow conditions at the rotor plane. The wing upwash effect on the rotor is visualized in Figure 2.6.

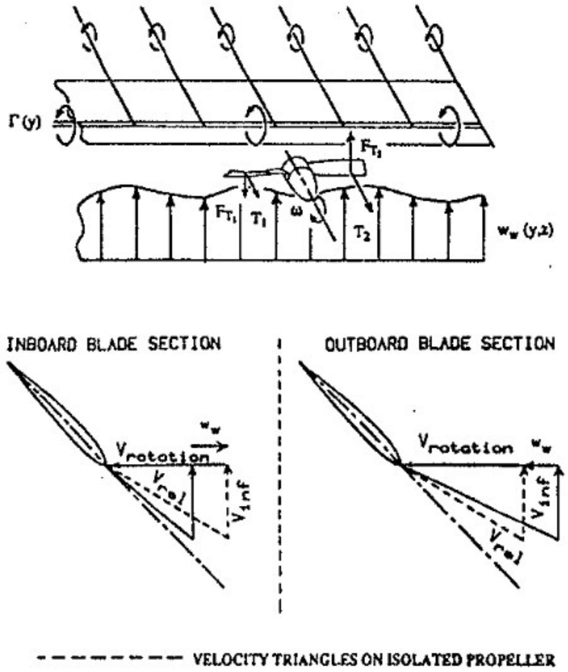

Figure 2.6: Sketch of the wing upwash effect on the rotor. The circulation at the wing (top) induces an upwash at the rotor plane (center). The result is an increased angle of attack for the down-going blade, increasing the loading, and a decreased angle of attack for the up-going blade, decreasing the loading, causing forces and moments normal to the rotation axis. [24]

The non-axial inflow conditions at the rotor plane causes the blade loading to be varying with the azimuth angle. As a result, the rotor produces an additional normal force and moments. The non-uniform inflow also results in the induced velocities to vary with the azimuth angle. Larger induced velocities at the down-going blade side and smaller induced velocities at the up-going blade side are formed, such that the slipstream velocity profile is not axi-symmetric anymore.

The generated rotor moments are small compared to the moments for the total aircraft [25], however the rotor normal force can considerably contribute to the lift coefficient of the rotor as observed in the PROWIM wind tunnel campaign of Veldhuis [16]. Witkowski, Lee, and Sullivan [24] have researched the effect of the wing upwash on the rotor normal force, or hub force as called in the literature. In the experimental set-up the rotor incidence was kept constant at zero with the freestream velocity. The wing angle of attack was varied and the change in rotor normal force was measured. A linear relationship is observed for the increase in normal force with an increase in wing angle of attack up until $8\,\mathrm{deg}$. The results are compared to the analysis methods of Ribner [22] and McCormick [26] and it is shown that these methods severely underpredict the rotor normal force with wing angle of attack. Witkowski et al. attribute this to the assumed constant upwash at the rotor disk, which is not the case in reality. They also attribute the discrepancy to the use of an isolated wing for the upwash at the rotor instead of the using a wing with the slipstream altered circulation distribution. A linear relationship between the rotor side force and the wing angle of attack is also observed.

The upwash at the rotor is amplified for large flap deflections. The deflection of trailing-edge flaps can considerably increase the circulation of the wing [8], resulting in an increase in upwash at the rotor plane. Contrarily, Kuhn and Draper [11] has not consistently observed an increase in rotor normal force due to an increase in flap deflections. However, it is stated that this could be due to the relatively large distance between the rotor and the wing which is about 45% of the diameter to the leading-edge and 62% of the diameter to the wing quarter-chord.

The numerical analysis of Cole, Maughmer, and Bramesfeld [27] has shown that the negligence of the upwash of the wing on the rotor resulted in a 12.5% discrepancy in wing span efficiency compared to the analysis including the upwash of the wing at the rotor plane. The wing upwash effect can therefore have a considerable influence on the aerodynamic performance of the wing. The numerical analysis of Veldhuis [16] has also shown observable differences in the lift distribution of the wing between the approach in which the upwash at the rotor is neglected and the the approach in which the upwash is included.

Observable differences between the thrust coefficient, power coefficient and efficiency of an isolated propeller and propeller within the wing flow field are shown in the numerical analysis of Marretta [28]. The thrust coefficient, power coefficient and efficiency are higher under the influence of the upwash of the wing.

2.3.2. Slipstream turning effect

A wing that is immersed in a slipstream turns the slipstream downwards due to its circulation as is schematically shown in Figure 2.7. The slipstream therefore deviates from the path that an isolated rotor slipstream would follow. The turning of the slipstream generates an additional lifting force as the momentum in the slipstream is directed downwards. This turning is amplified with trailing-edge flap deflections. The turning of the slipstream is limited by the boundary layer separation over the flap due to the adverse pressure gradient that is present.

In the experiments of Kuhn and Draper [11] the turning effect for a tested wing geometry with two-part plain flaps is investigiated. It was observed the turning angle could only reach at most 45 degrees under static thrust conditions for the investigated geometry. This turning angle was obtained with a 60% chord flap deflected at 30 degrees and the 30% chord flap deflected at 50 degrees. Higher flap deflections reduced the turning angle and the turning effectiveness, the ratio between the resultant force due to the turning and the thrust force. The turning angle was increased to 67 degrees by the use of two auxiliary vanes.

This research was followed up by Kuhn and Draper [29] for a wing with a double slotted trailing-edge flap instead of a plain flap. For this wing geometry, a turning angle of 63 degrees is achieved with a 10% loss of thrust. This turning angle was obtained with the 60% chord flap deflected 60 degrees and the 30% chord flap deflected 40 degrees. The presence of a slot therefore considerably increases the maximum turning angle that can be achieved. The turning angle increased to 74 degrees with the inclusion of an auxiliary vane above the flap. The turning angle increased from 63 degrees to 73 degrees for a wing without auxiliary vanes when the wing was placed at a 10 degree incidence (nose-up) relative to the rotor axis.

Boundary layer control by means of blowing a jet of air over the flaps to increase the turning angle is investigated by Spreemann and Kuhn [30]. It is observed that the effect of the blowing is primarily to reattach the slipstream. The blowing at small flap deflections where no separation would occur therefore does not contribute to the effectiveness of the turning other than the direct contribution of the jet thrust. At flap deflections beyond the deflections at which stall occurs for unblown flaps, great increases in turning angle are observed. However, the turning effectiveness considerably reduces at these higher flap deflections with blown flaps. A more recent investigation in internally blowing of flaps immersed in a slipstream is performed by Lenfers, Beck, and Radespiel [31] on a wing with plain flap deflected 60 degrees. The flow is successfully kept attached in the wing section immersed in the slipstream that would otherwise have separated.

In the experiments of Huston and Winston [32], a 20% spanwise variation in turning angle and 40% spanwise variation in turning effectiveness is observed for a wing with a double-slotted flap. This is attributed to the spanwise variation in angle of attack due to the swirl induced by the slipstream. The spanwise variations change under the influence of the ground effect.

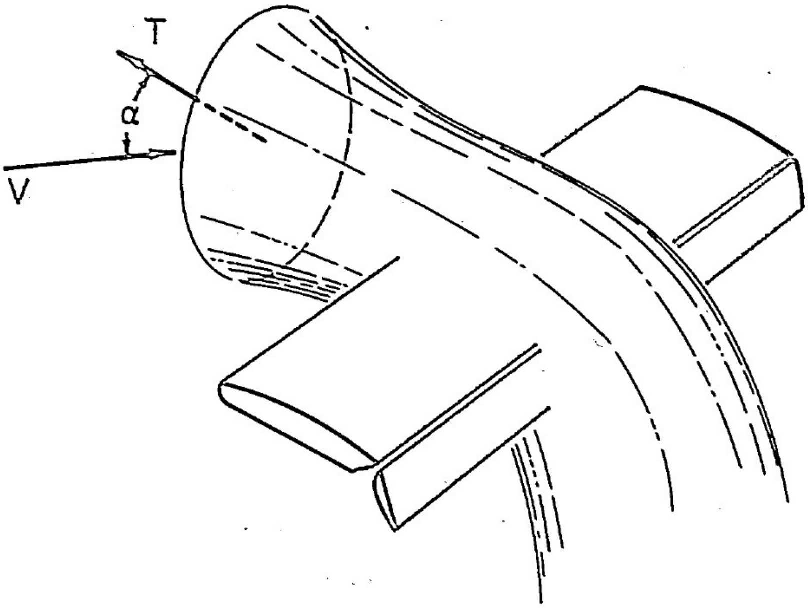

Figure 2.7: Slipstream turning effect in which the sliptream turns with a certain angle due to the deflection of the trailing-edge flaps. [33]

2.3.3. Slipstream distortion effect

The slipstream starts to shear in spanwise direction as it progresses along the wing chord, distorting the circular shape of the slipstream. This effect is observed in numerous wind tunnel experiments [34, 35, 24, 36, 16, 31]. This is due to the strong vorticity shed at the junction of the wing and the slipstream boundary as stated by Veldhuis [16] and Johnson, Witkowski, and Sullivan [35]. These vortices are shed here as a result of the steep lift gradient due to the slipstream swirl and dynamic pressure increase. Thus, for the inboard up rotating rotor, the slipstream on the lower surface shears inboard while the slipstream on the upper surface shears outboard. In Johnson, Witkowski, and Sullivan [35] it is observed through smoke visualisation that the tip vortex move in opposite direction on the upper and lower surface and then reconnect at the trailing-edge. This is schematically shown in Figure 2.8. Aside from the shearing slipstream, the slipstream shape remains well preserved for a wing with no flaps deflected and at near zero angle of attack [16, 34, 35].

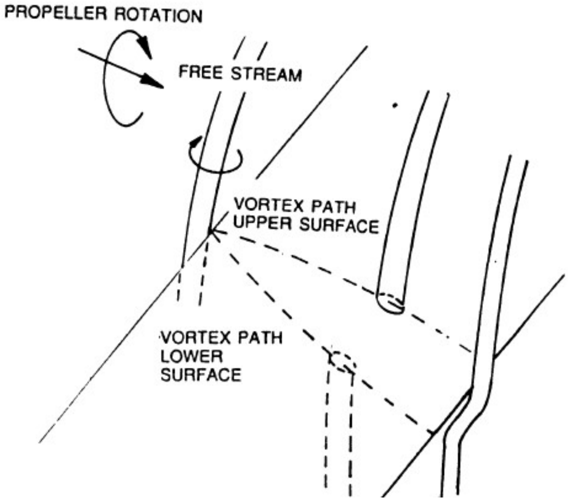

Figure 2.8: Slipstream distortion effect causing the tip vortex to move inboard on the upper surface and outboard on the lower surface when the propeller rotates outboard up. The tip vortex reconnects past the trailing-edge in a deformed shape. [35]

For wings with a deflected slotted flap the slipstream wake aft of the wing drastically changes as observed by the flow survey of Aljabri and Hughes [34]. It is shown that the swirl is removed and the slipstream does not have a distinct circular boundary anymore as the velocity perturbations are found below and laterally to the circular projection of the propeller disk. The wake survey results showing the cross flow field behind a wing without and with flap of [34] are shown in Figure 2.9. It can be observed that for the case of the wing with flap, no distinct swirl and slipstream boundary can be found unlike what is observed for the case without flap. Aside from this research, not much other research is performed on the slipstream distortion of slipstreams going over a wing with a deflected flap.

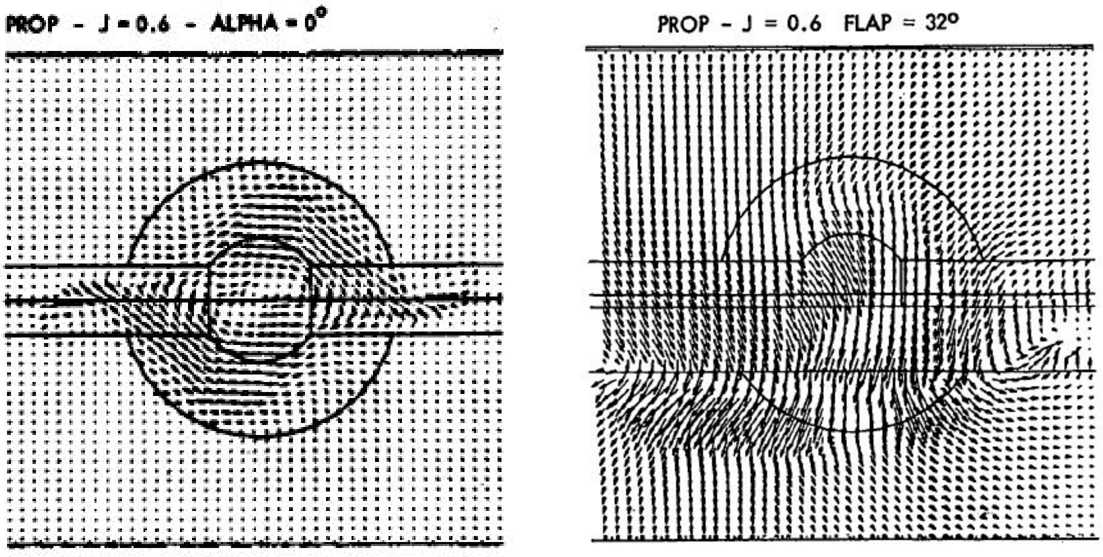

Figure 2.9: Wake survey observations for a wing immersed in a slipstream without (left) and with (right) flaps. [34]

2.3.4. Swirl Reduction effect

The presence of a wing in the slipstream acts as a flow straightener and recovers the swirl. As a result, the rotational velocity in the slipstream reduces. Veldhuis [16] attributes the reduction in rotational velocity mainly to inviscid phenomena of the wing induced upwash and downwash. At the up-going blade side the the downwash is augmented due to the increase in lift, counteracting the rotational velocity at this side. In contrast, at the down-going blade side a wing upwash is generated counteracting the tangential velocity at this side as well. The result is a reduction in the slipstream helix angle. Veldhuis states that the reduction in helix angle a function is of the rotor position with respect to the wing and the local angle of attack. Furthermore, it is stated that a part of the reduction in swirl can be attributed to viscous effects even though most of the reduction is due to the reduction in slipstream helix angle.

It is also shown by Veldhuis that the negligence of the swirl reduction or swirl recovery in the numerical analysis can cause considerable over-predictions in the loading.

2.4. Isolated wing phenomena

The wing provides the majority of the lift by inducing circulation on the flow and also contributes considerably to the overall aircraft drag. The lift linearly changes with angle of attack until considerable decambering due to boundary layer thickening starts to occur and due to separation of the boundary layer. The transition location from a laminar to turbulent boundary layer has a large effect on the separation at these higher angles of attack.

A laminar separation bubble often occurs on the upper surface of an airfoil at low Reynolds number conditions, such as at take-off and landing conditions. Due to an adverse pressure gradient the laminar flow separates, as the flow separates the boundary layer transitions from laminar to turbulent with reattachment as a result. A pocket of recirculating air, the laminar separation bubble, forms between the separation and reattachment point. The separation bubble locally reduces the pressure, creating additional lift and a pressure drag component as the bubble is usually present on the aft facing upper surface.

2.5. Slipstream interaction phenomena on wing and flap

When a part of the wing is immersed in the rotor slipstream, considerable phenomena in the interactions between the two can occur. The slipstream causes inviscid effects such as a dynamic pressure increase and a change in the local angle of attack distribution along the slipstream immersed wing section. The contraction and swirl of the slipstream induces a radial component influencing the wing inflow conditions. The slipstream also alters the boundary layer development along the wing and flap such that non-linear aerodynamic phenomena are influenced.

2.5.1. Dynamic pressure increase and swirl effect

As early as 1918, Ludwig Prandt observed two interaction effect of the slipstream on the wing: an effect due to the change in flow speeds and an effect due the change in the direction of the flow [37]. The former is referenced as the dynamic pressure effect and the latter is referenced as the swirl effect. The dynamic pressure effect occurs due to the increased axial velocity within the slipstream while the swirl effect occurs due to the tangential velocities in the slipstream.

The higher axial velocities in the slipstream create a higher dynamic pressure region surrounding the slipstream immersed wing section. The higher dynamic pressure augments the aerodynamic forces generated on the surface, locally increasing the lift and drag. The effect of only this dynamic pressure effect on the spanwise lift distribution is shown in Figure 2.10.

The tangential velocities in the slipstream interact with the wing by causing an upwash effect for the up-going blade side and a downwash effect for the down-going blade side. This upwash and downwash changes the local angle of attack at the wing section immersed in the slipstream. The upwash increases the angle of attack and therefore the lift increases in this region while the downwash decreases the angle of attack and therefore the lift decreases in the region at the other side of the rotor axis. The result is an s-shaped variation in the spanwise lift distribution as shown in Figure 2.11. The induced gradient in the spanwise loading also results in the shedding of strong vortices at the intersection between the slipstream boundary and the wing.

Combining the dynamic pressure and swirl effect results in an increase in lift at the up-going blade side due to the upwash and the increase in dynamic pressure and a small decrease in lift at the down-going blade side due to the downwash and increase in dynamic pressure effectively attenuating each other. The spanwise lift distribution of the combined case is shown in Figure 2.12. Both dynamic pressure and swirl effects have been observed in the experimental research of Aljabri and Hughes [34] and Fratello, Favier, and Maresca [38] using pressure measurements. The lift distribution outside of the slipstream is also altered by the slipstream due to the distorted vorticity sheet [16].

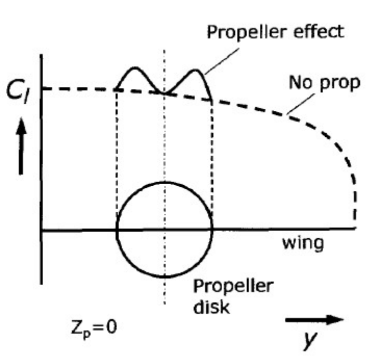

Figure 2.10: spanwise lift coefficient distribution for a wing under the influence of only the dynamic pressure increase effect of a slipstream. [16]

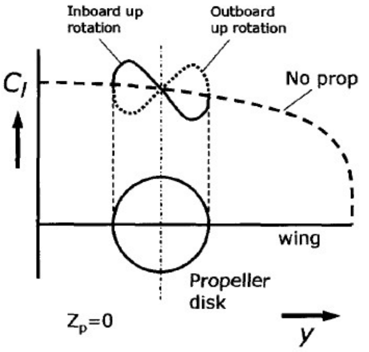

Figure 2.11: spanwise lift coefficient distribution for a wing under the influence of only the swirl effect of a slipstream for both an inboard up rotation and outboard up rotation.[16]

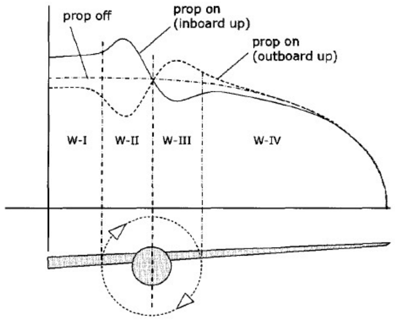

Figure 2.12: spanwise lift coefficient distribution for a wing under the influence of the combination of the dynamic pressure increase effect and the swirl effect. The influence of the slipstream on the lift distribution extends outside of the slipstream diameter. [16]

2.5.2. Swirl recovery effect

The wing acts as a flow straightener for the slipstream, therefore the wing affects the slipstream by reducing the swirl. However, the opposite effect of this interaction of the slipstream on the wing is called the swirl recovery effect.

The rotation of the slipstream is a loss for the rotor as the induction of tangential velocities does not generate a thrust force but a torque. This swirl loss is recovered by the wing, causing a net thrust (negative drag) contribution on the wing as observed by many authors such as Aljabri and Hughes [34], Kuhn and Draper [11], Aminaei, Mostofizadeh, and Dehghan Manshadi [39], and Johnson, Witkowski, and Sullivan [35] and Veldhuis [16].

The workings of this effect for a wing at zero-lift angle of attack can be described as follows. The upwash on the wing at the up-going blade side causes the lift vector to increase in magnitude and tilt forward which decreases the induced drag. At the same time, at the down-going blade side the downwash causes a downward lift vector tilted forward as well. The result is a net thrust (negative drag) contribution on the wing. Of course, for a wing at an angle of attack with positive lift, the lift vector does not point downwards at the down-going blade side. Instead, at the down-going blade side the downwash tilts the vector rearwards increasing the induced drag here. However, as the lift vector decreases in magnitude at this side while it increases at the up-going blade side, the net effect is still a thrust (negative drag) contribution.

2.5.3. Radial slipstream flow effect

The contraction of the slipstream causes an inwards radial flow. For off-centre rotor vertical position this can induce a downwash for a low vertical position or an upwash for a high vertical position as was observed in the wind tunnel experiments of Veldhuis [16] and Fei, German, and Patterson [40]. This effect is schematically shown in Figure 2.13. The result is an increased lift coefficient if the rotor is placed above the wing chord line compared to below the wing chord line. However, an optimum exists for the maximum lift coefficient, as an excessive high vertical rotor position reduces the frontal area of the wing that is immersed in the slipstream. Fei, German, and Patterson [40] has presented a linear relation between the optimum vertical rotor position for maximum lift and the unpowered lift coefficient.

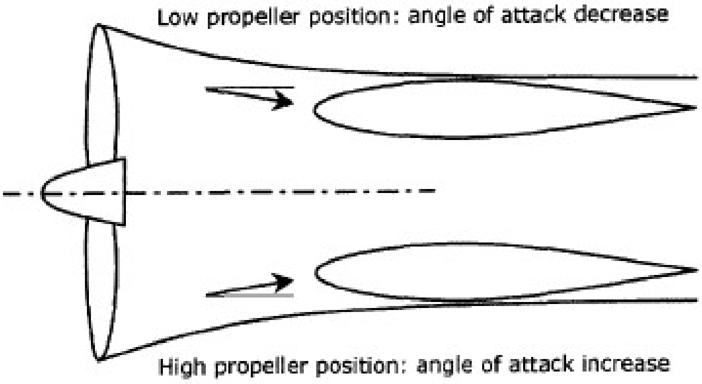

Figure 2.13: Drawing of the radial flow effect. The slipstream contraction induces a radial velocity component, resulting in a downwash for a low propeller position and an upwash for a high propeller position. [16]

2.5.4. Slipstream induced boundary layer alterations

The slipstream alters the boundary layer of the wing and flap. Miley, Howard, and Holmes [41] has observed that the boundary layer transitions from a laminar boundary layer to a transitional turbulent boundary layer to a reverse-transitional boundary layer and back again to a laminar boundary layer at the blade passage frequency. It is also observed that near the surface the turbulence in the boundary layer persists until some time after the passage of the propeller wake. This effect on a laminar boundary layer is visualized in Figure 2.14. Furthermore, laminar separation bubbles within the slipstream immersed wing section disappear entirely under the influence of the slipstream as observed by Veldhuis [16], Elsaadawy and Britcher [42], and Catalano [43] and Aminaei, Mostofizadeh, and Dehghan Manshadi [39]. Also the steady-state transition locations move towards the leading-edge as is observed by the experiments of Elsaadawy and Britcher [42] and Catalano [43] and Aminaei, Mostofizadeh, and Dehghan Manshadi [39]. Catalano [43] noted that the slipstream effects on the boundary layer extend further than the propeller diameter as viscous mixing occurs between the slipstream and the flow external.

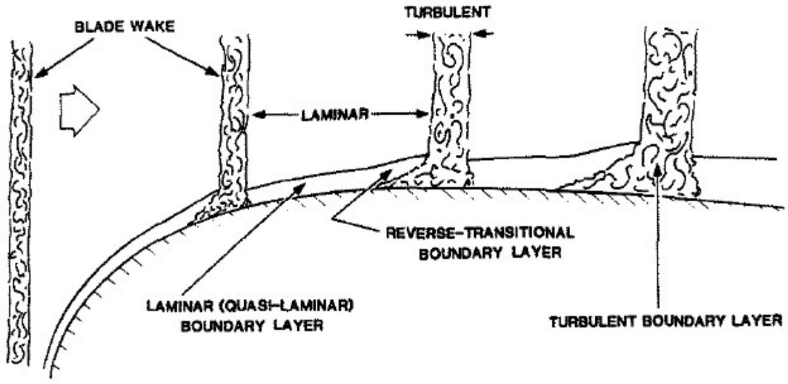

Figure 2.14: The boundary layer on a wing in a periodic rotor wake. The rotor wake that traverses along the chord causes the laminar boundary layer to transition to a turbulent boundary layer to a reverse-transitional boundary layer and back to a (quasi-)laminar boundary layer at the blade passage frequency. [41]

The slipstream causes steeper adverse pressure gradients on the wing and flap. This is observed in the wind tunnel experiments and numerical analysis of Lenfers, Beck, and Radespiel [31] for a wing with a plain flap deflected 60 degrees. As a result, the flow is observed to separate in the spanwise section of the wing that is immersed in the slipstream, while outside the slipstream no separation is observed. The position and extension of the flow separation is stated to be a function of the wing angle of attack and the rotor rotational speed.

In contrast, the experiment of Brenckmann [44] for an airfoil without flap delayed boundary layer separation is observed inside as well as outside of the slipstream compared to a wing in power-off condition. The experiments of Kuhn and Draper [11] and Kuhn and Draper [25] seem to support this as an increase in rotor power is observed to increase the stall angle of attack and suppress the decrease in lift in the post-stall regime. This effect was observed in wings in clean configuration as well as wings with trailing-edge flaps deflected.

These contradicting results are probably due to the difference in the geometry and flow conditions wherein the wing is analysed. In the case of Lenfers, Beck, and Radespiel [31], the experiment is ran on a high Reynolds number which probably caused a turbulent boundary layer to form way ahead of the plain flap for the wing without propeller slipstream effects. The steeper adverse pressure gradient due to the slipstream therefore dominated the change in separation instead of the effect of the slipstream on the boundary layer state. While for Brenckmann [44] and Kuhn and Draper [11, 25], the wing could have been mostly laminar in the unpowered condition, resulting in the slipstream effects on the boundary layer state to make the wing more resilient to stall.

2.6. Wing and flap interaction phenomena

Five favourable interaction phenomena between multi-element airfoils, and therefore between a wing and a trailing-edge flap, are identified by Smith [45]. A sketch of four of the five favourable interaction phenomena are shown in Figure 2.15.

The **slat effect** describes the effect of the interference on the flap due to the circulation of the wing. At angle of attack the wing has a circulation which induces velocities at the nose of the flap opposing the velocities caused by the circulation of the flap itself. As a result, the velocities at the nose of the flap are reduced therefore reducing the suction peak of the flap. The reduction in the adverse pressure gradient near the nose delays boundary layer separation on the flap.

The **circulation effect** describes the effect of the interference on the wing due to the circulation of the flap. The flap induces a vertical cross-flow up at the trailing edge of the wing. To adhere to the Kutta condition, the circulation on the wing has to increase such that the rear stagnation point remains at the trailing edge.

The **dumping effect** describes the effect of the increased trailing edge velocity on the wing due to the circulation interference of the flap. Closely coupled to the circulation effect, the circulation of the flap does not only increase the cross flow at the trailing edge of the wing but also the tangential flow speed on the upper surface at the trailing edge of the wing. The increased tangential flow speed allows the wing to discharge into a higher velocity region. As a result, the required velocity reduction, or pressure recovery, at the trailing edge is decreased. The adverse pressure gradient on the wing is therefore reduced as well.

The boundary layer of the wing leaves the trailing edge at a higher velocity than the free stream velocity. This wake recovers the freestream velocity off-the-surface. The **off-the-surface pressure recovery** is more resilient to adverse pressure gradients than recovery in contact with a surface.

The **fresh boundary layer effect** describes the effect of a new boundary layer forming on each consecutive element. The fresh boundary layer is thinner than a boundary layer covering the entire wing + flap length, allowing it to be more resilient to adverse pressure gradients and separation. Larger pressure gradients are then possible without separation, allowing for a higher lift coefficient.

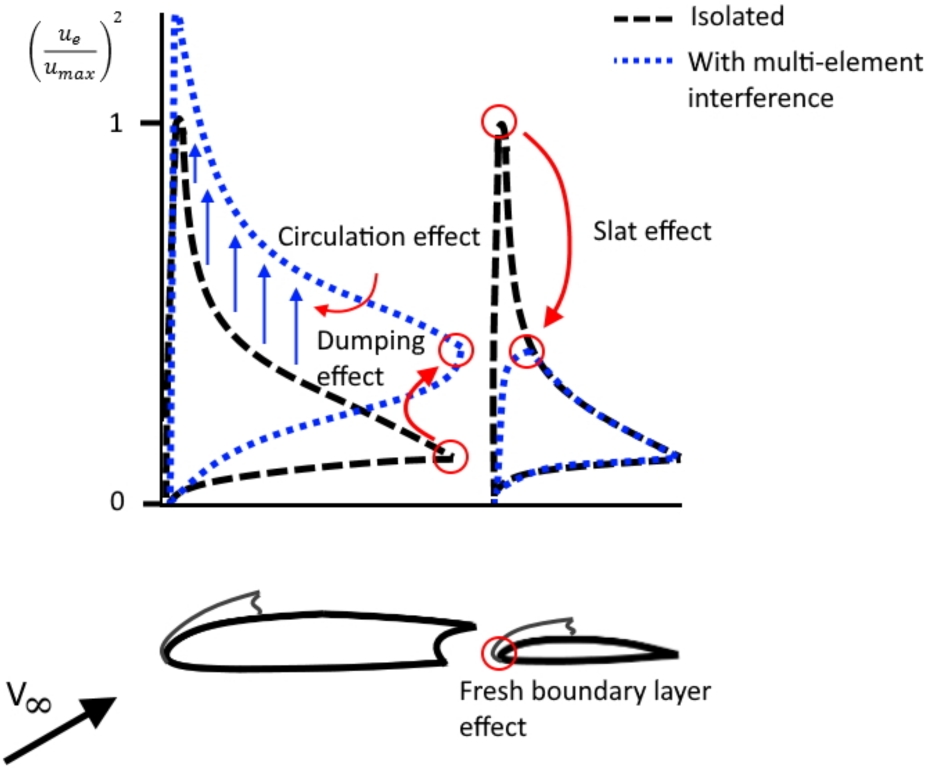

Figure 2.15: Four of the five favourable interaction phenomena of a multi-element airfoil. The slat effect, circulation effect, dumping effect, and the fresh boundary layer effect are schematically shown. The graphs depict a canonical velocity distribution of the isolated airfoils (black periodic stripes) and the altered velocity distribution with multi-element interference (blue dotted).

An adverse interaction effect between a wing and flap occurs when the wake of the wing merges with the boundary layer of the flap. The result is a confluent boundary layer on the flap that is thicker than a boundary layer with no merging. The thicker boundary layer results in earlier separation on the flap [46]. A sketch of the confluent boundary layer effect for a wing with a slat and a flap is shown in Figure 2.16.

Another adverse interaction effect is the wake bursting phenomena as first mentioned by Smith [45].

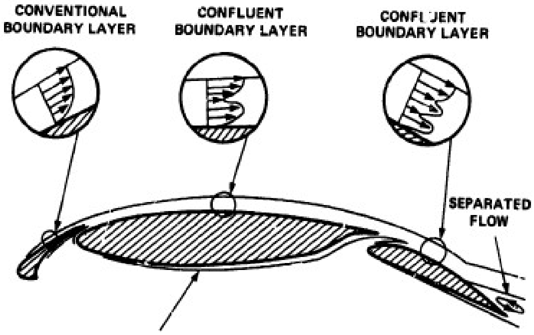

Figure 2.16: Confluent boundary layer effect in which the boundary layer of the wing and trailing flap merge. [47]

Wake bursting is the viscous phenomenon of flow reversal in the wake of the wing due to the off-the-surface pressure recovery exceeding its limits when the adverse pressure gradient is too great. The flow reversal occurs above the flap, reducing the circulation of the flap and causing a decambering effect [48]. The phenomena is therefore observed to decrease lift and increase drag [49]. The wake bursting phenomena has therefore a considerable influence on the performance of high-lift systems. Nevertheless, not much literature is found on the wake bursting phenomena.

3

Research questions and scope

The increased interest in closely-coupled rotor, wing, and flap configurations raises a need for physics-based analysis tools that can capture the most important flow phenomena observed in these configurations while remaining computationally fast. The previous chapter has shown the difficulty of the problem as complex aerodynamic phenomena govern the flow in these interacting rotor and wing environments. Various methods have been explored in literature, but they either are computationally too costly [50] or only capture limited flow phenomena such as only one-way coupling of the rotor and wing [51, 52, 53], exclusion of the rotor normal force [54, 55], slipstream deflection [16, 56], or are limited to wings in cruise configuration [56]. It is for this reason that a physics-based analysis tool is developed and researched in the present work. In this chapter is the scope first presented section 3.1. Following the scope, the research questions and objective are formulated and presented in section 3.2.

3.1. Scope

The focus of this study is on the development of a physics-based aerodynamic numerical analysis tool for wings in high-lift configuration with a closely-coupled tractor open-rotor. The application of the analysis tool is limited to an aerodynamic analysis because it has a large influence on conceptual design choices of future-gen aircraft and because there is not an available sufficient analysis tool presently. The structural analysis and noise of the ORWF configuration is not covered, even though these are important considerations for future DEP research.

The study is limited to interactions between an open rotor and a wing and excludes the interactions between multiple rotors and rotors with other parts of the aircraft frame. The focus will also be on the interactions of one open rotor and wing even though the DEP concepts utilize a multitude of open rotors. This is justified because the external effects between the open rotors and different slipstream immersed wing sections is expected to be small. As such, the influence of multiple open rotors are expected to be modeled relatively easy by superposition of the single open rotor cases. This is supported by the experimental research of Pernas [57] in which is concluded that the effect of three adjacent leading-edge propellers had the nearly the same effect on the lift and drag as three times the effect of a single propeller configuration.

The primary focus of the analysis is the lift prediction and lift augmentation in high-lift configurations. However, also a secondary focus is put on the thrust and drag prediction capabilities and for analysis of cruise configurations. Particular focus is put on the single slotted flap for the high-lift configuration. The analysis of a slotted flap is more difficult than a plain flap due to the increased flow complexity within the gap and on the flap surface. An analysis tool developed for a single-slotted flap is therefore also likely to be able to accurately predict plain flap aerodynamics. Furthermore, single-slotted flaps are also commonly used in presently researched distributed electric propulsion aircraft such as in the Scepter project of NASA where a DEP concept is applied on a light General Aviation (GA) aircraft [9][58] and in the SynergIE project of DLR where a DEP concept is applied to a 70 PAX regional aircraft [3].

Because of the focus on the high-lift case, the Open Rotor-Wing-Flap (ORWF) configuration is coined as the term for a wing with a flap and a tractor open rotor. The ORWF configuration can obviously be divided into three distinct elements: the open rotor, the wing and the trailing-edge flap.

These elements experience aerodynamic phenomena that are present at isolated conditions within a freestream but also phenomena that present themselves due to the interactions between the element. The latter are denoted as (internal) interaction effects. The interactions due to the other parts of the airframe are not considered as these are outside of the scope of the study. These interactions are denoted as external interaction effects.

3.2. Research objectives and questions

Following the knowledge gap found in literature, the objective of the present research is to develop a low-fidelity methodology which can capture the governing aerodynamic phenomena in an open rotor-wing-flap configuration. The methodology is applied by developing a numerical tool in which the methodology can be applied on arbitrary geometries. The tool itself can then be evaluated by comparing the predictions to experiments. Furthermore, the tool is used to evaluate gain insight in the coupling between the elements and its effect on the aerodynamic performance. The main research objective of this thesis can therefore be stated as follows:

> **”To develop and evaluate an aerodynamic analysis tool of an open rotor-wing-flap configuration by the use of low-fidelity aerodynamic methods”**

The research questions supporting this objective are formulated consisting of one main question and several sub-questions to aid the answering of the main question. The main research question of this thesis is:

> **”How well can low-fidelity aerodynamic analysis methods predict the lift and drag augmentation of an open rotor-wing(-flap) configuration?”**

There are two aspects which can be derived from this question. First, low-fidelity aerodynamic methods suited for the problem have to be identified and it has to be determined how they can be integrated into the analysis tool. Second, the analysis tool has to be evaluated on its capability to predict the lift and drag augmentation.

These two aspects are incorporated in sub-questions which allow for the answering of the main research question. The sub-questions for the main research question formulated as follows:

1. How can the low-fidelity aerodynamic methods be applied for modelling the propeller, propeller slipstream, wing and flap flow fields in a coupled fashion?
2. What governing aerodynamic phenomena in an open rotor-wing(-flap) configuration can be captured by low-fidelity aerodynamic methods?
3. How do the lift augmentation and drag augmentation of the analysis tool compare with experimental results?
4. What is the effect of the coupling between the rotor, wing, and flap on the forces of the rotor, wing and flap?

II

Methodology

4

ORWFIS analysis tool

To answer the research questions a numerical tool is developed in Python to perform an aerodynamic analysis of arbitrary open rotor-wing-flap configurations. This numerical tool is promptly called Open Rotor-Wing-Flap Interactions Solver (ORWFIS). ORWFIS is a quasi-3D viscous analysis tool consisting of a rotor, slipstream, inviscid wing, inviscid-viscous coupling, and viscous airfoil module. The different modules and the interfaces between the modules are schematically shown in Figure 4.1. The tool can analyze arbitrary ORWF configurations and requires for its input only the dimensions, positions and orientations of the rotor, wing, and flap as well as the operating conditions. The tool outputs the rotor forces, such as thrust, torque, and normal force, and the wing loading, such as the total lift and drag and their spanwise distributions.

4.1. Analysis modules

The rotor and slipstream analysis module are based on a Blade Element Method (BEM) and vortex based slipstream tube model developed by Willemsen [59]. The rotor module is run first to set up the unsteady BEM and to calculate spanwise circulation distribution required for the set up of the slipstream tube model. Furthermore, the thrust, torque, normal force are calculated and stored. Initially, the inflow of the BEM is set equal to an uniform inflow at the angle of attack of the rotor. The slipstream tube model is set up thereafter using the blade circulation.

The inviscid wing and flap module uses a custom developed vortex ring based Vortex Lattice Method (VLM). The VLM model is set up by creating a mesh on the wing camber surface using the wing planform parameters, airfoil dat file, and the rotor position and diameter. The rotor geometry and position is used in the mesh generation to locally refine the mesh at the slipstream position. The slipstream induced velocities are calculated at each panel control point and added to the VLM.

The inviscid-viscous coupling module corrects the inviscid VLM for viscous, thickness, and compressibility effects through the coupling with the two-dimensional viscous analysis method MSES. The coupling is achieved by decambering the wing through the rotation of the panel normal vectors. The module performs an initial inviscid VLM analysis to calculate an initial guess for the range of effective angles of attack at the strips. The first time the inviscid-viscous coupling module is used for the specific airfoil geometry an interpolation function for the profile drag and normal vector orientations as function of effective angle of attack is created using a Newton-iteration scheme by matching the chordwise lift distribution between a two-dimensional VLM and MSES.

The normal vectors of the VLM panels are then proceeded to be iteratively rotated using the interpolation function for the normal vector orientations using the effective angles of attack for each strip as calculated by the VLM. After convergence is achieved, the profile drag of each strip is calculated using the converged strip effective angles of attack.

In case full-interaction mode is enabled, the wing induced velocities are then used to calculate a new effective angle of attack at the rotor disk center and to calculate the vertical slipstream deformation. The new rotor forces and slipstream induced velocities are thereafter calculated. The change in slipstream induced velocities changes the wing induced velocities at the rotor disk once again. This process is repeated until convergence on the lift, drag, thrust and torque is achieved.

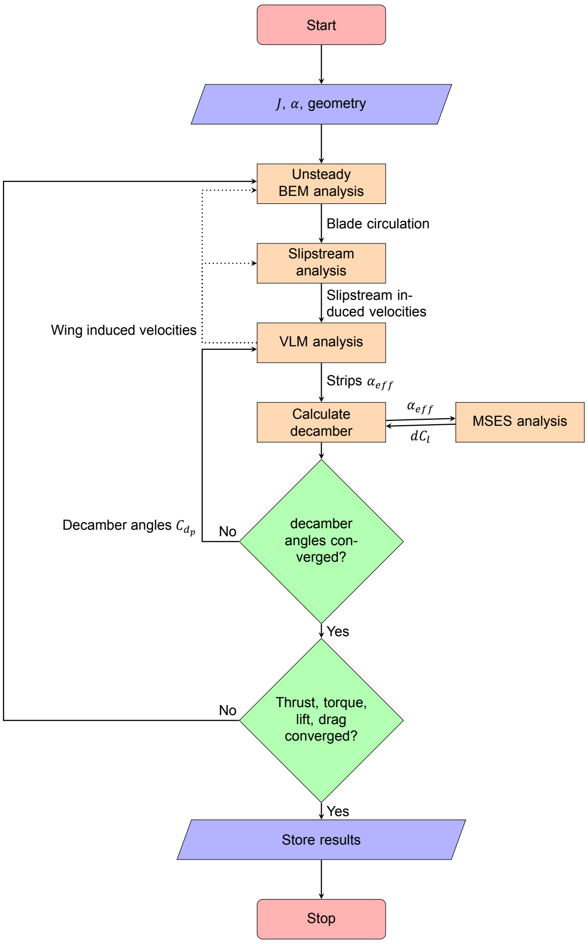

Figure 4.1: Flowchart of ORWFIS

4.2. Limitations and assumptions

The use of the presented analysis modules as well as the integration of these into ORWFIS imposes limitations on the model due to the assumptions accompanying the methods. The main limitations and assumptions of the method are presented here. A more detailed overview of assumptions for each module is provided in their respective chapters.

Assumptions:

1. The rotor inflow can be approximated by an uniform inflow at the effective angle of attack at the rotor center
2. Flow is not separated over the rotor blade
3. The time-averaged slipstream emitting from a rotor is cylindrical
4. The slipstream only deflects in vertical direction and does not deform
5. The slipstream induced velocities do not vary in chordwise direction
6. The wake of the wing and flap are flat and aligned with the freestream direction
7. The flap is not within the wake of the wing
8. Viscous effects are purely two-dimensional and only dependent on the Reynolds number, Mach number, and angle of attack.

9. Sectional lift and drag can be approximated by a two-dimensional airfoil with an uniform inflow at an effective angle of attack.

The assumptions lead to the following limitations:
Limitations:

1. Advance ratio is limited to low- to medium values
2. Rotor angle of attack limited to values where no considerable stall on the rotor blades is present
3. Wing angle of attack and flap deflections are limited to values outside of the stall and post-stall region
4. Wing configurations are limited to nested, plain, and single slotted flaps
5. Flap positions are limited to positions below the main element and outside of the main element wake
6. Limited to low subsonic mach conditions

4.3. Coordinate system

In all the analysis modules is the same global wing body coordinate system used. The origin of the global coordinate system is defined to be at the leading edge of the main element at the spanwise center of the wing. The x-direction is aligned with the reference chord (nested chord) line with positive being in the direction of the trailing edge. The z-direction is defined in the vertical direction with upwards being defined as positive. The y-direction follows from the right-hand rule is aligned in the spanwise direction with the starboard side defined as positive. The coordinate system is schematically shown in Figure 4.2.

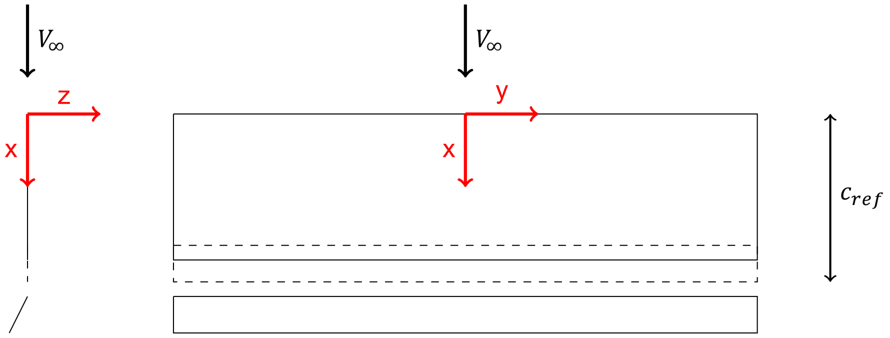

Figure 4.2: Coordinate system used in the present research. Solid line indicates wing with a deployed flap and the dashed indicates the retracted flap.

4.4. Methodology outline

The rotor and slipstream methodology is first presented chapter 5. Thereafter, methodology of the developed VLM for the inviscid wing analysis is described in chapter 6. The finite slipstream correction is described in chapter 7. The viscous solver MSES used for the viscous wing analysis is shortly presented in chapter 8. The developed decamber method in which the inviscid VLM and viscous MSES method are coupled is presented in chapter 9. Lastly, the integration of the different modules, as well as the convergence characteristics and computational time of the complete ORWFIS tool are presented in chapter 10.

5

Rotor and slipstream module

The rotor and slipstream model are required to calculate the generated forces in thrust and lift direction by the rotor as well as to calculate the induced velocities of the rotor slipstream on the wing. For this purpose the code of the Blade Element Method (BEM) and slipstream model of Willemsen [59] are used. The methodology of the rotor and slipstream model are summarized in section 5.1 and section 5.2, respectively. For more information on the methods one can refer to the original source [59].

5.1. Rotor model

The BEM is based on Goldstein's vortex theory with the graded momentum formulation such as used in the programs of XROTOR and QPROP of Drela [60]. In line with the graded momentum formulation, the Prandtl tip loss factor is used to account for the wake induced velocities. The method differentiates itself from XROTOR by using airfoil polars as input for the sectional analysis.

The rotor blades are discretized into radial sections. For each radial section the circulation can be derived from the local angle of attack and the airfoil polars as well from the local induced velocities and tip loss factor. The circulation distribution is then iteratively solved to eventually calculate the lift and drag of each radial section. The thrust and torque can then be calculated by integration along the blade.

The method is limited in advance ratio as the tip loss factor is not valid for high advance ratios [61]. Furthermore, per Goldstein's vortex theory, a Goldstein optimum circulation distribution is assumed and contraction is neglected by assuming the rotor is lightly loaded [62]. However, Willemsen [59] has shown that the method is still valid for rotor blades with arbitrary circulation distribution.

5.1.1. Non-uniform inflow method

A rotor in an ORWF configuration can experience a considerable non-uniform inflow due to the high angle of attack of the rotor plus the large wing induced upwash. This non-uniform flow condition alters the thrust and torque of the rotor and causes the addition of in-plane forces which can have a large contribution to the the total lift. The present rotor model also includes a method for non-uniform and non-axial inflow conditions allowing for the calculation of the change in thrust and torque as well the in plane forces. For this the engineering method of Van Arnhem et al. [63] is used. The method first assumes a quasi-steady solution after which it is then corrected for unsteady effects experienced on the rotor blade as the blade loading changes in rotation.

The quasi-steady method uses the principle of local advance ratio perturbations along different radial stations and azimuthal positions. It is assumed that the change in local advance ratio compared to the freestream advance ratio results in a local change in thrust and torque equal to the change in local thrust and torque when the advance ratio of the entire rotor disk is changed with the local advance ratio. This is schematically shown in Figure 5.1.

In this figure the radial loading distribution as approximated by the present method is shown for a local decrease in advance ratio at a radial section. The loading at the radial section with the perturbed

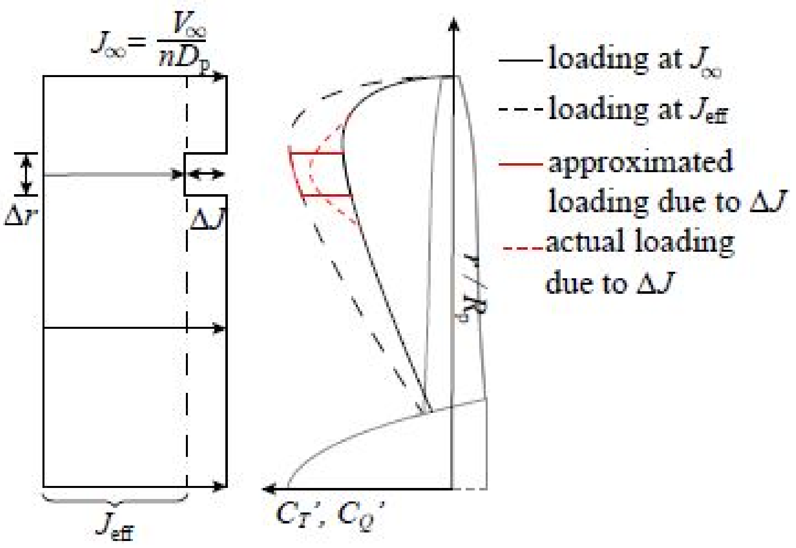

Figure 5.1: Non-uniform inflow modelling on the rotor blades using perturbations in local advance ratio at different radial and azimuthal locations. Figure from Van Arnhem et al. [63]

advance ratio is assumed equal to the loading at that radial section for a rotor disk with an advance ratio equal to the local decreased advance ratio. The change in loading due to a change in advance ratio is calculated from propeller performance maps which are calculated using the BEM for uniform inflow conditions. The method is limited at large changes in local advance ratios due to the limited range of advance ratio in the propeller performance maps. In case the local advance ratio exceeds the available range of advance ratios, the change in loading due to the maximum or minimum advance ratio in the propeller performance map is chosen. As a result, the change in loading is locally limited in some regions at high non-uniform inflow conditions such as for a rotor at an (effective) angle of attack of 10 degrees or higher.

The local changes in loading due to the non-uniform inflow are then integrated over the rotor disk to allow for the calculation of the change in thrust, torque and in-plane forces of the rotor. The total forces of the rotor are then calculated by summing the forces computed by the BEM with uniform inflow with the additional forces due to the non-uniform inflow conditions.

However, the the azimuthal variation in loading causes unsteady effects as the change in bound vorticity is not instantaneous due to the shedding of a vortex in the opposite direction equal to the change in circulation. As a result, the change in loading is smaller and a phase difference between the change in loading and change in local advance ratio occurs. The phase difference especially alters the in-plane forces and as such has to be corrected for. The method corrects for the unsteady effects using the Sears function to determine the transient response of the loading. The non-uniform flow method has been validated by Van Arnhem et al. [63] by comparison with experimental and CFD results and good agreement is achieved with the method slightly under predicting the thrust and normal force.

The rotor method allows for a non-uniform inflow to be provided by defining different local velocities on the discretized rotor disk. However, from a short study it is observed that the variation in wing induced velocities over the rotor disk is small. Therefore, to reduce the computational effort only the wing induced velocity at the center of the rotor disk is calculated. The non-uniform inflow due to the wing induced velocities is then assumed to be equal to a change in angle of attack with the effective angle of attack calculated at the rotor disk center. The rotor inflow is a function of the wing induced velocities which in itself is a function of the rotor loading. The induced velocities at the rotor disk are therefore iteratively solved together with the wing and flap.

5.2. Slipstream model

A model of the slipstream emitting from the rotor is required to calculate the slipstream induced velocities on the wing. The method Willemsen [59] uses a slipstream tube model with modifications to allow for contractions, deflection and azimuthal variation in circulation, called the enhanced slipstream tube model. With the slipstream model the induced velocities can be calculated at arbitrary positions. The slipstream model does not feature slipstream deformation which is observed in literature to be considerable for wings with deflected flaps behind the trailing edge [34, 64]. However, the slipstream is assumed to retain its shape aside from shearing effects quite well ahead of the trailing edge. Therefore, the present slipstream model is still expected to be sufficiently valid for the fidelity of the present methodology for the region ahead of the trailing edge where the slipstream has the largest influence on the wing.

The unmodified slipstream tube model models the slipstream as a straight cylinder with one end of the cylinder bounded by the rotor disk with vorticity distributions along and within. As the rotor emits a helical wake, the slipstream tube can be thought of as a time-averaged rotor wake. Three types of continuous vorticity distributions are used: the axial vorticity parallel to the axis of rotation distributed on concentric cylinders at different radii within the slipstream tube, tangential vorticity parallel to the axial vorticity on the same concentric cylinders and propeller disk vorticity equal to the azimuthal distributed bound vorticity of the rotor blades on the rotor disk. The axial and tangential vorticity is shown in Figure 5.2.

The enhanced slipstream tube model modifies the unmodified model to allow for azimuthal and axial variation of vorticity. The velocity at a certain point induced by the slipstream tube can then be calculated by integrating the induced velocity of the vorticity distributions using the Biot-Savart law. The slipstream tube model does this numerically by discretizing the slipstream tube in axial, radial and azimuthal direction.

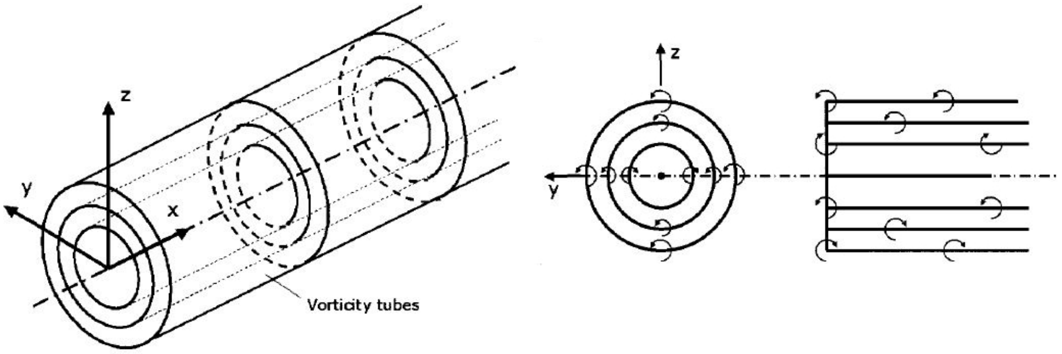

Figure 5.2: The slipstream tube model as represented by a distribution of semi-infinite vortex lines representing the axial vorticity and circular vortex lines representing the tangential vorticity. Figure from Veldhuis [16].

The azimuthal distribution of vorticity in the slipstream tube is a result of the bound vorticity being a function of azimuthal angle at non-uniform inflow conditions. However, as the rotor wake is helical the azimuthal vorticity distribution rotates along the rotation axis in opposite direction of the rotor the further the wake travels axially. This rotation in azimuthal vorticity distribution is approximated with the ratio of the rotor angular speed and the freestream velocity times the axial distance as shown in Figure 5.3.

The contraction of the slipstream tube model depends on the axial induced velocities distribution in axial direction. The method of Willemsen [59] uses analytical solutions of Conway [65]. These axial induced velocities are then used to calculate the slipstream contraction following from the conservation of mass. The contraction differs radially but the mean is used for the contraction of the slipstream boundary at different axial positions.

Lastly, the slipstream tube model is modified to allow for slipstream deflection. The slipstream deflection is modeled by vertically translating discrete annular segments of the slipstream tube at different axial positions as shown in Figure 5.4. The vertical translation of an annular segment is calculated using the ratio of the local external induced vertical velocity and the freestream velocity as shown in Equation 5.1. These external induced velocities are calculated similarly to the wing induced velocities at the rotor disk by summing the induced velocity of every vortex ring at each annular segment center.

$$\Delta z = \frac{w_{ext}}{V_\infty} \Delta x \tag{5.1}$$

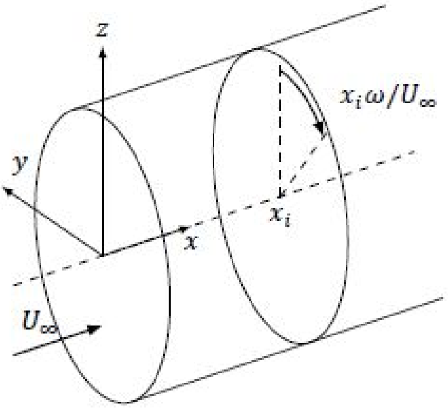

Figure 5.3: Azimuthal rotation of the vorticity in the slipstream as function of the axial distance from the rotor disk. Figure from [59].

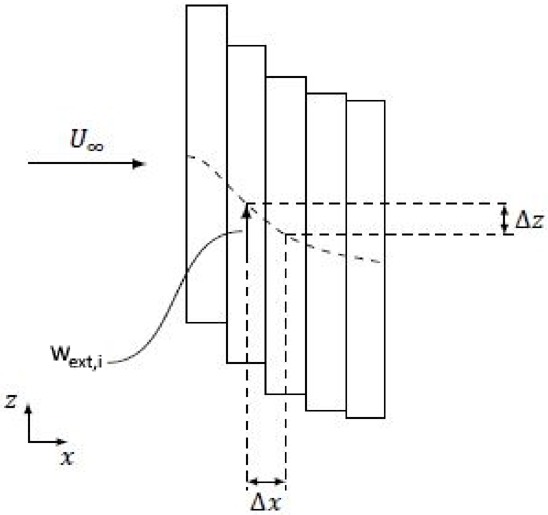

Figure 5.4: Slipstream tube deflection is modeled by translating each axial station in vertical direction. Figure from [59]

6

Inviscid wing-flap module: Vortex Lattice Method

The inviscid wing-flap module is used to calculate the three-dimensional inviscid effects surrounding the wing and flap. The circulation distribution of the wing and flap and the velocities induced by the circulations are calculated. The lift and induced drag quantities can then be derived from the circulation distribution.

A vortex ring VLM is used to solve the linearized potential flow equations in a discretized fashion. The methodology is presented in section 6.1. The methods for the force derivation from the circulation distribution is thereafter presented in section 6.2. Finally, the vortex ring VLM is verified against other vortex based solvers as shown in section 6.4.

6.1. Vortex ring formulation

The VLM formulation using vortex rings as described in Katz and Plotkin [66] is used to compute the three-dimensional inviscid lift and induced drag of the wing. The VLM is based on the theory of potential flow. The main assumptions for this method are therefore that the flow is **inviscid**, **irrotational** and **incompressible**. Furthermore, as the panels are placed only on the camber line and not the wing surface, **thickness is neglected**.

The wing is discretized into n chordwise panels and m spanwise panels on each lifting surface camber line. In case of a single slot flap configuration, the main wing and flap are discretized as two separate lifting surfaces. The choice of a panel discretization on the camber surface instead of a more conventional planar mesh is made to capture the considerable spatial variations in the external induced velocities of the slipstream of a rotor more accurately. For the slipstream immersed wing sections the mesh is adjusted such that the rotor axis is at the spanwise center of a panel and the slipstream boundary coincides with the edges of the panel. The singular nature of the vortex lines impose additional restrictions on the mesh to avoid non-physical induced velocities. The same amount of spanwise panels are therefore used for both the wing and flap to make make the chordwise vortex lines aligned with each other. The mesh also requires a finer mesh at locations with large circulation gradients. The spanwise panel distribution is therefore sinusoidal with a finer mesh near the tips as the spanwise circulation gradients increase here. Furthermore, the separate sections for the slipstream immersed wing allow for local mesh refinement to accommodate the steep circulation gradients due to the slipstream induced velocities. An example of a mesh generated for a multi-surface cambered wing with two symmetric rotors at the center of the semi-span is shown in Figure 6.1.

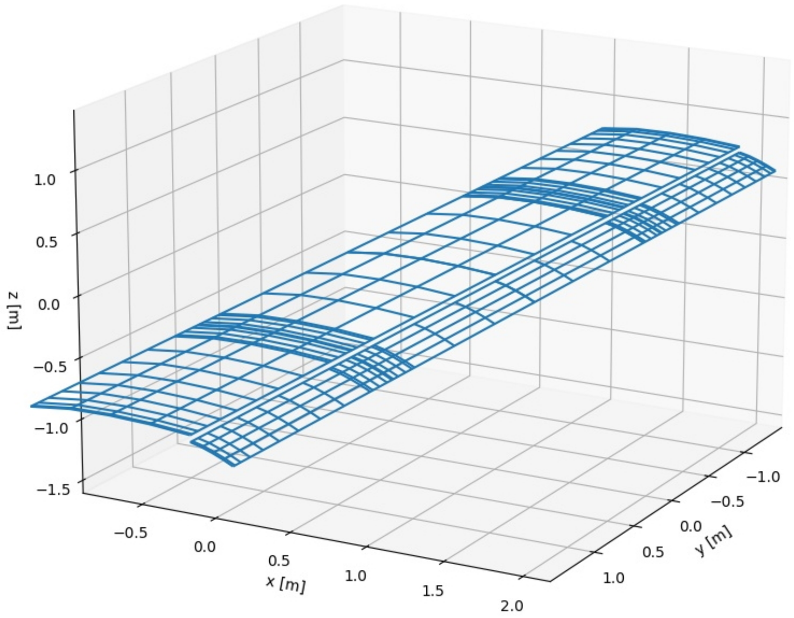

Figure 6.1: Example of a mesh generated by the present method for a multi-surface cambered wing with rotors at 50% semi-span.

A vortex ring is generated for each panel consisting of four straight vortex line segments with a constant vorticity. The front and rear bound vortex lines are positioned on the quarter chord of the local panel and of the panel rear of the local panel, respectively. The trailing vortex lines of the vortex ring connect the two bound vortex lines. The collocation points are placed on the three-quarter chord point of the panels in the spanwise center with the normal vector orthogonal to the camber line at the collocation point. A schematic of a lifting surface with vortex rings is shown in Figure 6.2.

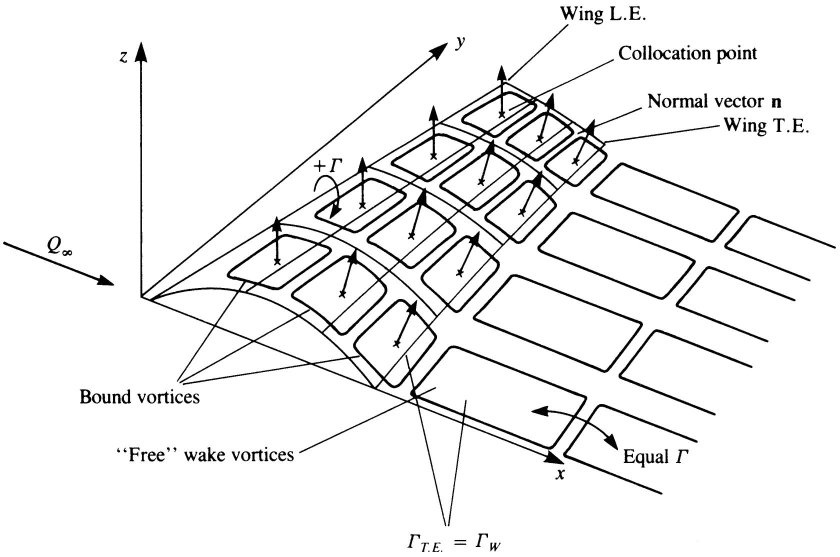

Figure 6.2: Vortex ring model on a camber surface of a wing. [66]

To satisfy the three-dimensional trailing edge condition of zero vorticity, a wake is included extending infinitely far into the far-field with constant circulation strength equal to the strength of the vortex ring at the trailing edge is. The wake is assumed to be flat and can be aligned either with the chord line or the free-stream. The freestream aligned wake is a better representation of reality whilst the body aligned wake is computationally more efficient as it does not have to be recomputed for different angles of attack [66]. In case of a wing with a slotted flap a wake emerges from each of the trailing edges. These separate wakes are also modelled in the present theory by prescribing two fixed flat wakes behind each surface as is also used by Bissonnette and Bramesfeld [67] in a non planar VLM.

In reality, the wakes are force-free and follow the local velocity such that the wake rolls up near the tip. In the research of Bissonnette and Bramesfeld [67], the results of a free-wake model is compared with a fixed-wake model in a VLM for a wing with a slat and a flap. These results are also compared with experimental data of a NASA wind tunnel test campaign. The findings of this research showed minimal differences in lift and drag between the free-wake and fixed-wake model, supporting the use of a fixed-wake model in this research. However, it should be noted that the assumption of a fixed-wake might yield larger errors in case slipstream interactions are present, as the slipstream considerably deforms the wake of the wing. The deformation of the wake is firstly caused directly by the induced velocities of the slipstream and secondly caused indirectly by the strong trailing vortices generated by the large spanwise circulation gradient on the slipstream-immersed wing sections. This could have significant influence on the wake induced velocities on the closely located flap. However, no research is found on the significance of this effect in the presence of a propeller slipstream.

A Neumann boundary condition is enforced on each collocation point ensuring that the velocity normal to the camber line is zero at all the collocation points. The normal velocity at the panel collocation point is a superposition of the freestream velocity, vortex ring induced velocities, and external velocities such as slipstream induced velocities. The Neumann boundary condition for a local panel is therefore enforced with Equation 6.1, where $\overline{V}_{ind}$, $\overline{V}_{\infty}$ and $\overline{V}_{ext}$ are the induced velocities of the vortex rings, the freestream velocity and the external induced velocities, respectively, and $\overline{n}$ represents the normal vector of the camber line at the collocation point.

$$\left(\sum_{j=0}^{N}(\overline{V}_{ind_j}) + \overline{V}_{\infty} + \overline{V}_{ext}\right) \cdot \overline{n} = 0 \tag{6.1}$$

The freestream velocity and external induced velocities at each collocation point are known a priori and can be moved to the right-hand side. The induced velocities of the vortex rings are unknown and a function of the vortex ring circulation. Rewriting Equation 6.1 yields Equation 6.2. where the a coefficient represents the induced velocity of panel j with unit circulation strength normal on the collocation point of panel i.

$$\sum_{j=0}^{N} a_{ij}\Gamma_j = -\left(\overline{V}_{\infty} + \overline{V}_{ext}\right) \cdot \overline{n} \tag{6.2}$$

The solvable linear system of equations of Equation 6.3 is obtained when the boundary condition is enforced on each collocation point, with AIC denoting the Aerodynamic Influence Coefficient matrix and RHS denoting the Right Hand Side vector with the external induced velocities.

$$\overline{\overline{AIC}} \cdot \overline{\Gamma} = \overline{RHS} \tag{6.3}$$

The set up of the aerodynamic influence coefficient matrix requires the calculation of the induced velocity of every vortex ring at every collocation point for unit circulation. The induced velocity of a straight vortex line segment with constant vorticity can be calculated according to the modified Biot-Savart law shown in Equation 6.4, where $\overline{r}_1$ and $\overline{r}_2$ represents the vector from the start and end point of the line segment towards an arbitrary point in space, respectively. These position vectors are schematically shown in Figure 6.3. The modification removes the singularity when the point of evaluation lies on the virtual extension of the finite vortex line as described in [68]. The induced velocity of one vortex ring is then the summation of the induced velocities of the six vortex line segments.

$$\overline{V}_{ind_{\Gamma=1.0}} = \frac{1}{4\pi}\frac{(r_1 + r_2)(\overline{r}_1 \times \overline{r}_2)}{r_1 r_2 (r_1 r_2 + \overline{r}_1 \cdot \overline{r}_2)} \tag{6.4}$$

The wake is represented by a vortex ring with its trailing vortices going towards the rear bound vortex line infinitely far into the far-field such that the influence of the rear bound vortex is negligible. The induced velocities of these trailing vortices are calculated using the modified Biot-Savart law for a semi-infinite straight vortex line as presented in Equation 6.5 [68], where $\overline{r}$ represents the vector from the start point of the semi-infinite line towards an arbitrary point in space, and $\overline{n}_\infty$ represents the unit direction vector of the semi-infinite vortex line. The influence of the trailing vortices of the wake are then the summation of the two semi-infinite vortex lines.

$$\overline{V}_{ind_{\Gamma=1.0}} = \frac{1}{4\pi}\frac{\overline{n}_\infty \times \overline{r}}{r(r - \overline{n}_\infty \cdot \overline{r})} \tag{6.5}$$

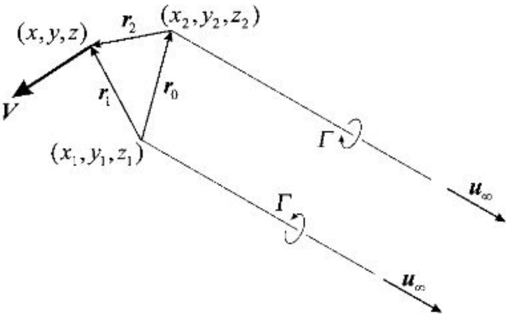

Fig. 2 Position vectors describing the geometry for a horseshoe vortex.

Figure 6.3: Vector definitions for a finite vortex line segment and a semi-infinite vortex line segment. [68]

6.2. Lift and drag derivation

The inviscid lift and drag can be computed using the solved panel circulations. The lift can be computed by calculating the forces on the body itself using the Kutta-Joukowski relation. According to the Kutta-Joukowski relation the lift is a function of the circulation of the bound vortex lines. As the circulation of the rear bound vortex of a forward panel opposes the front bound vortex of the local panel, the lift is a function of the difference in circulation of these two. This results in Equation 6.6 for the panels at the leading edge and Equation 6.7 for the remaining panels. The total lift is then calculated by summing the lift of the individual panels.

$$\Delta L = \rho V \Gamma \Delta y \tag{6.6}$$

$$\Delta L = \rho V (\Gamma - \Gamma_{front}) \Delta y \tag{6.7}$$

The velocity used for the lift calculation is the projection of the effective velocity in the direction of the free stream velocity. The effective velocity includes the slipstream induces velocities but excludes the wing induced velocities as is also the convention in Katz and Plotkin [66]. The effective velocity is then calculated with Equation 6.8.

$$V = V_\infty + (\overline{V}_{ext}) \cdot \frac{\overline{V}_\infty}{V_\infty} \tag{6.8}$$

The local lift coefficient is derived from the panel lift and is used for the chordwise lift distribution used in the present method. The local lift coefficient can be thought of as the VLM equivalent of a pressure coefficient. However, as the VLM assumes zero thickness only the pressure difference between the upper and lower surface can be calculated. Furthermore, it only indicates the pressure difference in the lift direction as it is derived from the panel lift. The local lift coefficient is calculated according to Equation 6.9.

$$dC_l = \frac{\Delta L}{S_{panel} q_\infty} \tag{6.9}$$

The inviscid drag, or induced drag, can also be comparatively to the lift computed on the body. However, the use of a Trefftz plane analysis is preferred instead to provide a more accurate estimate of the induced drag. Using the derivation of Katz and Plotkin [66] from the integral form of the momentum equation, the induced drag can be calculated at the Trefftz plane by Equation 6.10. For the vortex ring VLM solver, a rigid flat wake is assumed and therefore the wake span is assumed to be equal to the wing span. The downwash is calculated according to the induced velocities of the trailing vortices in the far-field.

$$D_i = -\frac{\rho}{2}\int_{-b_w/2}^{b_w/2} \Gamma(y) v_{n_w} dy \tag{6.10}$$

The potential at the Trefftz plane is altered in case a slipstream due to a rotor is present. As a result, two new terms arise in the drag equation as described in Veldhuis and Heyma [69]. The resulting equation for the induced drag is shown in Equation 6.11.

$$D_i = -\frac{\rho}{2}\int_{-b_w/2}^{b_w/2} \Gamma(y) v_{n_w} dy - \rho\int_{-b_w/2}^{b_w/2} \Gamma(y) v_{n_r} dy - \frac{\rho}{2}\iint_{S_p} (v_r^2 + w_r^2) dS \tag{6.11}$$

The first term is for a wing without a rotor and equal to Equation 6.10. The second term is due to the rotor and wing interaction effects and lastly the third term is the rotor drag. The rotor drag is ignored as it is not consistent with the rotor model used in this research. The normal induced velocity of the wing, v_{n_w} is determined by calculating the induced velocities of the infinite trailing vortices at the far-field projection of the trailing-edge panel control points. The normal induced velocity of the rotor, v_{n_p}, is determined from the induced velocities calculated by the slipstream model at a sufficient streamwise distance from the rotor disk such that a far-field assumption can be used.

6.3. Infinite span analysis

It is of interest to analyse an ORWF configuration for an infinite span wing, referred here to as a mode analysis. The mode analysis removes the dependency on the spanwise position such that more generalized cases of slipstream interactions can be explored. As the lift augmentation is the central topic of this research, spanwise positions are of less importance.

To remove the tip effects from the VLM analysis virtual panels with infinite span are placed at the edges of each wing surface within the segment, as is schematically shown in Figure 6.4. The infinite span of the virtual panels allows for the tip vorticity to cancel with the trailing vortex of the virtual panel without violating the Helmholtz theorem which states that a vortex line cannot end in a fluid. The collocation points of the virtual panels are assumed to be infinitely far away from the wing segment negating the influence from the neighbouring vortex panels, essentially representing a two-dimensional thin-airfoil panel method. The circulation strength of the virtual panels can therefore be calculated with a two-dimensional thin-airfoil vortex panel method with only chordwise influence of panels with only infinite bound vortex lines. The two-dimensional vortex panel method used for this purpose is simply a modified two-dimensional version of the vortex ring VLM using the same panel positions and normal vectors orientations as the VLM.

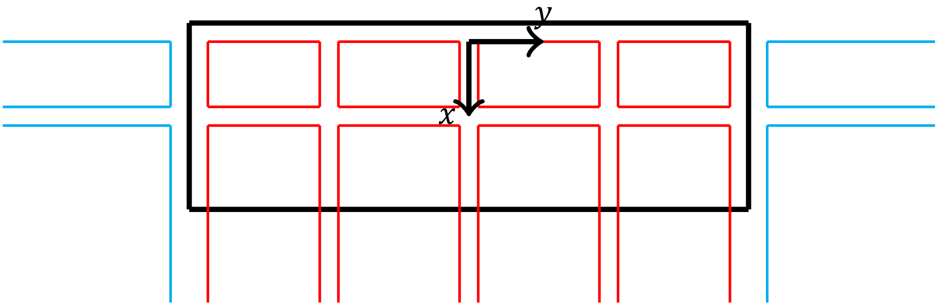

Figure 6.4: Top-view of a VLM mesh on a wing with virtual panels for infinite span analysis. The red lines indicate vortex rings and the cyan lines the virtual panels with semi-infinite vortex lines placed at the mesh boundaries.

The influence of the virtual panels on the physical panels can be added as 2xn additional columns, where n is the total amount of chordwise panels, in the aerodynamic influence coefficient matrix. The

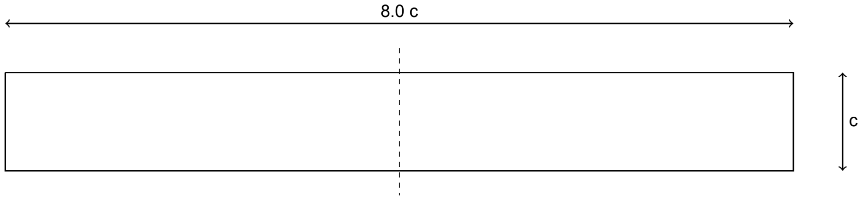

Figure 6.5: Single surface wing planform used for VLM validation.

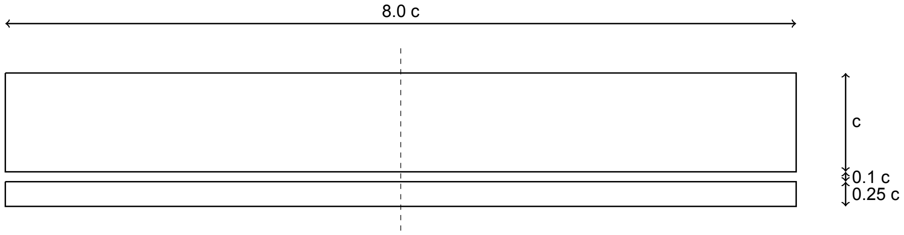

Figure 6.6: multi-surface wing planform used for VLM validation.

aerodynamic influence of each virtual panel is the summation of the influence of two semi-infinite vortex lines for the front and rear vortex bounds and a finite vortex line segment for the trailing vortex. For the virtual wake panel, the influence is only of two semi-infinite vortex lines with one for the front bound vortex and one for the trailing vortex. As the circulation strength of the virtual panels is known a priori with the two-dimensional vortex panel method, the AIC columns related to the virtual panel influence are moved together with the vector of virtual panels circulations to the RHS. The virtual panels are therefore included in the analysis by the addition of one term in the RHS as shown in Equation 6.12.

$$\overline{RHS}_{infinite} = \overline{RHS} - \overline{\overline{AIC}}_{virtual} \cdot \overline{\Gamma}_{virtual} \tag{6.12}$$

6.4. VLM verification

The vortex ring VLM implementation is verified by comparing the results with other VLM software programs such as AVL [70] and XFLR5 [71] using an identical wing geometry. Both AVL and XFLR5 are used with their planar horse-shoe VLM implementation. The validity of the vortex ring VLM is checked for both a single surface wing and a multi-surface wing as used for high-lift configurations.

The wing that is used for the single surface verification is a straight rectangular wing with an aspect ratio of 8.0. The multi-surface verification wing additionally has a surface behind the trailing edge of the single surface wing with a chord equal to 25% of the single surface wing chord and 10% single surface wing chord chordwise distance between the two surfaces. All surfaces used have a NACA4412 airfoil and zero incidence with respect to each other. Both wing planforms are shown in Figure 6.5 and Figure 6.6.

As the VLM results are dependent on the mesh settings, the panel settings of the vortex ring VLM, AVL and XFLR5 are shown in Table 6.1 for reproducibility. The amount of panels is equal for all lifting surfaces in the VLMs.

Table 6.1: Mesh settings used in the VLM validation of all three solvers.

Solver	# Spanwise panels (for semi-span)	Spanwise spacing	# Chordwise panels	Chordwise spacing
Vortex Ring	24	Sine	8	Uniform
AVL	24	Cosine	8	Cosine
XFLR5	24	Sine	8	Cosine

Single surface

The lift curve and spanwise lift distribution for the different VLM solvers for the single surface geometry are shown in Figure 6.7. The lift curve of the vortex ring is shown to correspond well with the results of AVL and XFLR5. However, slight discrepancies are observed with AVL at higher angles of attack due to smaller lift curve slope. This is likely caused by the small angle approximation utilised in AVL which is not used in the vortex ring VLM, increasing the error at larger angles of attack. A close constant discrepancy with XFLR5 is observed due to an difference in zero-lift angle of attack. These discrepancies are likely the result of the difference in normal vector determination. The vortex ring method derives the normal vector orientation from the camberline slope of the airfoil whilst XFLR5 uses the vector normal to the local panels, which is more prone to discretization errors. Furthermore, the vortex rings are located on the camber line while XFLR5 has vortices located on a planar surface, which allows the vortex ring VLM to capture the camber better and, therefore, shifts the lift curve more to the left than XFLR5.

The trend of an over-prediction in lift coefficient for the vortex ring VLM compared to XFLR5 is likewise observed in the spanwise lift distribution, although the shapes of the lift distribution correspond well with each other.

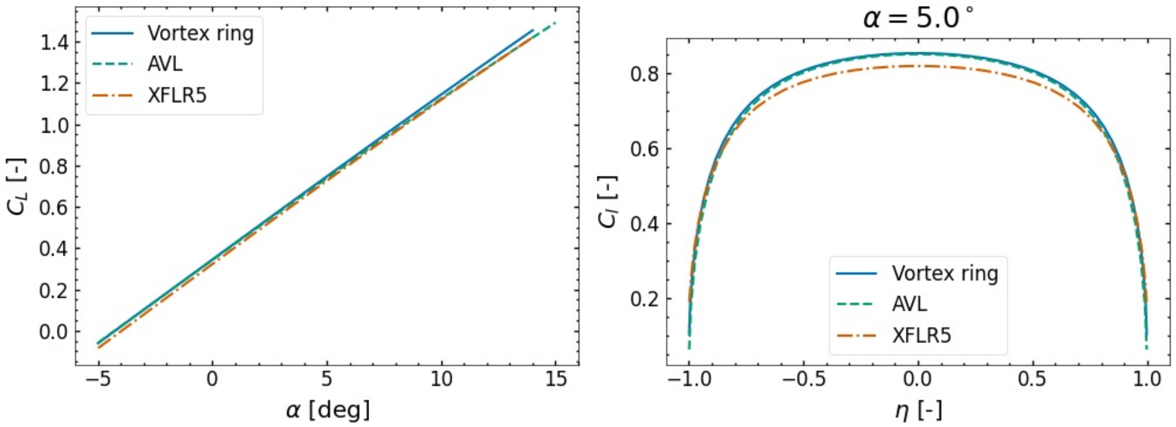

Figure 6.7: Lift polar (left) and lift distribution (right) as predicted by three different inviscid solvers for a cambered rectangular single-surface wing.

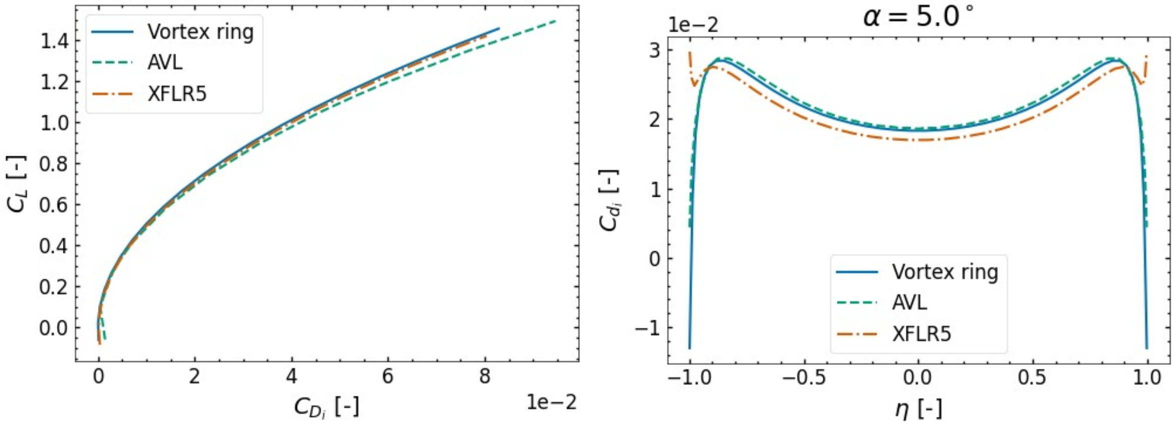

Figure 6.8: Drag polar (left) and induced drag distribution (right) as predicted by three different inviscid solvers for a cambered rectangular single-surface wing.

The drag polar and spanwise induced drag distribution are shown in Figure 6.8. The vortex ring VLM is shown to correspond well with XFLR5 for the whole range of design points analyzed. A discrepancy is observed between the vortex ring and AVL for larger lift coefficients with AVL estimating slightly larger induced drag values. It is not certain what the reason for this is but a potential reason could be due to a small angle approximation used in AVL.

For an angle of attack of five degrees, the spanwise induced drag distribution corresponds well with AVL. The induced drag distribution of XFLR5 is seen to be underestimated along the span compared to AVL and the vortex ring method. This is attributed to the underestimated lift coefficient compared to AVL and the vortex ring VLM as observed in the lift curve of Figure 6.7, resulting in a lower induced drag distribution. This is supported by the fact that the total induced drag is observed to correspond well between XFLR5 and the vortex ring VLM for equal lift coefficient in the drag polar of Figure 6.8.

Multi-surface

The lift curve and spanwise lift coefficient distribution for the multi-surface wing geometry is shown in Figure 6.9. The vortex ring VLM is observed to be slightly underestimated compared to AVL and slightly overestimated compared to XFLR5. The discrepancy with AVL increases with larger angles of attack, which is attributed to the use of the small angle approximation in AVL which produces increasing errors at larger angles. The overestimation of the vortex ring VLM compared to the XFLR5 is, likewise as for the single-surface solution, attributed to the presence of the vortex ring panels on the camberline instead of on the chord line as is the case for XFLR5.

The deviations in lift are observed in the spanwise lift distribution as well, with an overall over- or underestimation of the lift along the span compared with XFLR5 and AVL. This follows directly from the observations made in the total lift coefficient at an angle of attack of 5 degrees and is attributed to the former mentioned causes.

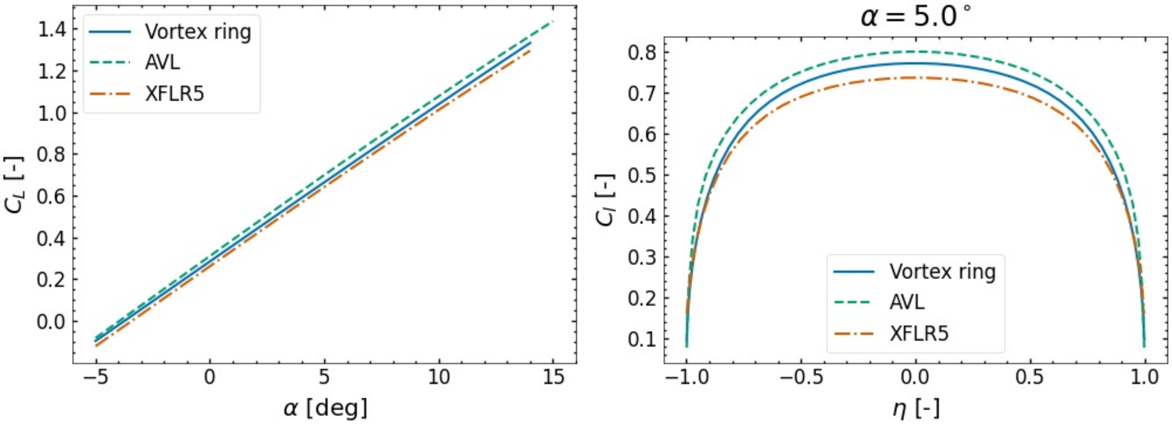

Figure 6.9: Lift polar (left) and lift distribution (right) as predicted by three different inviscid solvers for a cambered multi-surface rectangular wing.

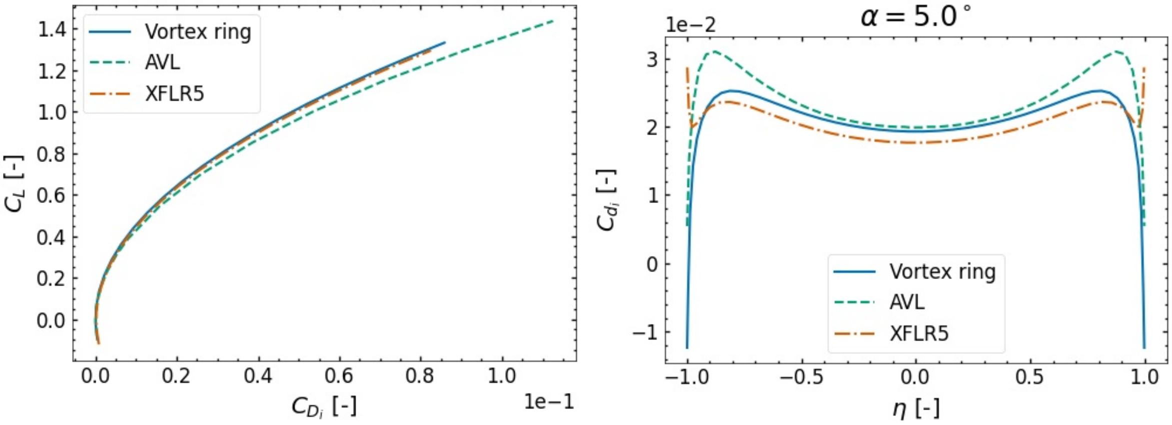

Figure 6.10: Drag polar (left) and induced drag distribution (right) as predicted by three different inviscid solvers for a cambered multi-surface rectangular wing.

The drag polar and spanwise induced drag distribution is shown in Figure 6.10. The drag polar of the vortex ring VLM corresponds well with the drag polar of XFLR5. AVL is observed to increasingly overestimate the induced drag at larger lift coefficients as was also observed for the single-surface wing geometry. The cause of this discrepancy is not certain but could be due to the small angle approximation used in AVL.

The spanwise induced drag distribution of the vortex ring VLM is observed to be lower than the AVL prediction and higher than the XFLR5 prediction. The lower induced drag of the XFLR5 analysis is the result of the underestimation of the lift coefficient at this angle of attack, reducing the overal induced drag. The overestimation of the induced drag for AVL compared to the vortex ring VLM is partially due to the overestimation of the lift coefficient as observed in the lift polar. Compensating for the lift coefficient, AVL still overestimates the induced drag as seen in in the drag polar, which is attributed to the small angle approximation employed in the method.

The vortex ring VLM is further verified for a multi-surface geometry with the panel code and experimental data of Feistel, Corsiglia, and Levin [72] in which a tandem configuration of a high aspect ratio canard and wing is analysed using a free-wake planar VLM and tested in a wind tunnel. The canard and wing both have an aspect ratio of 6, with the canard having a span of 1.29 meters and an incidence angle of 2 degrees and the wing a span of 1.83 meters with a zero incidence angle. The horizontal stagger between the quarter chord of the canard and wing is 1.63 wing chord and the vertical gap is 0.5 wing chord, with the wing below the canard. A sketch of the model is shown in Figure 6.11. The wind tunnel tests of Feistel, Corsiglia, and Levin [72] have been ran on a wing chord based Reynolds number of 1.4 million.

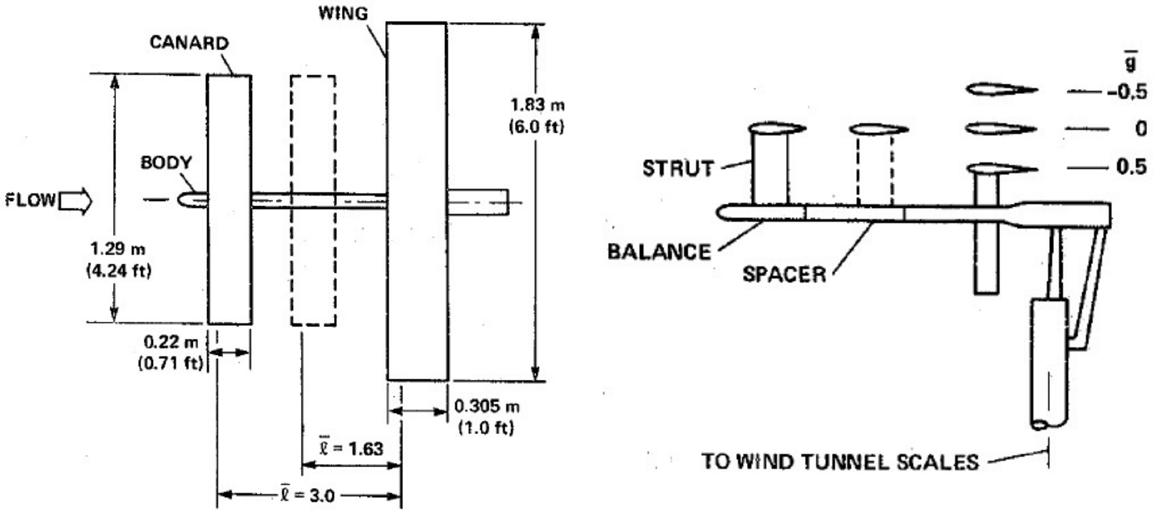

Figure 6.11: Top view (left) and Side view (right) of the geometry used in the panel analysis and wind tunnel tests of Feistel, Corsiglia, and Levin [72]. The canard position with a stagger of 1.63 and the wing position with a gap of 0.5 is used for the present verification.

The lift polar with the results of the present vortex ring VLM results together with the planar VLM and wind tunnel measurements of Feistel, Corsiglia, and Levin [72], is shown in Figure 6.12. The lift polar of the planar VLM of the literature is shifted by 1.4 degrees to the left as is also done in the paper of Feistel, Corsiglia, and Levin [72]. This is done to compare the slopes of the polars as the zero-lift angle of attack is overestimated by the planar VLM due to ”an inadequate representation of the camber” [72].

There are notable observations between the vortex ring VLM and the results from literature. First of all, the zero-lift angle of attack of the vortex ring VLM havs a good agreement with the experimental measurements, unlike the planar VLM with an error of 1.4 degrees due to inadequate camber representation. However, the lift curve slope is observed to be underestimated by the vortex ring VLM compared to the VLM and experimental measurements of the literature. The discrepancy between the vortex ring VLM and the experimental measurements are likely due to the lack of thickness modelling. The GAW-2 airfoil that is used in this analysis has a 12% thickness to chord ratio and, according to

Abbott and Von Doenhoff [73], the theoretical lift curve slope is about 9% greater for a 12% thick airfoil which covers the discrepancy observed here. The discrepancy with the planar VLM can not readily be explained but could be caused by the free-wake modelling used instead of a fixed-wake used in the present vortex ring method.

The drag polar with the vortex ring VLM results together with the planar VLM and wind tunnel measurements of Feistel, Corsiglia, and Levin [72], is shown in Figure 6.13. For the wind tunnel measurements, the zero-lift drag is subtracted to remove the effect of profile drag from the comparison. Good agreement is achieved for lift coefficients up to 1.0. At larger lift coefficients the drag is observed to be slightly underestimated compared to the experimental values and planar VLM. The cause of this is not entirely certain. One cause could be the modelling of the wake as fixed in the vortex ring VLM compared to free as in the experiment and the planar VLM of Feistel, Corsiglia, and Levin [72]. However, in the paper of Bissonnette and Bramesfeld [67] it was instead shown that a fixed wake has a higher induced drag compared to a free wake for a multi-element geometry. The discrepancy is, however, not disastrous as the error remains relatively small, only occurs at higher angles of attack at which the total drag prediction is less accurate either way, and because the drag prediction is only a secondary objective of the present research compared to the lift prediction.

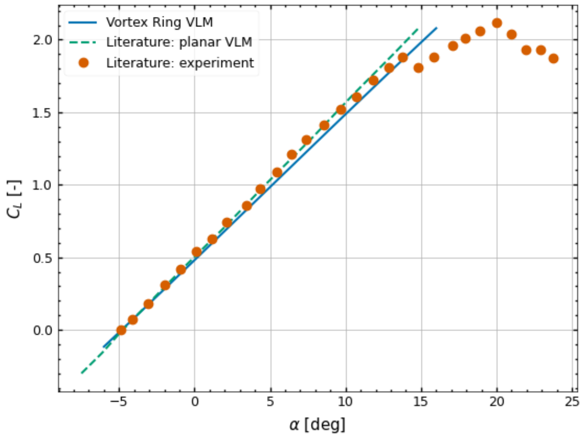

Figure 6.12: Lift polar as predicted by the vortex ring VLM and the planar VLM of Feistel, Corsiglia, and Levin [72] as well as wind tunnel measurements of Feistel, Corsiglia, and Levin [72] for a tandem canard-wing configuration.

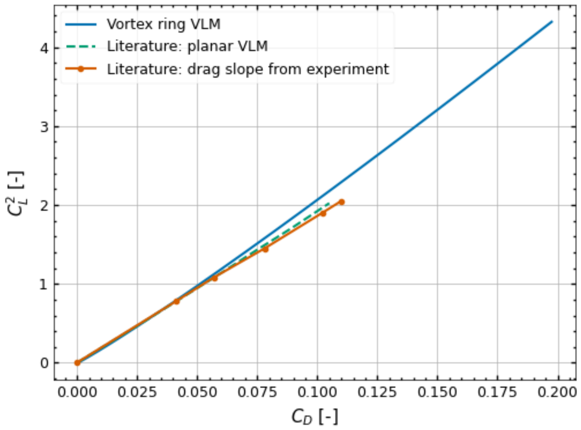

Figure 6.13: Drag polar as predicted by the vortex ring VLM and the planar VLM of Feistel, Corsiglia, and Levin [72] as well as wind tunnel measurements of Feistel, Corsiglia, and Levin [72] for a tandem canard-wing configuration.

7

Finite slipstream correction

The slipstream of the rotors induce a velocity on the VLM panels which have to be included in the VLM solver to include the slipstream influence. These induced velocities can be collected under the external induced velocity term on the right-hand-side of Equation 6.2 and therefore be included in the RHS term of Equation 6.3.

However, the consecutive lift calculation using the Kutta-Joukowski theorem as shown in Equation 6.7 with the effective velocity as calculated with Equation 6.8 results in an over-estimation of the lift due to the slipstream induced velocities as described by Nederlof [74]. This over-estimation is a consequence of the limitations of the Kutta-Joukowsky theorem which assumes an uniform inflow extending to infinity. In contrast, the velocity profile of the slipstream is finite in dimension and therefore is less effective than a to infinite extending inflow with the same slipstream velocity.

7.1. Three-dimensional image method

In the present research the jet correction of Rethorst [75] for three-dimensional wings in a circular jet with uniform velocity is used. The slipstream has to be corrected for both the finite slipstream height as well as width as Nederlof [74] has shown that only correcting for the finite slipstream height still results in a considerable over-estimation of lift augmentation of a wing in a jet. In this correction only the axial slipstream induced velocities are corrected and not the tangential velocities. However, Nederlof [74] has shown that the discrepancy of lift caused by the tangential velocities in a finite slipstream is negligible compared to the axial velocities. Furthermore, additional modifications are made to allow for arbitrary spanwise positions of the slipstream, arbitrary axial velocity profiles, vertical misalignment of jet center and wing chord line. These modifications are following from the methodology used by Willemsen [59]. Finally, the correction is modified to allow for the implementation in a vortex ring VLM.

The jet correction is applied by adding an additional term to the induced velocities of the panels such that these are reduced to account for the reduction in circulation as a result of the finite jet. As such the equation enforcing the flow tangency boundary condition for each panel becomes Equation 7.1 leading to the addition of a G matrix to the linear system of equations as shown in Equation 7.2.

$$\sum_{j=0}^{N}(a_{ij} - G_{ij})\Gamma_j = -\left(\overline{V}_\infty + \overline{V}_{ext}\right) \cdot \overline{n} \tag{7.1}$$

$$\left(\overline{\overline{AIC}} - \overline{\overline{G}}\right) \cdot \overline{\Gamma} = \overline{RHS} \tag{7.2}$$

In Rethorst [75] the jet correction method is applied to a wing with a circular jet in the spanwise center with uniform axial velocity bounded by an infinite flow with the freestream velocity. The wing is modeled with horse shoe vortices in a discrete lifting line method. As such, it is assumed that the wing is planar. An example of a wing with the circular jet and a single horse shoe vortex as used in the method is shown in Figure 7.1.

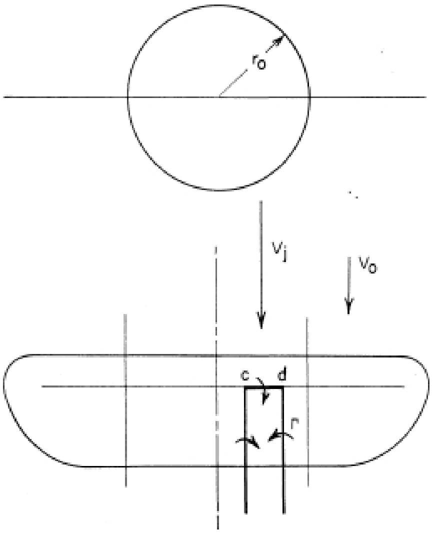

Figure 7.1: The slipstream and wing vortex model used by the jet correction. The jet is taken to be cylindrical in the center of the wing with a constant axial velocity, V_j, which is larger than the velocity outside of the jet, V_o. A series of spanwise horseshoe vortices is used to model the wing. Modified from Rethorst [75].

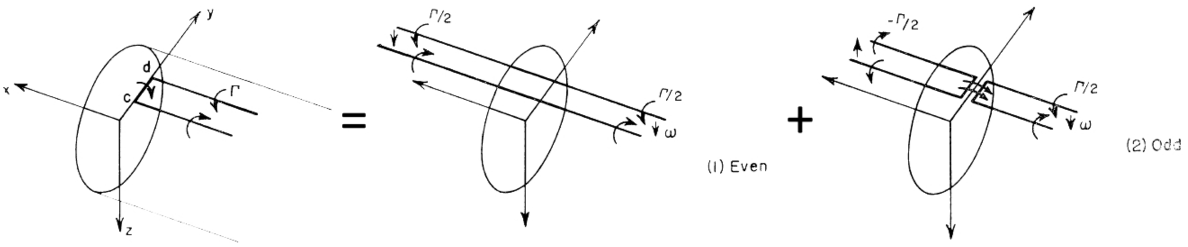

Figure 7.2: The representation of a horseshoe vortex as a summation of two infinite trailing vortices, even part, and two symmetric horseshoe vortices, odd part. Modified from Rethorst [75].

At the jet boundary two conditions are imposed: 1) the pressure of the outside flow and inside flow must be equal at the boundary and 2) the inside and outside flow must be tangent at the boundary. These conditions are satisfied by placing images of the horseshoe vortices along the wing. By calculating the induced velocities of these images on each control point, matrix G can be determined. To achieve an analytical solution, the horseshoe vortices are split up into an even and odd part as shown in Figure 7.2.

Furthermore, the induced velocities of the images depend on whether the images are inside or outside the jet and whether the point of the induced velocity is inside or outside the jet. As a result, there are four options possible for both the even and odd part. The four equations for the coefficients of G describing the image induced velocities for the even part are shown in Equation 7.3 till Equation 7.6 and the four equations for the coefficients of G describing the image induced velocities for the odd part are shown in Equation 7.7 till Equation 7.10. The first letter of the subscript of the coefficient G denotes whether the control point is inside the jet (j) or outside the jet (o), whilst the second letter denotes whether the image vortex is inside or outside the jet. The coefficients of the odd and even part are summed together to form the jet boundary downwash matrix G. The background on this method and derivation of these equations is out of the scope of this study and can be found in Rethorst [75].

$$G_{jj_{\text{even}}}(\eta) = \frac{1}{5}\frac{1-\mu^2}{1+\mu^2}\left[\frac{1}{(1/d)-\eta} - \frac{1}{(1/c)-\eta} + \frac{1}{(1/d)+\eta} - \frac{1}{(1/c)+\eta}\right] \tag{7.3}$$

$$G_{oj_{\text{even}}}(\eta) = -\frac{1}{5}\frac{(1-\mu)^2}{1+\mu^2}\left[\frac{1}{\eta-c} - \frac{1}{\eta-d} + \frac{1}{\eta+d} - \frac{1}{\eta+c}\right] \tag{7.4}$$

$$G_{jo_{even}}(\eta) = -\frac{1}{5}\frac{(1-\mu)^2}{1+\mu^2}\left[\frac{1}{d-\eta} - \frac{1}{c-\eta} + \frac{1}{d+\eta} - \frac{1}{c+\eta}\right] \tag{7.5}$$

$$G_{oo_{\text{even}}}(\eta) = -\frac{1}{5}\frac{1-\mu^2}{1+\mu^2}\left[\frac{1}{\eta-(1/c)} - \frac{1}{\eta-(1/d)} + \frac{1}{\eta+(1/d)} - \frac{1}{\eta+(1/c)}\right] \tag{7.6}$$

$$G_{jj_{odd}}(\xi,\eta) = \frac{8}{5\pi\eta}\sum_{p=0}^{\infty}(2p+1)^2\int_0^{\infty}\frac{KK'I(\eta\lambda)\sin\xi\lambda d\lambda}{[1/\{(1/\mu^2)-1\}]-\lambda IK'}\int_{c\lambda}^{d\lambda}\frac{I(\lambda\beta)}{\lambda\beta}d(\lambda\beta) \tag{7.7}$$

$$G_{oj_{odd}}(\xi,\eta) = \frac{8}{5\pi\eta}\sum_{p=0}^{\infty}(2p+1)^2\int_0^{\infty}\left[\frac{1}{\mu-\lambda\{(1/\mu)-\mu\}IK'}-1\right]\frac{K(\eta\lambda)\sin\xi\lambda d\lambda}{\lambda}\int_{c\lambda}^{d\lambda}\frac{I(\lambda\beta)}{\lambda\beta}d(\lambda\beta) \tag{7.8}$$

$$G_{jo_{odd}}(\xi,\eta) = \frac{8}{5\pi\eta}\sum_{p=0}^{\infty}(2p+1)^2\int_0^{\infty}\left[\frac{1}{\mu-\lambda\{(1/\mu)-\mu\}IK'}-1\right]\frac{I(\eta\lambda)\sin\xi\lambda d\lambda}{\lambda}\int_{c\lambda}^{d\lambda}\frac{K(\lambda\beta)}{\lambda\beta}d(\lambda\beta) \tag{7.9}$$

$$G_{oo_{odd}}(\xi,\eta) = \frac{8}{5\pi\eta}\sum_{p=0}^{\infty}(2p+1)^2\int_0^{\infty}\frac{II'K(\eta\lambda)\sin\xi\lambda d\lambda}{[1/\{(1/\mu^2)-1\}]-\lambda IK'}\int_{c\lambda}^{d\lambda}\frac{K(\lambda\beta)}{\lambda\beta}d(\lambda\beta) \tag{7.10}$$

7.2. Off-center jet modification

The method of Rethorst is applied on a jet in the center of the wing. However, most of the time the jet is not in the center but positioned along the semi-span. The method can be modified to allow for arbitrary spanwise positioning. For this the equally divided method of Nederlof [74] is used.

In the method of Rethorst only one half of the wing is used for the calculation of the G matrix coefficients as the horseshoe images are symmetric across the jet center. However, when the jet is off-center this is not the case anymore. As such, the G matrix has to be converted such that it is not only dependent on the circulation of one half of the wing but also on the circulation of the other half of the wing, increasing the matrix from size $m/2xm/2$ to mxm with m being the total amount of panels in spanwise direction. This is achieved by equally dividing the matrix coefficients over the symmetric horseshoe pairs at each side of the jet. For a wing with 5 strips with the jet in the center of the wing at the third strip, the original G matrix and equally divided matrix are shown in Equation 7.11 and Equation 7.12, respectively. It can be noticed that in case the jet is in the center of the wing, the spanwise circulation distribution is symmetric and therefore the two G matrices are equal.

$$G\Gamma = \begin{bmatrix} G_{11} & G_{12} & G_{13} \\ G_{21} & G_{22} & G_{23} \\ G_{31} & G_{32} & G_{33} \end{bmatrix}\begin{bmatrix} \Gamma_1 \\ \Gamma_2 \\ \Gamma_3 \end{bmatrix} \tag{7.11}$$

$$G\Gamma = \begin{bmatrix} G_{11}/2 & G_{12}/2 & G_{13} & G_{12}/2 & G_{11}/2 \\ G_{21}/2 & G_{22}/2 & G_{23} & G_{22}/2 & G_{21}/2 \\ G_{31}/2 & G_{32}/2 & G_{33} & G_{32}/3 & G_{31}/2 \\ G_{21}/2 & G_{22}/2 & G_{23} & G_{22}/2 & G_{21}/2 \\ G_{11}/2 & G_{12}/2 & G_{13} & G_{12}/2 & G_{11}/2 \end{bmatrix}\begin{bmatrix} \Gamma_1 \\ \Gamma_2 \\ \Gamma_3 \\ \Gamma_4 \\ \Gamma_5 \end{bmatrix} \tag{7.12}$$

To allow for the equally divided G matrix there has to be an equal amount of horseshoe vortices at both sides of the jet axis to allow for the symmetry pairs. In case of an off-center jet the horseshoe vortices are not symmetric. This is corrected by virtually extending the wing such that the jet is in the center of the wing plus virtual wing extension such as shown in Figure 7.3. The circulation of the horseshoe vortices located in this virtual wing extension are zero and can therefore be omitted. If Γ_5 is located within the virtual wing extension in the example of Equation 7.12, the final G matrix then becomes Equation 7.13.

$$G\Gamma = \begin{bmatrix} G_{11}/2 & G_{12}/2 & G_{13} & G_{12}/2 \\ G_{21}/2 & G_{22}/2 & G_{23} & G_{22}/2 \\ G_{31}/2 & G_{32}/2 & G_{33} & G_{32}/3 \\ G_{21}/2 & G_{22}/2 & G_{23} & G_{22}/2 \end{bmatrix}\begin{bmatrix} \Gamma_1 \\ \Gamma_2 \\ \Gamma_3 \\ \Gamma_4 \end{bmatrix} \tag{7.13}$$

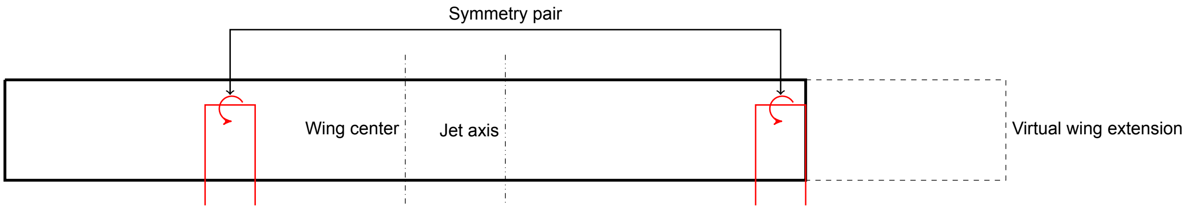

Figure 7.3: Virtual wing extension used for the jet correction if the jet axis is not at the wing center. The correction assumes symmetry in horseshoe vortices around the jet axis as denoted by the red lines.

7.3. Non-uniform velocity profile modification

The correction up until now assumes an uniform axial velocity profile. However, slipstreams of rotors have a radial variation in axial induced velocities. Prabhu [76] has shown that the induced velocities of the even part of the horseshoe images can be can be used via the superposition principle to account for radial variation in the axial induced velocities for an axisymmetric velocity profile. Willemsen [59] assumes in their method that this is also true for the odd part of the correction. In the present method this is also assumed.

The jet with radial variation in axial induced velocities can then be discretized by uniform jets with different radii and jet velocities as shown in Figure 7.4. As the boundary has to be aligned with the edges of the horseshoe vortex, the jet is discretized according to the spanwise discretization of the wing. The jet boundary downwash matrix can be calculated for each uniform jet and summed together in line with the superposition principle. For the velocity ratio the jet velocity of the neighboring annular jet is used as freestream velocity as shown in Equation 7.14.

$$\mu_i = \frac{V_\infty + u_{ss_{i-1}}}{V_\infty + u_{ss_i}} \tag{7.14}$$

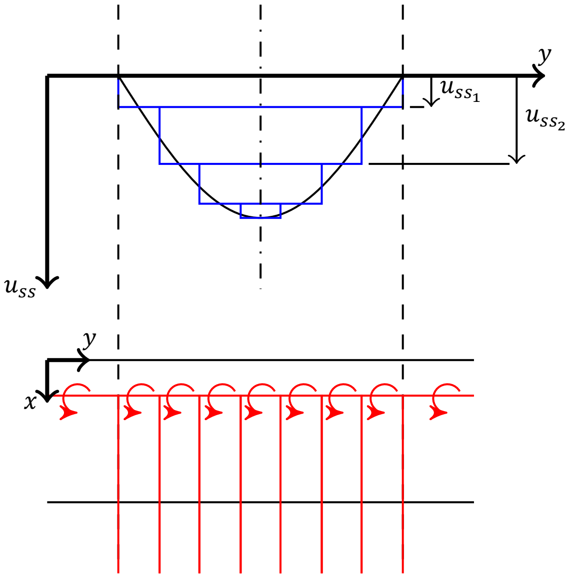

Figure 7.4: Top-view of the discrete representation of a jet with radially varying axial induced velocities in front of a wing discretized by horseshoe vortices as used in the jet correction. The discretization of the jet velocity profile coincides with the spanwise discretization of the wing.

7.4. Application to vortex ring VLM

The jet boundary downwash matrix G is calculated for a discrete lifting line method with only variation in horseshoe vortices along the span. However, the VLM utilizes a vortex ring method with spanwise as well as chordwise distributed vortex rings. As such, the slipstream induced velocities distributed calculated on each panel have to be reduced to one representative induced velocity per spanwise strip for use in the jet correction. Furthermore, the G matrix has to be converted from a mxm matrix to a NxN matrix, with m denoting the amount of spanwise strips and N denoting the total amount of vortex rings.

The jet velocity of a strip is determined by taking the weighted average of the slipstream induced velocities in every panel in that strip. The weights are calculated according to their fraction of

It is assumed that the jet boundary downwash matrix coefficient is constant for every control point in the same spanwise station, thus assuming that the downwash of the image vortices is constant along the chord. Furthermore, it is assumed that the images of the horseshoe vortices in a strip can be represented by one image horseshoe vortex with the same total circulation of that strip. The total circulation of a strip with the present VLM vortex ring method can be calculated according to Equation 7.15. As the rear bound vortex of a vortex ring opposes the front bound vortex of a vortex ring, the total circulation of the strip is represented by the trailing edge circulation which is equal to the circulation in the wake. As a result, the jet boundary downwash matrix coefficient for every control point is zero for every vortex ring except for the ones at the trailing edge of the surface.

$$\Gamma_{strip} = \Gamma_1 + (\Gamma_2 - \Gamma_1) + (\Gamma_3 - \Gamma_2) + \ldots + (\Gamma_n - \Gamma_{n-1}) = \Gamma_n \tag{7.15}$$

The coefficients of the converted G matrix with respect to the coefficients of the original G matrix are then as shown in Equation 7.16.

$$G_{VLM}[i,j] = \begin{cases} 0, & \text{if } \Gamma_j \text{ is not at TE} \\ G[i_{strip_{panel_i}}, i_{strip_{panel_j}}], & \text{if } \Gamma_j \text{ is at TE} \end{cases} \tag{7.16}$$

Furthermore, the method requires the jet axis to coincide with the center of a panel, the jet boundary to coincide with the edge of panel and the mesh to be symmetric. Therefore, the mesh of the wing submerged in the slipstream is generated beforehand to be symmetric within the jet and aligned with the jet boundary and center requirements. This also allows mesh refinement for the slipstream submerged section without refining the mesh outside of the slipstream. As the spanwise panel distribution is sinusoidal outside of the mesh of the slipstream immersed wing section the panel symmetry is not conserved outside of the slipstream. This is solved by linearly interpolating the G coefficients for the panel locations at the other side of the jet axis.

7.5. Non-planar wing modification

The Rethorst method is derived with the assumption that the wing is planar such that all the images of the horseshoe vortices which enforce the slipstream boundary condition are located in the $z = 0$ plane, allowing for an analytical solution to be found. However, the flap can be largely off-plane from the main element due to its vertical off-set or deflection. Therefore, it is investigated whether the planar assumption remains valid in case a trailing surface is vertically off-set from the leading surface. For this purpose, a sensivity analysis is performed on the finite slipstream correction as function of the vertical off-set of the flap.

7.5.1. Sensitivity analysis to flap position

For the sensitivity analysis, a simplified VLM geometry with a flat plate for the main and flap element immersed in a sinusoidal slipstream is set up. The slipstream velocity profile and wing geometry visually shown in Figure 7.5. The VLM is then used to investigate the sensitivity of the lift and circulation distribution to the vertical position of the trailing flap.

The spanwise lift and circulation distribution for different vertical flap positions is shown in Figure 7.6. First, analysing the lift distribution of the wing and separate elements. It can be seen that the total lift distribution of the wing with the flap at $z = 0$ is not showing erroneous spikes and is similar to the isolated main element analysis solution. As the flap is positioned lower than the main element, non-physical spikes in lift are observed at the center of the slipstream where the induced velocities are zero. The discrepancy is not visible in the main element lift distribution but is prominently visible in the lift distribution on the flap. For the flap at $z/c_{main} = 0$, the lift is greatly reduced in the slipstream due to the finite correction but its shape follows the distribution of the uncorrected solution. For the flap positions further away from the xy plane, the lift is shown to reduce values lower than lift outside of the

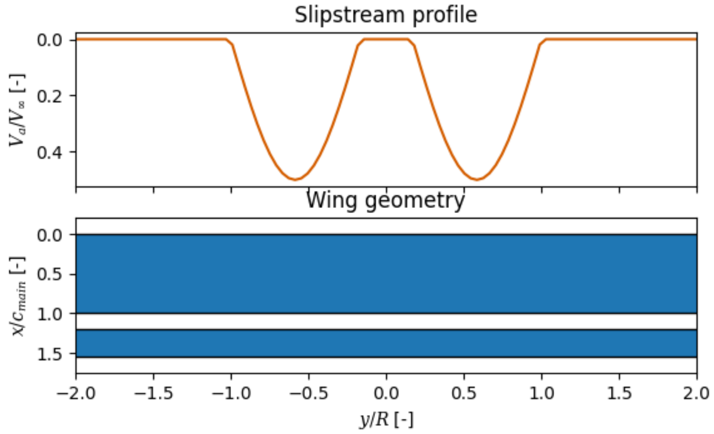

Figure 7.5: Slipstream profile and wing geometry used in the analysis of the sensitivity of the finite slipstream correction to vertical flap position.

slipstream while the lift at the center of the slipstream is excessively increased. Comparing the circulation distributions on the flap reveals that the excessive increase in lift at the center of the slipstream is caused by an excessive increase in circulation at this location by the finite slipstream correction while the flap with zero vertical off-set reveals a reduction in circulation in this region. While the non-physical results on the flap have limited effect on the total lift distribution in this geometry, its effect on the total lift will only increase as the flap contributes more to the lift of the wing such as for a bigger flap or a flap deflected.

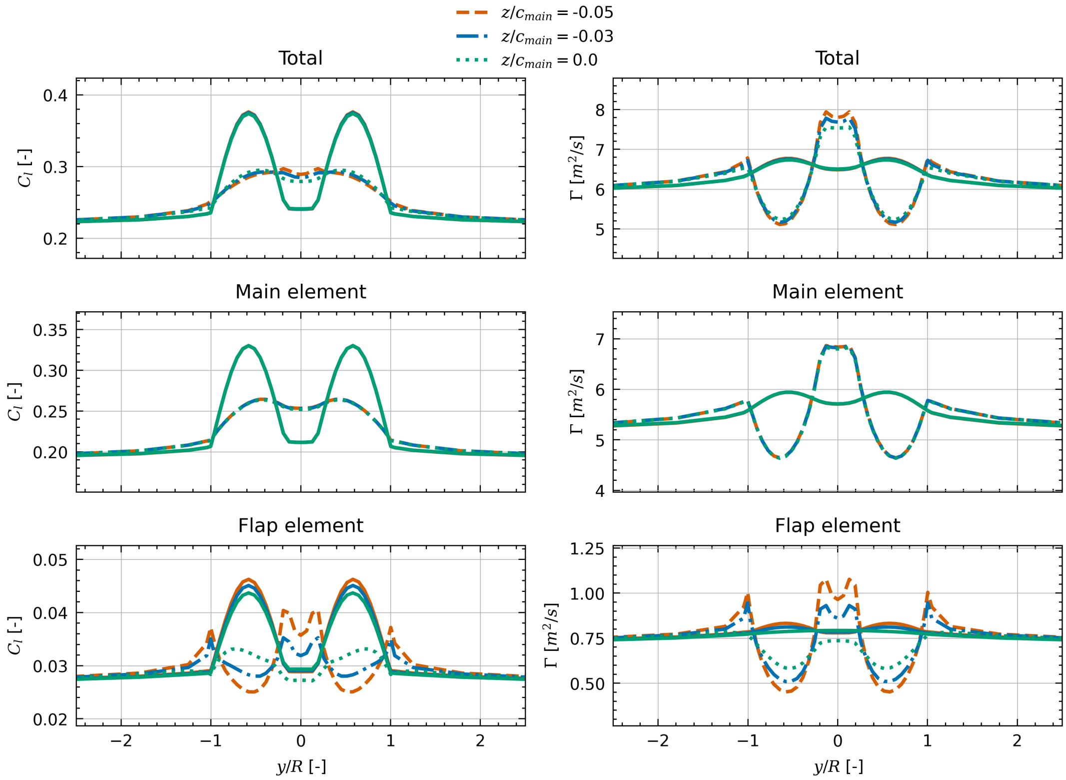

Figure 7.6: The spanwise lift distribution (left) and circulation distribution (right) for the total wing, main element, and flap element for different vertical flap positions. The solid lines indicate the distributions without finite slipstream correction for the respective vertical flap positions.

The cause of the discrepancy is attributed to the assumption of the method of Rethorst [75] which states that the wing is planar. This assumption holds true if the flap is undeflected and is at the same vertical position as the main element. However, if the flap is deflected and/or vertically displaced the lifting line method and the VLM used in the present method become inconsistent with each other. The lifting line method assumes that the vorticity of the flap and its wake is in the same plane as that of the main element and its wake while the VLM has the vorticity of the flap and its wake off-set by a certain distance from the main element. As a result, the induced velocities of the images of the main element on the control point of the flap that are calculated by the jet correction method are overestimated as the control point in the lifting line method is closer to the bound and trailing vortices of the main element than in the VLM. As the control point is closer to the vortex lines, the induced velocities are overestimated according to the Biot-Savart law. This effect is schematically shown in Figure 7.7.

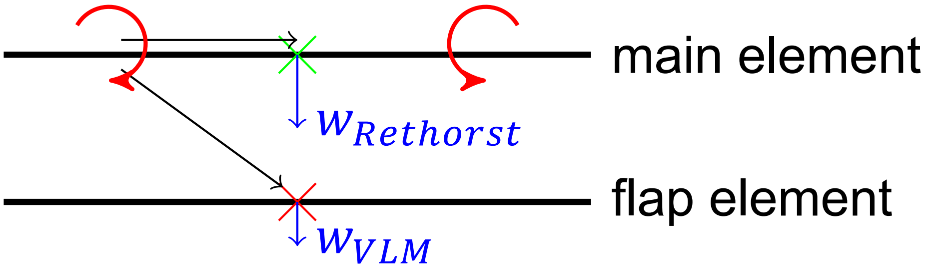

Figure 7.7: Difference in induced velocity due to a trailing vortex of the main element between the control point used in the method of Rethorst [75] (green cross) and used in the present VLM (red cross).

The difference in distance between a trailing vortex line and a control point at different heights can be relatively large if the mesh size is small such that the y distance is much smaller than the z distance. The overestimation of the image induced velocities of the main element on the flap results causes larger downwash at the slipstream velocity maxima positions on the flap and larger upwash at the slipstream velocity minimum positions, resulting in the circulation and lift seen in Figure 7.6. The discrepancy in the circulation is greatest at the center of the slipstream compared to the slipstream boundary as the spanwise circulation gradient is greater here as seen in the circulation distribution on the main element. As a result, the trailing vortices shed at these locations are here the greatest, which amplifies the error.

7.5.2. Non-planar finite slipstream correction

The Rethorst method is adapted to allow for the specification of a z-coordinate (= ζ non-dimensionalized with jet radius) for the control points, or ζ . For the even system this results in a simple adaptation of the two-dimensional Biot-Savart law to include a z component, resulting in the new downwash coefficients for the even system as shown in Equation 7.17 till Equation 7.20.

$$G_{jj_{\text{even}}}(\eta,\zeta) = \frac{1}{5}\frac{1-\mu^2}{1+\mu^2}\left[\frac{(1/d)-\eta}{((1/d)-\eta)^2+\zeta^2} - \frac{(1/c)-\eta}{((1/c)-\eta)+\zeta^2} + \frac{(1/d)+\eta}{((1/d)+\eta)^2+\zeta^2} - \frac{1/c)+\eta}{((1/c)+\eta)^2+\zeta^2}\right] \tag{7.17}$$

$$G_{oj_{\text{even}}}(\eta,\zeta) = -\frac{1}{5}\frac{(1-\mu)^2}{1+\mu^2}\left[\frac{\eta-c}{(\eta-c)^2+\zeta^2} - \frac{\eta-d}{(\eta-d)^2+\zeta^2} + \frac{\eta+d}{(\eta+d)^2+\zeta^2} - \frac{\eta+c}{(\eta+c)^2+\zeta^2}\right] \tag{7.18}$$

$$G_{jo_{even}}(\eta,\zeta) = -\frac{1}{5}\frac{(1-\mu)^2}{1+\mu^2}\left[\frac{d-\eta}{(d-\eta)^2+\zeta^2} - \frac{c-\eta}{(c-\eta)^2+\zeta^2} + \frac{d+\eta}{(d+\eta)^2+\zeta^2} - \frac{c+\eta}{(c+\eta)^2+\zeta^2}\right] \tag{7.19}$$

$$G_{oo_{\text{even}}}(\eta,\zeta) = -\frac{1}{5}\frac{1-\mu^2}{1+\mu^2}\left[\frac{\eta-(1/c)}{(\eta-(1/c))^2+\zeta^2} - \frac{\eta-(1/d)}{(\eta-(1/d))^2+\zeta^2} + \frac{\eta+(1/d)}{(\eta+(1/d))^2+\zeta^2} - \frac{\eta+(1/c)}{(\eta+(1/c))^2+\zeta^2}\right] \tag{7.20}$$

The adaptation of the odd system is more complicated as the presence of the bound vortex necessitated the use of Bessel functions for an analytical expression of the potential fields. For the present adaptation, the downwash is derived by taking the derivative of the potential field expressions with respect to z without assuming that $z == 0$. The result is the multiplication of the existing equation with the term of $1/cos(\theta)$ resulting from the change of coordinate system from Cartesian to cylindrical, and by reintroducing the $cos((2p+1)\theta)$ term in the series in front of the integral term to allow for $\theta \neq 0 or \pi$. Here, θ indicates the azimuth angle of the control point with respect to the jet axis. The resulting jet boundary downwash coefficients for the odd system are then as shown in Equation 7.21 till Equation 7.24.

$$G_{jj_{odd}}(\xi,\eta,\zeta) = \frac{8}{5\pi\eta cos(\theta)} \sum_{p=0}^{\infty}(2p+1)^2 cos((2p+1)\theta) \int_0^{\infty} \frac{KK'I(\eta\lambda)\sin\xi\lambda d\lambda}{[1/\{(1/\mu^2)-1\}]-\lambda IK'} \int_{c\lambda}^{d\lambda} \frac{I(\lambda\beta)}{\lambda\beta} d(\lambda\beta) \tag{7.21}$$

$$G_{oj_{odd}}(\xi,\eta,\zeta) = \frac{8}{5\pi\eta cos(\theta)} \sum_{p=0}^{\infty}(2p+1)^2 cos((2p+1)\theta) \int_0^{\infty} \left[\frac{1}{\mu-\lambda\{(1/\mu)-\mu\}IK'} - 1\right] \frac{K(\eta\lambda)\sin\xi\lambda d\lambda}{\lambda} \int_{c\lambda}^{d\lambda} \frac{I(\lambda\beta)}{\lambda\beta} d(\lambda\beta) \tag{7.22}$$

$$G_{jo_{odd}}(\xi,\eta,\zeta) = \frac{8}{5\pi\eta cos(\theta)} \sum_{p=0}^{\infty}(2p+1)^2 cos((2p+1)\theta) \int_0^{\infty} \left[\frac{1}{\mu-\lambda\{(1/\mu)-\mu\}IK'} - 1\right] \frac{I(\eta\lambda)\sin\xi\lambda d\lambda}{\lambda} \int_{c\lambda}^{d\lambda} \frac{K(\lambda\beta)}{\lambda\beta} d(\lambda\beta) \tag{7.23}$$

$$G_{oo_{odd}}(\xi,\eta,\zeta) = \frac{8}{5\pi\eta cos(\theta)} \sum_{p=0}^{\infty}(2p+1)^2 cos((2p+1)\theta) \int_0^{\infty} \frac{II'K(\eta\lambda)\sin\xi\lambda d\lambda}{[1/\{(1/\mu^2)-1\}]-\lambda IK'} \int_{c\lambda}^{d\lambda} \frac{K(\lambda\beta)}{\lambda\beta} d(\lambda\beta) \tag{7.24}$$

7.5.3. Evaluation of the non-planar modification

The adapted equations for the slipstream boundary downwash coefficients are implemented in the code using the z-coordinate of the three-quarter chord points on each surface for the control points. Applying the adapted finite slipstream correction to the same analysis problem of subsection 7.5.1 yields the results for the lift and circulation distributions as shown in Figure 7.8. It can be seen that the circulation and lift distributions on the flap matches much closer to the solution for $z = 0$ and does not display excessive circulation and lift near the jet center as observed for the original method. With the adapted method, the lift near the rotor slipstream is reduced slightly more than necessary but still closer than the original correction method. However, the minor discrepancies on the flap are negligible when comparing the lift and circulation distribution of the total wing.

The minor discrepancies still present are attributed to the still present differences between the lifting line method and the VLM. The downwash of the lifting line at the three-quarter chord point is different than a chordwise downwash distribution evaluated in the VLM. This discrepancy is expected to decrease as the distance between the main and flap element are increased. An increase in distance is expected to make the modelling of a lifting surface with a vortex line at the quarter-chord more valid for the computation of the induced velocities between the surfaces.

Furthermore, the discrepancies are expected to increase at higher angles of attack if a freestream aligned wake is used. The wake of the surfaces will as a result considerably be deflected from the plane of the lifting surfaces in the VLM while the method of Rethorst [75] assumes that the wake is always in plane with the surface. For this reason, the wake is modeled to be aligned with the body instead of with the freestream for the analyses of geometries with a flap.

Due to the large sensitivity of the lift to the finite slipstream correction and the found issues in the original method of Rethorst [75], it is recommended for future research to investigate image-based finite slipstream correction methods directly derived from the vortex lattice method instead of an equivalent lifting line method. This would avoid the inconsistencies between the two modelling methods allowing for an accurate finite slipstream correction for highly non-planar lifting geometries such as found in wings with deployed flaps.

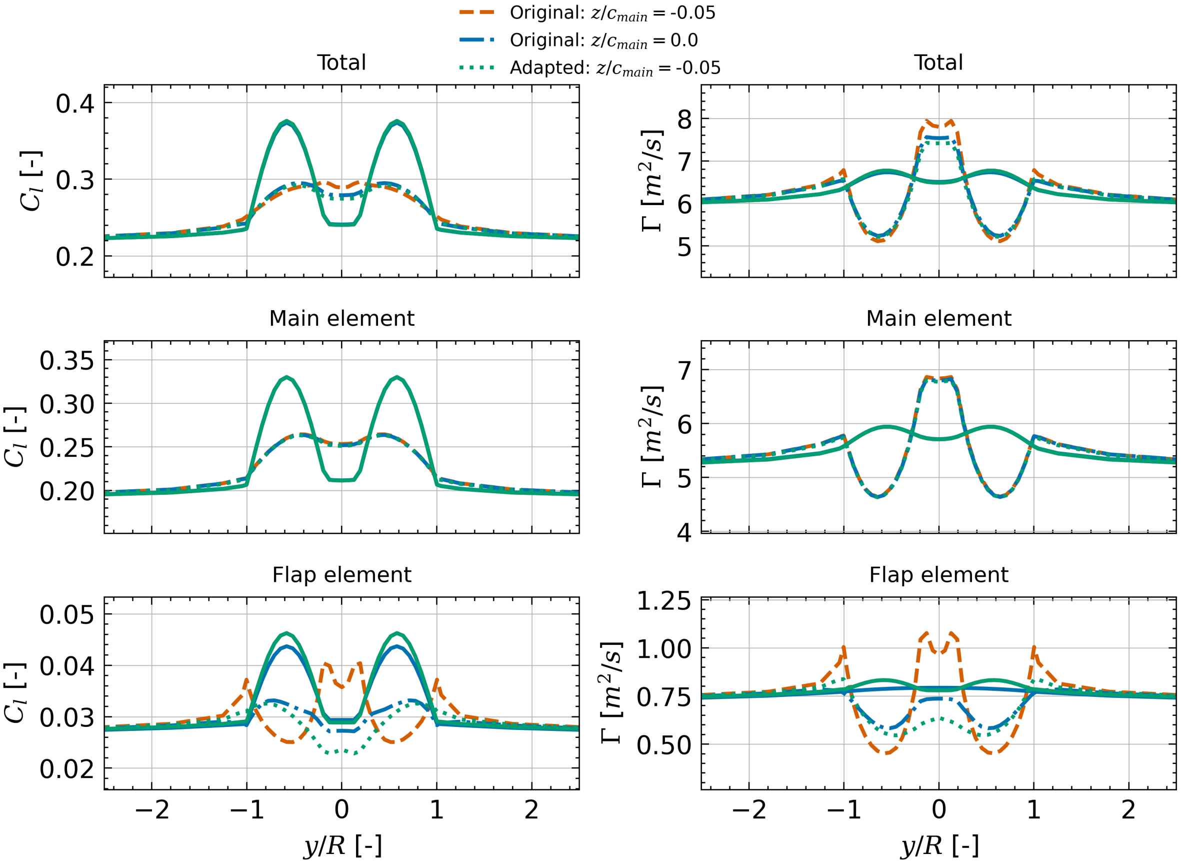

Figure 7.8: The spanwise lift distribution (left) and circulation distribution (right) for the total wing, main element, and flap element for the original finite slipstream correction method and the adapted finite slipstream correction method for non-planar surfaces. The solid lines indicate the distributions without finite slipstream correction for the respective solutions.

7.6. Finite slipstream correction verification

To verify the implementation of the finite slipstream correction into the present vortex ring VLM the spanwise lift distribution is compared with the results of Willemsen [59] and Nederlof [74] for a straight wing with an aspect ratio of 10 and a NACA 0012 airfoil submerged in one uniform jet with a radius equal to the chord at 50% semi-span.

Willemsen has applied a lifting line method with the present Rethorst method and equally divided correction whilst Nederlof performed an inviscid CFD analysis with a laminar model as turbulence model and very small value for viscosity. As the CFD analysis accounts for airfoil thickness and the lifting line method and VLM do not, a 6% magnification in C_l is used on the lifting line method and VLM to account for thickness. This 6% is provided in Nederlof [74] and is derived from a comparison between a VLM and CFD analysis without the presence of a jet.

The spanwise lift and circulation distribution of the different methods is shown in Figure 7.9 and Figure 7.10, respectively. An excellent match in the lift coefficient distribution is found between the present VLM and the LL and CFD results. It can be seen that the lift coefficient is correctly reduced within the jet with as a result a smooth change in lift along the jet boundary. The sectional circulation is also seen to match well with the lifting line results. Small discrepancies are found near the jet boundary due to discretization errors of the lifting line method which used a coarser grid than the VLM.

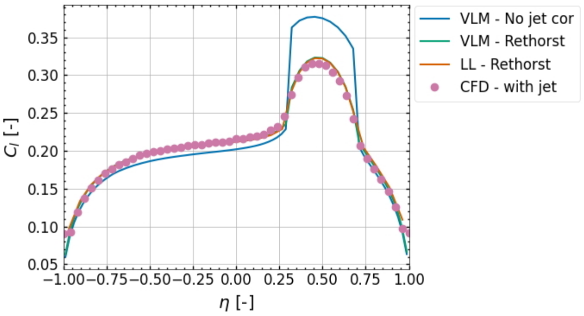

Figure 7.9: Lift coefficient distribution for the VLM without and with the Rethorst jet correction together with the results of the lifting line method with Rethorst correction of Willemsen [59] and the CFD results of Nederlof [74].

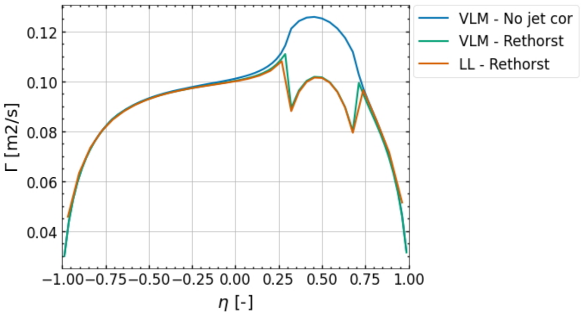

Figure 7.10: Spanwise circulation distribution for the VLM without and with the Rethorst jet correction together with the results of the lifting line method with Rethorst correction of Willemsen [59].

8

Viscous wing-flap module: MSES

A viscous flow solver is required to correct the inviscid results for viscous effects. The viscous flow solver has to be able to solve for multi-element airfoils for the purpose of this research. The model has to account for the circulation effects, fresh boundary layer effect, off-the-surface pressure recovery and dumping effect whilst remaining computationally fast enough to allow for rapid geometry iterations. The two-dimensional flow solver MSES is used for this purpose which is a collection of programs to analyze single- and multi-element airfoils. Limiting the viscous analysis to a two-dimensional analysis greatly reduces the computational time whilst still capturing the important streamwise viscous effects found on lifting surfaces. More details on the methods of MSES can be found in Drela [77]. MSES couples a two-dimensional inviscid Euler method with a two-equation integral boundary layer formulation for viscous effects. These methods are coupled through the boundary layer displacement thickness in a Newton-iteration scheme. Furthermore, the boundary layer formulation is extended to multi-layer velocity profiles to account for asymmetric wakes and confluent shear layers present in multi-element airfoil flows.

The inviscid formulation of MSES is first described in section 8.1 after which the viscous formulation is then presented in section 8.2. The inviscid-viscous coupling scheme uses the chordwise lift distribution of MSES. The method to obtain this force distribution from the output of MSES is described in section 8.3. Lastly, MSES is validated for single slotted wing-flap geometries in section 8.4.

8.1. Inviscid formulation

A streamline grid is used to discretize the steady Euler equations onto. This streamline grid is solved simultaneously with the flow field in the full Newton method. The advantage of using a streamline grid is that the mass flux and stagnation enthalpy are always conserved along a streamtube. This reduces the energy and continuity equations to two algebraic equations as shown in Equation 8.1 and Equation 8.2. The pressure, p, and the velocity, q, can be eliminated by the grid node positions as variables in the Newton method as the streamtube area is a function of the node positions. The streamline grid and its flow variables as well as the grid nodes expressing the Newton variables are shown in Figure 8.1.

$$\frac{\gamma}{\gamma-1}\frac{p}{\rho}+\frac{q^2}{2}=h_0=constant \tag{8.1}$$

$$\rho q A=\dot{m}=constant \tag{8.2}$$

Away from shockwaves it is preferred to use isentropic condition as specified in Equation 8.3 instead of the conservation of energy as shown in Equation 8.1 as it allows for coarser grids to be used. These shockwaves can appear even at lower freestream Mach numbers in multi-element airfoils due to the associated higher supervelocities reached along the surface.

$$\rho\left[1-\frac{q^2}{(\gamma-1)h_0}\right]^{\frac{-1}{\gamma-1}}=\rho_0=constant \tag{8.3}$$

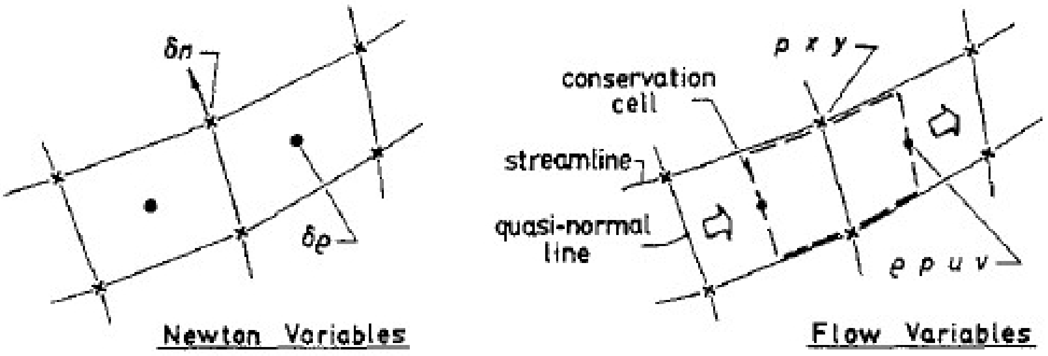

Figure 8.1: Streamline grid and its flow variables and Newton variables used in the discretization of the Euler equations. [77]

The far-field boundary conditions consisting of the velocity and pressure are derived from a far-field circulation term, source strength and two doublet components. The boundary condition imposed on the airfoil surface is such that the streamline is displaced by the local displacement thickness of the boundary layer. The gap in the wake is set to be the sum of displacement thicknesses of both upper and lower surface. The streamlines are imposed to be parallel with the freestream velocity at the inlet. The stagnation point is constrained by enforcing equal pressure on each side of this point.

8.2. Viscous formulation

The viscous effects are accounted for using a two-equation integral boundary layer equations.These equations are able to resolve thin separated regions, allowing for extremer flow cases. The integral boundary-layer equations are shown in Equation 8.4 and Equation 8.5 as derived in Drela and Giles [78].

$$\frac{d\theta}{d\xi} + (2 + H - M_e^2)\frac{\theta}{u_e}\frac{du_e}{d\xi} = \frac{C_f}{2} \tag{8.4}$$

$$\theta\frac{dH^*}{d\xi} + [2H^{**} + H^*(1 - H)]\frac{\theta}{u_e}\frac{du_e}{d\xi} = 2C_{Ds} - H^*\frac{C_f}{2} \tag{8.5}$$

The closure of the integral boundary layer equations is done by assuming the functional dependencies shown in Equation 8.6, Equation 8.7, Equation 8.8 and Equation 8.9. These correlations are explained more thoroughly by Drela and Giles [78] for both the laminar and turbulent case. The analysis of free wakes is valid using the presented boundary layer equations and the turbulent closure relations by stacking the upper and lower surface boundary layers and setting the skin-friction coefficient to zero. The boundary layer transition is predicted using the e^n method as detailed by Ingen [79].

$$H^* = H^*(H_k, M_e, Re_\theta) \tag{8.6}$$

$$H^{**} = H^{**}(H_k, M_e) \tag{8.7}$$

$$C_f = C_f(H_k, M_e, Re_\theta) \tag{8.8}$$

$$C_{Ds} = C_D(H_k, M_e, Re_\theta \tag{8.9}$$

MSES uses extended integral boundary layer equations and closure relations for the use of multi-layer velocity profiles in the wake. This allows the modelling of the confluence of adjacent shear layers and wake asymmetries present in multi-element airfoil flows as shown in Figure 8.2. Each wake is formulated as two half-sine wake profiles with a velocity discontinuity at the wake centerline. MSES does not model the confluence effects of the wake and boundary layer, leading to an over prediction of maximum lift according to Drela [77].

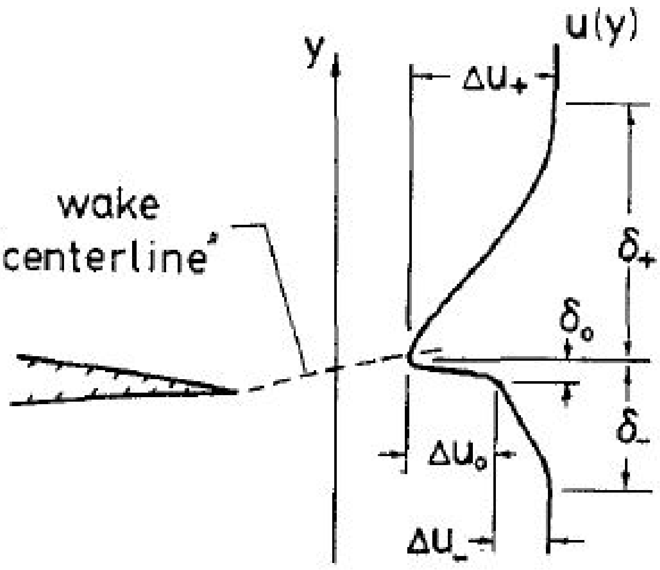

Figure 8.2: Multi-layer wake profile with a steep shear layer downstream of trailing edge as is modeled in MSES. [77]

8.3. Surface force distribution

The inviscid-viscous coupling method described in this research requires the viscous model to output the chordwise lift coefficient distribution. This distribution is derived from the pressure and skin friction coefficient distribution given as output of MSES.

The chordwise lift coefficient distribution can be calculated by integrating the pressure and skin friction coefficient along the surface in the normal and tangential direction. The chordwise normal force coefficient on an infinitesimal chord segment is given by Equation 8.10 and calculated using the difference in the pressure coefficient and the net skin friction force normal to the chord. The tangential force coefficient is similarly derived to be Equation 8.11 but by taking the forces in tangential direction. In this direction an additional term appears due to the freestream pressure which can be related to the freestream Mach number following the isentropic condition in the freestream.

$$dC_N = dC_{N_p} + dC_{N_f} = (C_{p_l} - C_{p_u}) + (C_{f_u}\frac{dy_u}{dx} + C_{f_l}\frac{dy_l}{dx}) \tag{8.10}$$

$$dC_T = dC_{T_p} + dC_{T_f} = \left(C_{p_u}\frac{dy_u}{dx} - C_{p_l}\frac{dy_l}{dx} + \frac{2}{\gamma M_\infty^2}(\frac{dy_u}{dx} - \frac{dy_l}{dx})\right) + (C_{f_u} + C_{f_l}) \tag{8.11}$$

The lift coefficient on an infinitesimal chord segment can then be described by Equation 8.12 using the local geometric angle of attack.

$$dC_l = dC_N cos(\alpha + \delta) - dC_T sin(\alpha + \delta) \tag{8.12}$$

8.4. MSES validation

MSES is validated by comparing the predicted the pressure distribution of an airfoil with a single slotted flap with experimental results from literature. For this purpose the experimental data set of Van den Berg [80] is used. The measurements are performed in a low-speed wind tunnel test with a two-dimensional wing flap configuration with a 32% chord trailing edge flap with a deflection of 20 degrees. This airfoil, NLR7301, is shown in Figure 8.3. The measurements are performed at an angle of attack of six degrees, Reynolds number of $2.51e6$ and Mach number of 0.185. The analysis of the NLR7301 converges successfully in MSES. However, it should be noted that the success of convergence on this airfoil is not indicative of the expected overall success on different airfoils. Different airfoil geometries were also analysed with MSES throughout the present research and it was noticed that MSES tends to have more difficulty converging when a cove is present, a sharp leading edge is present, and when the gap is smaller. In these cases, separation at the trailing end of the main element can occur and the flap element can be submerged in the separated wake from the lower surface of the main element. In these cases MSES is not able to converge successfully. Furthermore, convergence at higher angles of attack near stall was often not achieved. For this reason, stall could most of the time not be predicted, and if it was, the validity would be questionable.

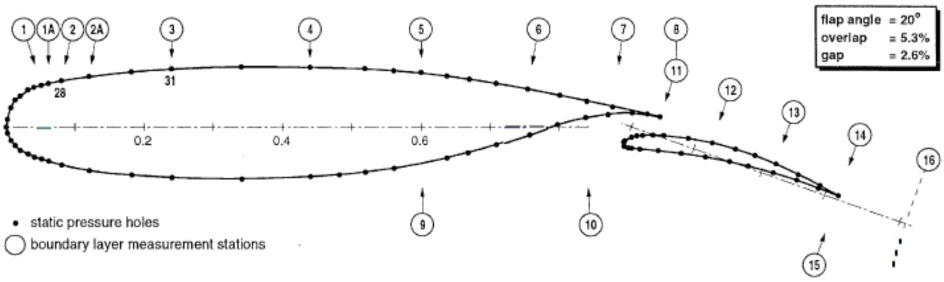

Figure 8.3: NLR 7301 airfoil as used in the MSES validation. [80]

The pressure distribution on the main and flap element according to both the MSES prediction as well as the experimental results from literature for the NLR7301 airfoil are shown in Figure 8.4. An excellent agreement can be seen between MSES and the experimental measurements on both elements except for a slight overprediction in the suction pressure peak. The total lift coefficient is therefore also slightly overpredicted with a value of 2.475 compared to the measured lift coefficient of 2.416 in the experiment.

Furthermore, the measured drag is compared with the drag as predicted by MSES. MSES predicts a profile drag coefficient of 0.0222 whilst the mean measured profile drag coefficient measured in the experiments is 0.0229 which is an error of 3%. However, the profile drag of the experiments is a mean of the profile drag measurements at different spanwise stations. Variation of 5 to 10% of the mean value were measured. An error of 3.0% is therefore within the range of error induced by the three-dimensional effects in the experiment.

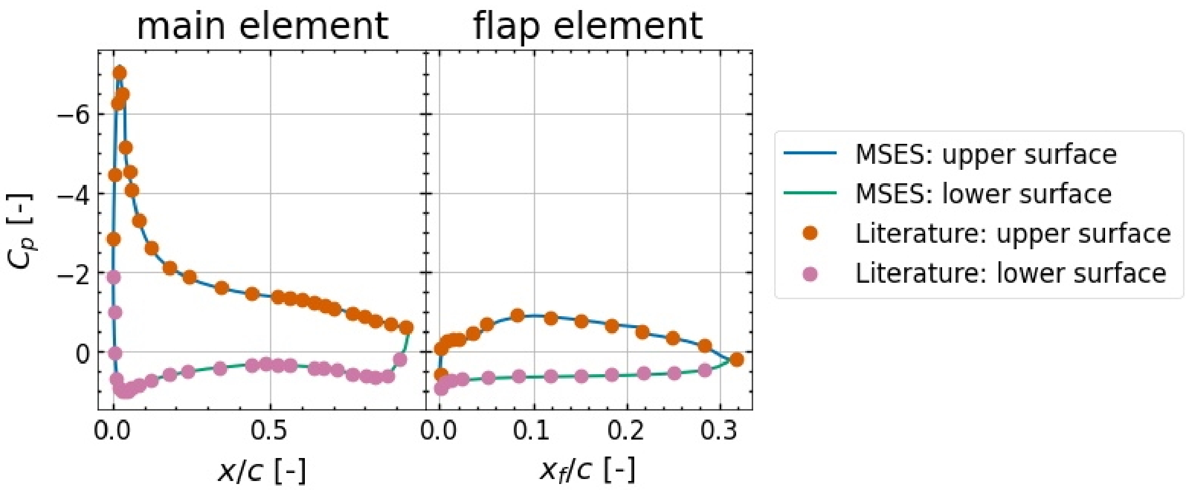

Figure 8.4: Pressure distribution of a NLR 7301 airfoil at an angle of attack of 6 degrees as predicted by MSES and as measured in the experimental data set from literature [80]. Analysis performed at a Reynolds number of $2.51e6$ and Mach number of 0.185.

9

Inviscid-viscous coupling: decambering approach

The three-dimensional inviscid model (VLM) is coupled with the two-dimensional viscous wing-flap model (MSES) to correct the inviscid model for the viscous, thickness and compressibility effects. The method for the coupling between the VLM and MSES is denoted as inviscid-viscous coupling. In the present research a decambering approach by rotating the panel normal vectors is adopted for the inviscid-viscous coupling. Furthermore, the coupling adds the profile drag to the drag build-up of the wing.

The top-level explanation of the inviscid-viscous coupling method is explained in section 9.1. Thereafter, is the effective angle of attack determination and the analysis on the effects of this assumption are presented in section 9.2. The method describing the camber adaptation to correct for the viscous effects as function of the effective angle of attack is described in section 9.3. The coupling method is verified in section 9.4. Lastly, a mesh convergence study is presented section 9.5.

9.1. Inviscid-viscous coupling process

To couple the three-dimensional VLM method to the two-dimensional MSES program strip theory is applied by defining a set of spanwise strips. The chordwise sets of panels at different spanwise locations in the VLM are used as strips for this purpose. In this theory the aerodynamic characteristics of a strip are modeled as if the strip has an infinite span. It is assumed that there are no spanwise influences on the viscous effects the between strips. The only spanwise influences included are the induced velocities from neighboring strips inferred from the VLM.

The inviscid-viscous coupling is achieved by two main steps: 1) effective angle of attack determination of each strip and 2) adaptation of the normal vector orientation of the panels in the VLM.

The correction for the viscous, thickness, and compressibility effects using the results of MSES is not straight forward. The predicted lift distribution in the strips of the VLM is not readily comparable with the predicted lift distribution in MSES due to the difference in external flow field. The VLM should only be corrected for the viscous, thickness and compressibility effects and not for the difference in the external flow field between the VLM strip and MSES. Ideally, this is achieved by evaluating MSES with the same external flow field as observed at the VLM strip, including the downwash distribution and slipstream induced velocity distribution. However, in the standard implementation of MSES this is not possible. Instead, the external flow field is defined as an uniform flow field at a specific angle of attack with respect to the airfoil. As a result, the discrepancy in the force distribution on the airfoil between the strip of the VLM and the MSES model is not only due to the viscous effects but also partly due to the difference in external flow field. The different contributions to the discrepancy in the chordwise lift distribution between the VLM strip and MSES can then be defined as Equation 9.1, with a term for the combined viscous, thickness and compressibility effects, a term for the self-induced velocities of the wing (i.e. downwash), and the slipstream induced velocities.

$$(dC_l)_{VLMstrip} - (dC_l)_{MSES} = \Delta dC_l = (\Delta dC_l)_{vtc} + (\Delta dC_l)_{ind} + (\Delta dC_l)_{ss} \tag{9.1}$$

Correcting the chordwise lift distribution of the VLM strip directly with the results of MSES will therefore also undesirably correct for difference between the external and internal induced velocities in the VLM and the uniform inflow in MSES. To more accurately compare the forces between the VLM and MSES, the MSES model is compared instead with the forces of a two-dimensional panel method with the same effective angle of attack. The two-dimensional panel method is developed as a two-dimensional version of the vortex ring VLM with no panels in spanwise direction and infinite bound vortices. This two-dimensional panel method uses the same panels on the camber line as used in the VLM such that the mesh of the VLM and the 2D panel method are equivalent. Using the 2D panel method, the chordwise lift distribution of the strips is corrected such that the chordwise lift distribution of MSES and the 2D panel method at the strip effective angle of attack are equal. By reducing the difference between the lift of the two-dimensional panel method and MSES, only the viscous, thickness, and compressibility effects are corrected for. It is assumed that the viscous correction on the 2D panel method is the same as on a strip in the VLM with the same effective angle of attack. This assumption is denoted in equation form in Equation 9.2. The normal vector adaptation on the 2D panel method can then directly be applied on a strip in the VLM with the same effective angle of attack.

$$(\Delta dC_l)_{vtc} \approx (dC_l)_{2Dpanel} - (dC_l)_{MSES} \tag{9.2}$$

To demonstrate the effect of downwash profile compared to an uniform inflow, an example of the difference in chordwise lift distributions of a VLM strip, MSES and the two-dimensional panel method for a section without slipstream induced velocities is shown in Figure 9.1. The viscous, thickness, and compressibility effects are then shown by the difference in MSES and the 2D panel method at the same effective angle of attack. The self-induced downwash effect is shown by the difference in the 2D panel solver and the VLM strip.

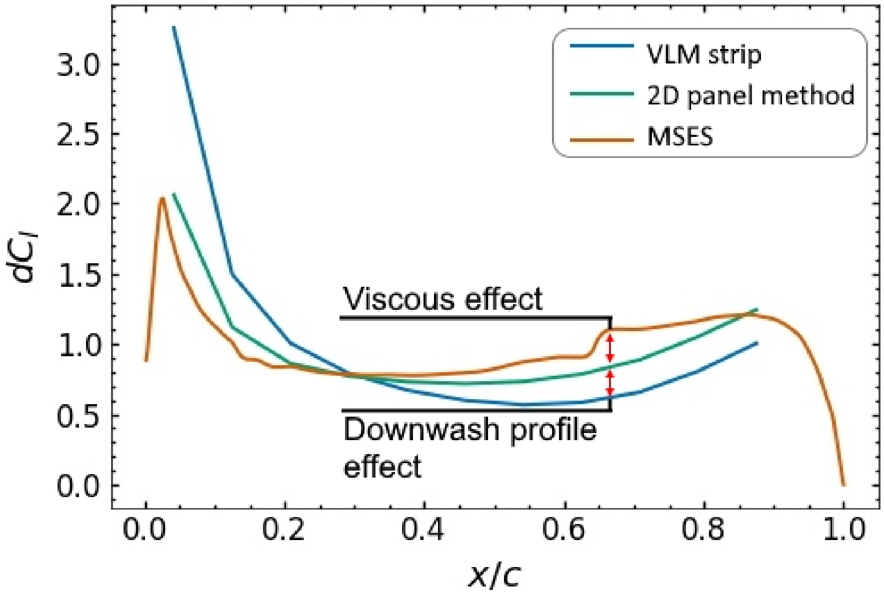

Figure 9.1: Chordwise lift distribution at a strip calculated with 1) VLM (VLM strip), 2) 2D thin-airfoil panel method at effective angle of attack (2D panel method) and 3) MSES at effective angle of attack (MSES). Viscous effect and downwash profile effect on the lift distribution are shown by the red arrows.

The viscous correction can then be applied to each strip in the VLM using the effective angles of attack. The correction changes the effective angle of attack of each strip, requiring another iteration of corrections. This process is repeated until the orientation of the normal vectors are converged. The profile drag calculated by MSES for each strip at the converged effective angle of attack distribution is then added to the drag build-up of the wing. The flowchart describing the inviscid-viscous coupling process is shown in Figure 9.2.

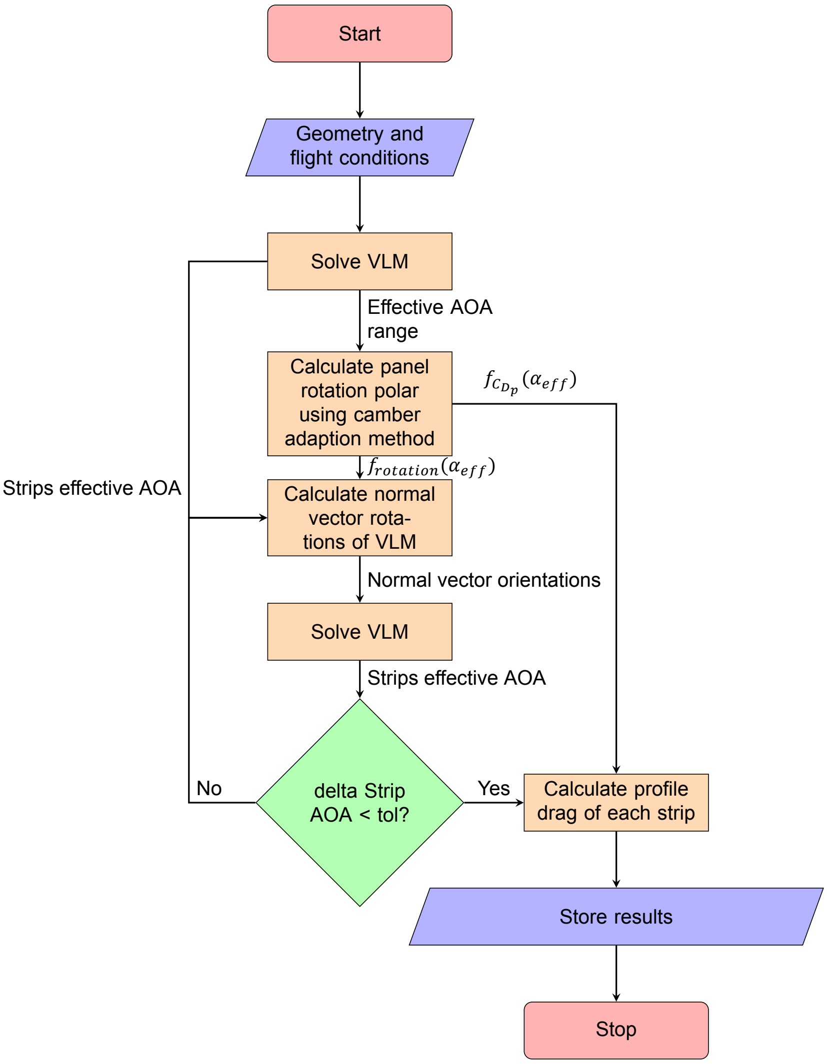

Figure 9.2: Flowchart of inviscid-viscous coupling method.

9.2. Effective angle of attack

MSES assumes a uniform inflow at a certain angle of attack. Therefore, an effective angle of attack has to be derived from each strip of the VLM to perform a two-dimensional viscous analysis of that strip.

In other viscous correction methods [81, 51, 82] the effective angle of attack is often calculated from the two-dimensional lift curve by finding the angle of attack that yields the same lift coefficient as that of the strip in the VLM analysis. However, the determination of the effective angle of attack is not trivial in case of a section within a slipstream. The two-dimensional lift curve of an airfoil in an uniform flow is not representative of a section within a slipstream. First of all, the slipstream velocity field has much larger spatial variations than the velocity field self-induced by the wing. However, even if the slipstream velocity field were to be relatively uniform, the finite slipstream height and width would alter the two-dimensional lift curve slope from 2π to a greater slope if the lift coefficient is normalized with the freestream velocity and smaller slope if normalized with the jet velocity.

The effective angle of attack is, therefore, instead derived by interpolating the slipstream induced velocities and the self induced velocities at the quarter chord point and calculating the effective angle of attack according to Equation 9.3.

$$\alpha_{eff} = arctan\left(\frac{U_\infty + u_{ind} + u_{ss}}{W_\infty + w_{ind} + w_{ss}}\right) \tag{9.3}$$

The evaluation at the quarter-chord is valid in case the airfoil can be approximated by a lumped vortex.

The effective angle of attack approximation practically models the loading of an arbitrary inflow with an equivalent uniform inflow to achieve equivalence in loading on the airfoil in the actual inflow. This is approximation is exact if the induced velocities are spatially constant and equal to the value at the quarter-chord point. The approximation performs worse as the difference between the induced velocity at the quarter-chord point and induced velocities at the different chordwise positions of the wing increases.

For example, if the main element experiences a constant external upwash and the flap experiences no external upwash, then the effective angle of attack will not account for the absence of the external upwash on the flap. The loading on the flap will, therefore, be overpredicted but also the loading on the main element will be overpredicted as the circulation effect on the main element is overestimated.

Therefore, the effective angle of attack determination method is expected to be sufficiently accurate for sections wherein the entire airfoil section is immersed in the slipstream and for slipstreams with minor spatial variation in induced velocities, such as cases with minor flap deflection, minor rotor incidence, and for large diameter-to-chord ratios.The accuracy of the effective angle of attack is expected to suffer outside of these conditions.

9.3. Decamber method

Using the effective angle of attack for each strip, the chordwise force distribution of MSES can be determined and compared with the chordwise force distribution of the VLM. One approach to match the results of an inviscid and viscous model is to match the strip lift coefficient by adapting the twist of the section as used in Hunsaker and Snyder [83], Ferraro et al. [52], Bohari et al. [53], and Alba et al. [84]. However, adapting the twist only matches the section lift coefficient but not the chordwise force distribution. All the while viscous effects on the loss of lift are primarily focused near the trailing edge of the main element and the flap, known as the ”decambering effect”. As a result, the twist adaptation causes the distribution of lift to be underestimated near the leading edge and overestimated near the trailing edge and on the flap. The mere twist adaption causes, therefore, a less accurate estimation of the induced velocity field and consequential less accurate estimate of the strip effective angles of attack.

The chordwise lift distribution between the inviscid model and viscous model can be more closely matched by increasing the parameters to adapt. Decamber methods use the chordwise distribution of camber as adaptation parameters to correct for viscous effects. Previously, decamber methods have been succesfully applied in the form of a two DOF decamber angle based correction by Mukherjee, Gopalarathnam, and Kim [82] and Γ-based correction on all VLM panels by Şugar Gabor, Koreanschi, and Botez [85]. The method of Mukherjee, Gopalarathnam, and Kim [82] is not applicable for a wing with a slotted flap as the method assumes that the lift and moment of the airfoil can be approximated with a three-term Fourier series approximation of a flat plate with a flap deflection which is inconsistent with the VLM used in the present research. The VLM will have different, more representative lift and moment predictions than the Four series approximation, leading to an inconsistent viscous correction. The Γ-based decamber method of Şugar Gabor, Koreanschi, and Botez [85] is consistent with the VLM used in the present research but not able to be used in combination with the finite slipstream correction in the present methodology. The Γ-based does not account for the circulation reduction due to the finite slipstream correction which does occur in the VLM, which would lead to inconsistent results for the correction of the panel circulations.

As the former mentioned decamber methods are inapplicable to slipstream immersed flapped wings, a novel decamber method is developed in the present research by adapting the twist of each chordwise panel in the inviscid model. This method is implemented by rotating the normal vectors on the vortex rings such that the partial lift on each chordwise panel is corrected for viscous effects. With the rotation of the normal vectors each respective panel in the VLM can be decambered uniquely. This makes the method essentially a hybrid of the method of Mukherjee, Gopalarathnam, and Kim [82], in which only two locations on each strip are decambered, and the method of Şugar Gabor, Koreanschi, and Botez [85], in which all panels are adapted but with a circulation adaptation instead of a camber adaptation. The rotation of the normal vectors to correct the chordwise lift coefficient distribution is schematically shown in Figure 9.3.

The present coupling method calculates the rotation of the normal vectors such that the correction term

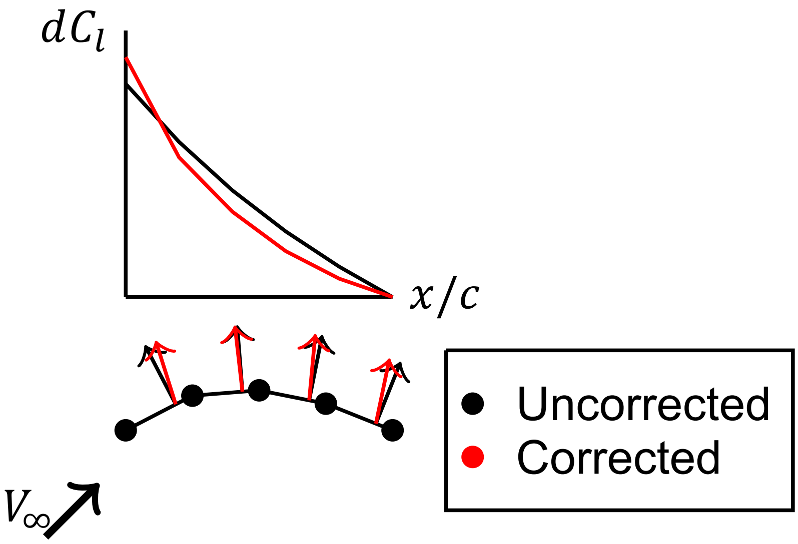

Figure 9.3: Schematic representation of the decamber method using the orientation of the panel normal vectors for the correction of the chordwise lift distribution. The black normal vectors and lift distribution represents the prediction with the normal vectors normal to the panels. The red 'normal' vectors represent the corrected orientation using the decamber method resulting in the adjusted lift distribution in red.

indicating the difference due to viscous, thickness, and compressibility effects, presented in section 9.1 is minimized. This is achieved by first calculating the decamber angles for a two-dimensional airfoil from the MSES. Second, the derived decamber angles of the two-dimensional solution are applied to a finite wing with the VLM.

The computation of the decamber angles in the two-dimensional coupling is first described in subsection 9.3.1. Thereafter, is the application of the decamber angles to a finite wing described in subsection 9.3.2.

9.3.1. Two-dimensional decamber solution

The rotation of the normal vectors are calculated from the coupling of a two-dimensional panel method with MSES. The two-dimensional panel method is developed as a two-dimensional version of the vortex ring VLM with no panels in spanwise direction and infinite bound vortices. This two-dimensional panel method uses the same panels on the camber line as used in the VLM such that the mesh of the VLM and the two-dimensional panel method are equivalent. The two-dimensional panel method will from hereon be referred to as the 2D Vortex Method (2DVM).

The normal vectors of the 2DVM are corrected such that the chordwise lift distribution of MSES and 2DVM are equal. Using a Newton-iteration scheme, is the difference between the 2DVM pressure and the pressure from MSES reduced by perturbing the orientation of the normal vectors. By reducing the difference between the lift of 2DVM and MSES, only the viscous, thickness, and compressibility effects are corrected for.

The normal vector orientation is calculated over a range of angles of attack. From these solutions, a linear interpolation function is calculated to provide the normal vector rotations of the panels as function of angle of attack. The Reynolds number is assumed constant along the wing to reduce the computational cost. This is a valid assumption outside of the slipstream as in the present research only untapered wings with constant chord are analysed. Within the slipstream, the Reynolds number is in reality higher. To account for the strips within the slipstream, MSES results with forced transition at the leading edge are used instead in these locations. The forced transition at the leading edge agrees with the observations found in literature [42, 43, 39]. As such, the normal vector orientations are calculated for both the forced transition case and the free transition case over the angle of attack range.

Using the solutions for the normal vector angles, a linear interpolation function is made for the rotations of the normal vectors as function of the effective angle of attack and whether the strip is within the slipstream or not. Using an interpolation function allows the normal vector rotations to not have to be calculated for each strip but only once for a range of effective angles of attack. The VLM can then be corrected for the viscous effects by calculating the normal vector rotations for each strip as function of the effective angle of attack of the respective strip. A flowchart of the process to calculate this normal vector rotation interpolation function is shown in Figure 9.4. An interpolation function is also made of the profile drag which is only a function of the effective angle of attack.

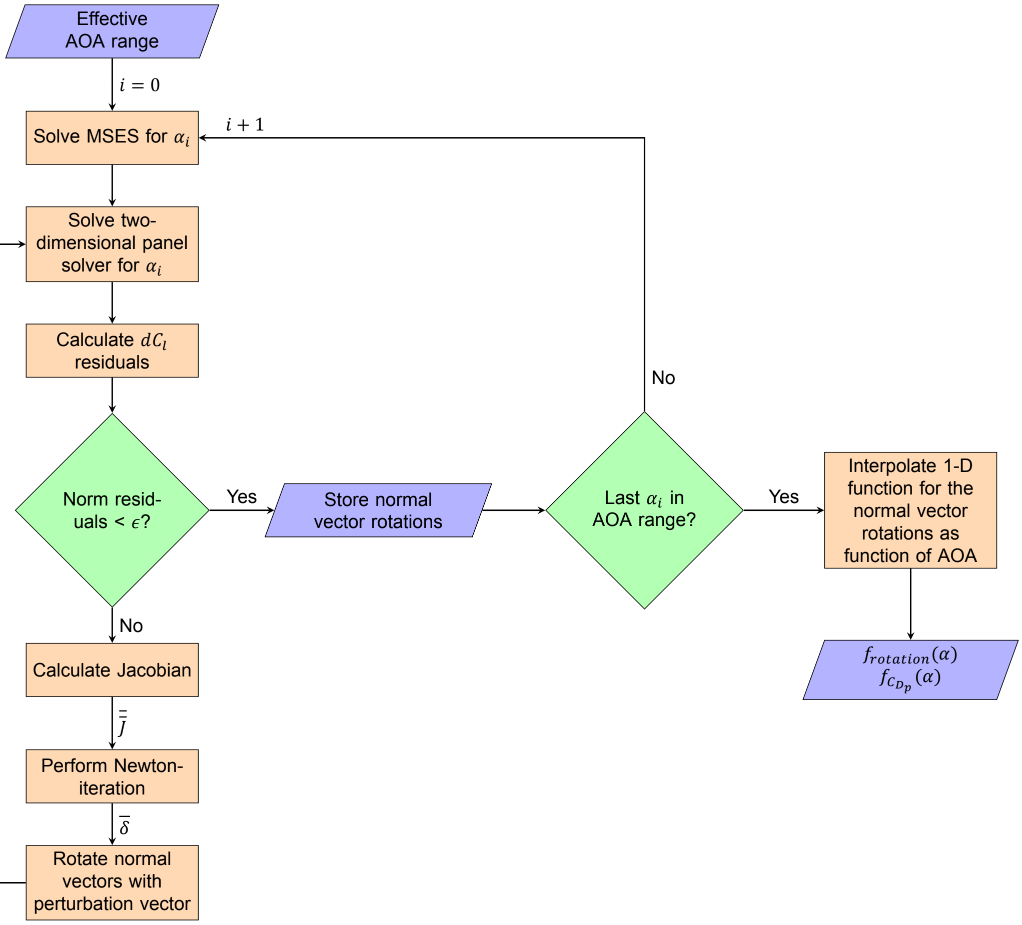

Figure 9.4: Flowchart of decamber method.

The Newton-iteration scheme shown in Equation 9.4 is solved for each iteration to determine the orientation of the normal vectors such that the chordwise lift distribution is corrected for viscous effects.

$$\bar{\bar{J}}\,\overline{\delta x} = -\bar{R} \tag{9.4}$$

In this scheme the residuals converge to a prior defined tolerance. The residual computation scheme uses the difference between the dC_l of a two-dimensional vortex ring VLM and the dC_l retrieved from MSES averaged along the respective panel chord location as shown in Equation 9.5. The integrals of the dC_l are calculated by integrating the Piecewise Cubic Hermite Interpolating Polynomial (PCHIP) fitted on the viscous chordwise lift distribution.

$$R_i = (dC_{l_{panel}})_i - (\overline{dC_{l_{MSES}}})_i = (dC_{l_{panel}})_i - \frac{\int_{x_i}^{x_i+\Delta x_i} dC_{l_{MSES}}(x)dx}{\Delta x_i} \tag{9.5}$$

Using the panel chord averaged dC_l allows for the viscous section lift coefficient to be enforced in the VLM irrespective of the fineness of the mesh in chordwise direction as derived in Equation 9.6.

$$\sum_{i=0}^{N-1} (\overline{dC_{l_{MSES}}})_i \Delta x_i = \sum_{i=0}^{N-1} \frac{\int_{x_i}^{x_i+\Delta x_i} dC_{l_{MSES}}(x)dx}{\Delta x_i} \Delta x_i = \int_0^c dC_l(x)dx = C_l \tag{9.6}$$

The Jacobian matrix is calculated by perturbing the orientation of the normal vector for each panel and recording the perturbation on the partial lift of each panel. The Jacobian elements are then calculated using a first-order finite difference scheme as shown in Equation 9.7.

$$J_{ij} = \frac{\partial dC_l)_i}{\partial \delta_j} \approx \frac{((dC_l)_i)_{perturbed} - (dC_l)_i}{\Delta \delta_j} \tag{9.7}$$

The perturbation vector that is solved in the Newton-iteration scheme contains the perturbation in the orientation of each normal vector and is multiplied by a damping factor of 0.4 before its input in the two-dimensional panel solver for the next iteration. The damping factor is chosen to be as large as possible while maintaining convergence stability.

After the norm of the residual vector is reduced below a threshold, a vector containing the rotations of each normal vector relative to the original orientation is stored. This process is repeated for every two degrees angle of attack within the set angle of attack range. The angle of attack range over which the decamber method is applied is determined from the effective angle of attack range found in the initial VLM solution. Once the rotation vectors for each angle of attack are calculated, they are linearly interpolated as function of angle of attack to provide a solution over the whole AOA range. An example of calculated rotations for a multi-element airfoil for an angle of attack range between -5 and 15 degrees is shown in Figure 9.5. The rotations are positive in pitch up direction. The interpolation function is also able to extrapolate at effective angles of attack outside of the interpolation range. The extrapolation can yield inaccurate results and the numerical tool therefore warns the user in such an occurrence.

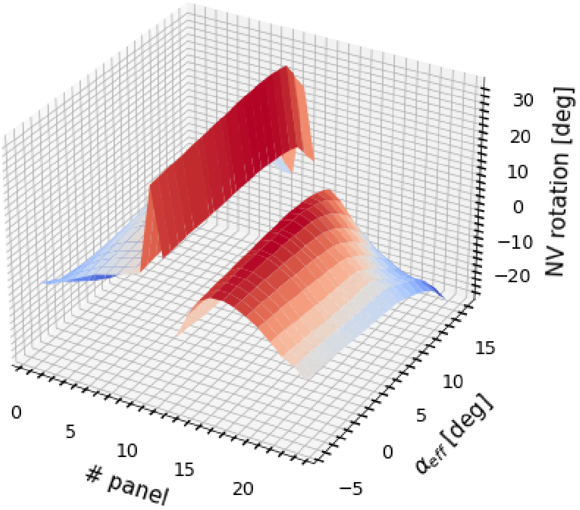

Figure 9.5: Example of rotations in pitch of panel normal vectors with respect to the uncorrected orientation for the different chordwise panels and effective angles of attack as calculated for the correction of the difference between the inviscid camber line panel solver and MSES predictions.

9.3.2. Application of decamber to a finite wing

The decamber solutions for the two-dimensional case are applied to the VLM to obtain the three-dimensional lift solution. First, the VLM is run without any decambering to obtain an initial solution for the effective angles of attack at each strip. The orientation (pitch angle) of the normal vectors in a strip are then calculated with the rotation vector interpolation function using the effective angles of attack computed by the VLM. The normal vectors of the VLM are rotated according to these rotation angles with a damping factor of 0.3 to stabilize the convergence. Afterwards, the VLM is ran again to compute the new effective angles of attack at each strip to which the process is repeated. Convergence is reached once the norm of the difference in orientation of each normal vector compared to the previous iteration is smaller than 0.05 degrees which has been shown to reach limit the error for the sectional lift coefficient to be below $1e-4$.

The inviscid-viscous coupling method does not only correct the inviscid lift of the VLM but also adds the profile drag as calculated by MSES to the VLM wing. After the evaluations of MSES at different sectional angles of attack a linear interpolation function of the profile drag as function of angle of attack is created. After convergence is reached for the lift by the coupling method, the effective angle of attack distribution is used to compute the profile drag at each strip using the interpolation function. The total profile drag is then simply computed by direct integration according to Equation 9.8. The integration is performed in the code with an trapezoidal integration scheme. Thereafter, is the total profile drag added to the total inviscid drag to obtain the total viscous drag.

$$C_D = \frac{1}{S}\int_{-b/2}^{b/2} C_{d_p}(y)c dy \tag{9.8}$$

9.4. Verification of decamber method

To verify the decambering method, the chordwise lift distribution as predicted by the uncorrected 2DVM (inviscid), camber corrected 2DVM (viscous), and experiments are compared. The NLR 7301 airfoil experiments performed by Van den Berg [86] is used for this purpose. The uncorrected 2DVM and camber corrected 2DVM predictions of the chordwise lift on the main and flap element are shown in Figure 9.6 together with the experimental results. The circular markers denote the position of the quarter-chord of each panel at which the dC_l of the panel is defined. The dC_l is derived from the pressure distribution of the experiments by calculating the difference in upper and lower surface pressure and taking the resultant pressure in lift direction.

The decambering method can be seen to effectively adjust the normal vectors such that a near perfect match between the chordwise lift distribution of the panel method and the experiment is achieved. The camber corrected dC_l is predicted lower than the values from the experiment near the leading and trailing edge. However, this is as designed, as the panel lift is set to be equal to the mean of the dCl distribution for the region spanning the local panel, which is lower than the maximum. This is done to ensure that the lift on the panel is equal to the lift of MSES in the region spanning the panel length as described section 9.3. Furthermore, it is shown that the uncorrected solution severely under predicts the lift on the main element and overpredicts the lift on the flap element.

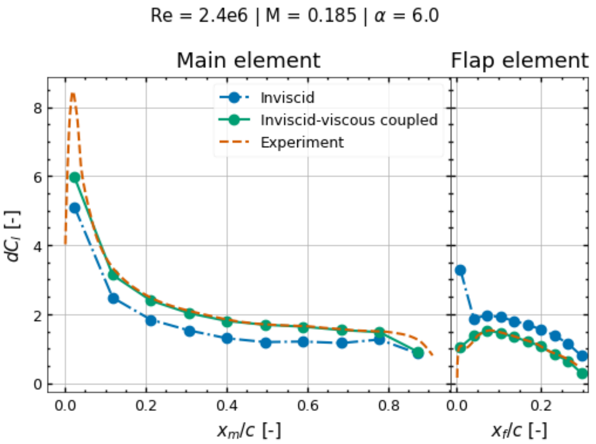

Figure 9.6: Chordwise lift distribution for the two-dimensional airfoil as predicted by the uncorrected 2DVM (2D panel method) and the camber corrected 2DVM together with the pressure distribution derived values from the experiments of Van den Berg [86] of the NLR 7301 airfoil at an angle of attack of 6 degrees, Reynolds number of $2.4e6$, and Mach number of 0.185.

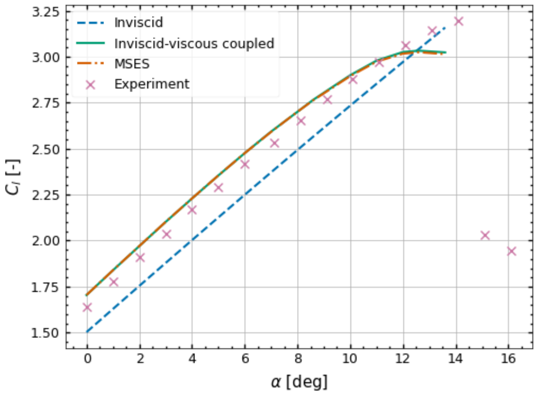

Figure 9.7: Sectional lift polar as predicted by the uncorrected 2DVM (panel method) and the camber corrected 2DVM together with the measured lift polar from the experiments of Van den Berg [86] of the NLR 7301 airfoil at a Reynolds number of $2.4e6$, and Mach number of 0.185.

It is further verified whether the correction to the chordwise lift distribution is able to result in a correct total sectional lift coefficient by comparing the total sectional lift of the camber corrected 2DVM solution with the sectional lift prediction of MSES and measured lift in the experiments of Van den Berg [86]. The total sectional lift is compared for angles of attack between 0 and 16.0 in Figure 9.7 with the cruise configuration used for the reference chord. MSES was not able to converge beyond 13.6 degrees angle of attack beyond stall and therefore limits the angle of attack range of the predictions. The limitation of MSES to converge at higher angle of attacks is a considerable limitation to the present methodology as a whole, and limits the applicable angle of attack range for which this method can be used.

An excellent match is observed between the sectional lift coefficient of the camber corrected 2DVM and MSES in Figure 9.7. This verifies that the pressure distribution from MSES is correctly converted to a chordwise lift distribution and that the decambering method is able to correct the total sectional lift coefficient of the inviscid camber panel method to the results of MSES. Furthermore, it can be observed that the coupling of the uncorrected 2DVM with MSES has three main effects. Firstly, the zero-lift angle of attack of the linear part of the polar is reduced which structurally increases the lift coefficient across the angle of attack range. The underprediction in lift agrees with the observations in the chordwise lift distribution of Figure 9.6 and is further investigated in subsection 9.4.1. Second, the slope of the linear part of the polar is slightly increased due to the effect of thickness which the inviscid camber panel neglects. Lastly, the curve is made non-linear at high angles of attack due to the viscous effects.

Comparing MSES with the measured lift in Figure 9.7 shows an overprediction of the lift at angles of attack up until 10 degrees with a constant error of around 0.06. This overprediction of lift in MSES for the NLR 7301 airfoil is also observed in the research of Zelst [87]. In this research it is observed that the discrepancy is caused by the overprediction in the suction peak in MSES as is also observed in section 8.4. A study on the grid resolution and turbulent amplification factor by Zelst [87] yielded no change in this discrepancy. It is therefore not entirely clear what the cause of this discrepancy is.

A difference in the stalling behaviour is also noticed between MSES and the experiment in Figure 9.7. MSES predicts a more gradual stall whilst a more abrupt stall is observed in the experiments. Furthermore, both the maximum lift and stall angle of attack are underpredicted by MSES. These discrepancies were also observed by Zelst [87] and further investigated. In this study it is shown that the turbulence amplification factor has a large influence on the agreement between MSES and the experiments for both the stalling behaviour in the lift polar as well as for the boundary layer properties. In the present research a turbulence amplification factor of 9 is used in the MSES analyses of wings in clean air. This factor corresponds to the lowest amount of turbulence as one would expect in clean and laminar flow conditions. However, a turbulence amplification factor of 3 allows for a better agreement with the experiments of Van den Berg [86] as concluded by Zelst [87]. This is due to the fact that the boundary layer properties of the lower surface agrees better with the experiments such that no separation is predicted in this area. The cause of this could be due to higher turbulence values in the wind tunnel or higher surface roughness of the model. A comparison between the lift polars of MSES for an amplification of 9 and 3 is shown in Figure 9.8. Here it can be seen that indeed a better agreement in lift is observed for a turbulence amplification factor of 3 which results in a more sudden and delayed stall. However, the maximum lift coefficient as well as stall angle of attack is still underpredicted by MSES.

9.4.1. Investigation into zero-lift angle of attack change

The inviscid-viscous coupling is shown to correctly alter the normal vectors of the panels to match with MSES. However, the discrepancy between the zero-lift angle of attack of the uncorrected 2DVM and MSES is surprising. The coupling to MSES is primarily used to correct for viscous effects which are expected to occur at high angles of attack, however, here it is shown that the lift is drastically underpredicted at low angles of attack due to a severe underprediction of lift on the main element by the uncorrected 2DVM.

The discrepancy in lift at low angles of attacks is further investigated by comparing the chordwise lift distribution of the uncorrected 2DVM with a viscous (regular) camber corrected 2DVM and an inviscid camber corrected 2DVM. These three different distributions are shown in Figure 9.6. The inviscid camber corrected 2DVM solution is obtained by coupling with MSES for which the Reynolds number and Mach are set to zero. A Reynolds number of zero in MSES results in an inviscid analysis using the Euler equations without any boundary layer modelling and a Mach number of zero results in an incompressible flow analysis. The coupling with this set up of MSES, therefore, only corrects for thickness effects.

Comparing the uncorrected 2DVM with the inviscid camber corrected 2DVM in Figure 9.6 reveals

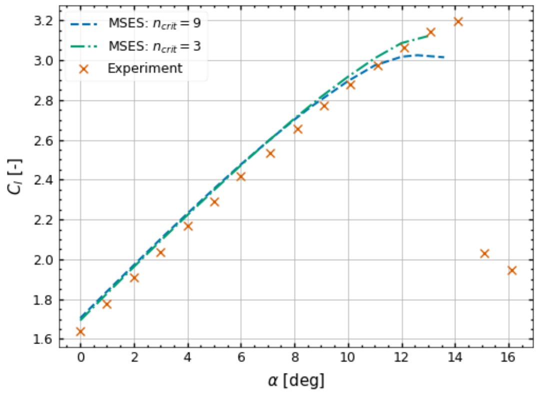

Figure 9.8: Sectional lift polar from the experiments of Van den Berg [86] together with the predicted lift polar by MSES for two turbulent amplification factors used in the boundary layer transition model.

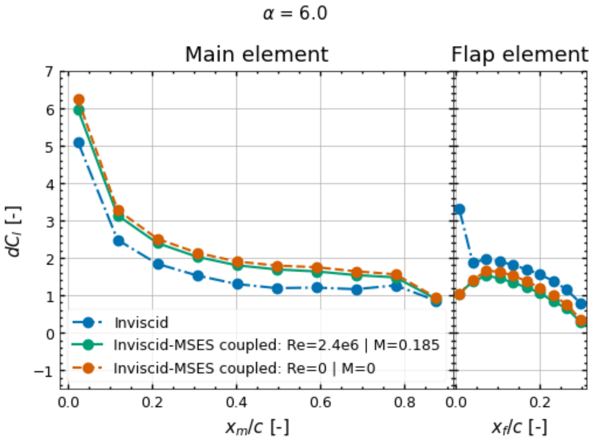

Figure 9.9: Chordwise lift distribution of the two-dimensional airfoil at zero Reynolds number (inviscid) as predicted by the inviscid camber panel method, the corrected camber panel method and MSES for the LFC airfoil at an angle of attack of 0 degrees.

the same discrepancies as observed in the coupling with the regular viscous MSES. The origin of the discrepancies can, therefore, be found in a difference in the inviscid modelling of the vortex ring VLM and MSES. One cause could be that the discrete vortices cause erroneous results with two elements in close proximity. Katz and Plotkin [66] recommends to use a panel density for multi-element airfoils with a panel length of one tenth of the gap between the elements and to align the control points of the two elements at the overlap. However, the elements do not overlap for this airfoil and the discrepancy is observed to remain when run for 400 panels which allows for the panel length requirement. The cause of the discrepancy is therefore likely due to the lack of thickness modelling. For potential flows, thickness of a single element airfoil slightly increases the lift curve slope but does not influence the zero-lift angle of attack [88]. However, this does not have to be the case for multi-element airfoils. The effect of thickness in each element can result in secondary effects in multi-element airfoils as the increase in lift of one element has a direct influence on a change in lift of the other element due to the circulation effects. The thickness could therefore not only change the lift curve slope but also the zero-lift angle of attack due to these secondary effects.

To verify the thickness theory, the coupling between the inviscid camber panel method and inviscid MSES is applied on a thin and thicker airfoil with the same camber line and the results are compared. For this purpose the NACA 0006 and NACA 0016 airfoil are chosen with 6% and 16% thickness, respectively. The same airfoil is used for both elements with an equal gap of $0.110c$, overlap of $-0.056c$ and flap chord fraction of $0.338c$ with the main element chord as reference chord. The polars are shown in Figure 9.10 and the chordwise lift distributions at an angle of attack of 6 degrees is shown in Figure 9.11. It is indeed observed in both the lift polar and chordwise lift distribution that the discrepancy between the uncorrected 2DVM and the inviscid camber corrected 2DVM grows with increasing thickness. In Figure 9.10 the effect of thickness is shown to not be zero at zero lift unlike the single element airfoil case but also causes a reduction in zero-lift angle of attack. In Figure 9.11 it is also shown that especially the inviscid lift on the main element is increased with increasing thickness whilst a minor decrease in lift on the flap is observed. This is in contrast with the larger overprediction in lift by the 2DVM on the flap as observed for the NLR7301 airfoil which is likely due to the fact that the gap is much smaller for the NLR7301 airfoil causing the circulation effects of the main element on the flap element to be larger here. As a result, the underprediction on the main element lift causes a larger underprediction in downwash on the flap element for this case.

To conclude, the neglected thickness in the uncorrected 2DVM causes a considerable underprediction in section lift coefficient for thick multi-element airfoils. This underprediction is also present in the VLM of the present method as the 2DVM is simply a two-dimensional adaptation of the vortex ring VLM and because these effects are independent of spanwise effects. However, the limitation of the 2DVM and

VLM to account for thickness is not an issue in the present methodology as the coupling with MSES is able to correct for the thickness effects. As a result, the inviscid-viscous coupling method mostly corrects for the lack of thickness modelling in the VLM at low angles of attack whilst also correcting for viscous effects at larger angles.

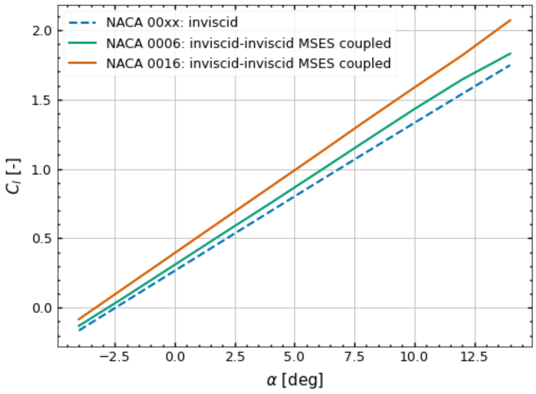

Figure 9.10: Lift polars of the inviscid 2DVM and for the 2DVM coupled to an inviscid MSES with varying airfoil thickness.

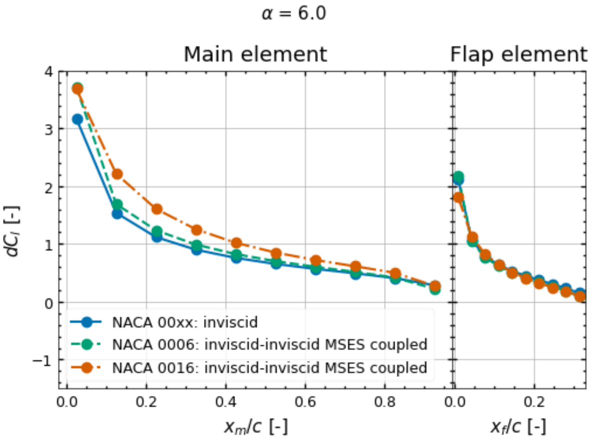

Figure 9.11: Chordwise lift distribution of the two-dimensional airfoil as predicted by the uncorrected 2DVM, the corrected 2DVM and MSES for the LFC airfoil at an angle of attack of 6.0 degrees.

9.5. Convergence analysis of decamber method

In this section the convergence of the decamber method is analyzed. First, the convergence of the camber adaption (normal vector rotations) is analyzed in subsection 9.5.1. Thereafter, the convergence in mesh size is analyzed in subsection 9.5.2.

9.5.1. Camber convergence

The convergence of the Newton-iteration scheme on the two-dimensional panel method used in the decamber method is investigated. In the camber adaptation process the normal vectors of the two-dimensional panel method are iteratively rotated until the difference in chordwise lift distribution between the panel method and MSES is sufficiently small. For this purpose, the Newton-iteration scheme is executed until the norm of the residual vector is below $1e-2$. In Figure 9.12 the progression of the residual norm against the amount of Newton-iterations is shown. It is observed that convergence is reached in six iterations.

The second iterative loop in the decamber method occurs when the camber angles of the two-dimensional panel method are applied on the three-dimensional VLM using an interpolation function of the two-dimensional camber adaptation as function of strip angle of attack. The normal vector orientations are calculated at each strip of the VLM and applied to the panels in the respective strip using the effective angle of attack distribution of the previous iteration. The normal vector rotations changes the effective angle of attack distribution once again, to which the new normal vector orientations are calculated. Convergence in this loop is reached once the norm of the vector containing the difference in normal vector orientations between current and previous iteration is reduced to less than $5e-2$. The convergence tolerance magnitude was set such that the difference in lift and drag coefficient of the present and previous iteration is lower than $1e-4$. In Figure 9.13 the progression of the normal vector orientation error term against the amount of iterations is shown. Convergence is shown to be achieved within 16 iterations.

9.5.2. Mesh convergence

The mesh convergence for the analysis of a high-lift wing with the inviscid-viscous coupling method is investigated. The fineness of the VLM mesh has a considerable influence on the present inviscid-viscous coupling method. The amount of spanwise panels determines the granularity of the spanwise

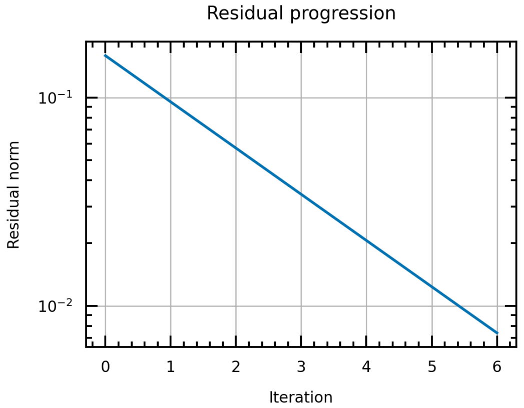

Figure 9.12: The progression of the norm of the residual vector (panel lift difference between two-dimensional panel method and MSES) against the amount of iterations for the Newton-iteration scheme used in the 2D panel method part of the camber adaption method.

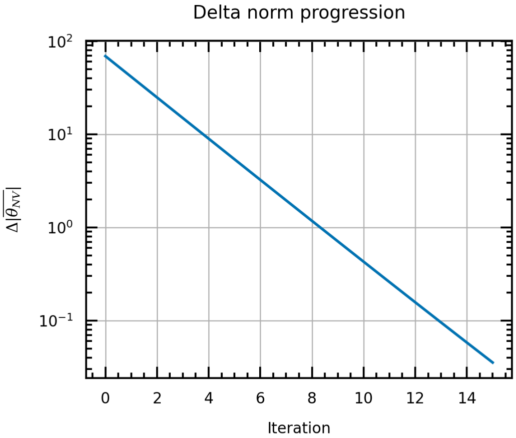

Figure 9.13: The progression of the norm of the VLM normal vector orientation difference against the amount of iterations for the iteration loop in the VLM part of the camber adaption method.

differentiation in normal vector orientations. Furthermore, the amount of chordwise panels determines the amount of variables for the decambering in a strip, with a larger amount allowing for a more accurate representation of the chordwise lift distribution. A finite wing with an aspect ratio of 5.9 and a single-slotted flap as used in the validation of MSES in section 8.4 is used for this purpose.

The relative error in total lift coefficient compared to the most fine mesh is shown in Figure 9.14. m denotes the amount of spanwise panels for one half of the wing. n denotes the amount of chordwise panels on each element, wing and flap, separately. The same amount of chordwise panels are chosen for each element as similar gradients in chordwise lift are expected on separate elements. The lift coefficient is observed to be underpredicted at small n and quickly converges to within 1% of the fine mesh at a value above 8. In contrast, the lift coefficient is overestimated at small m and converges within 1% of the fine mesh at values above 10.

The relative error in total drag coefficient compared to the most fine mesh is shown in Figure 9.14. The error in drag coefficient is observed to be largely dependent on the chordwise panels. The predictions of drag at the minimum evaluated amount of spanwise panels of six is already close to the fine mesh for sufficiently large amount of chordwise panels. Similarly to the lift coefficient error, are 10 or more chordwise panels required for sufficient convergence.

Both lift and drag coefficients within 1% of the fine mesh prediction are observed for meshes with 12 or more spanwise panels and 10 or more chordwise panels. These values are, therefore, used in the validation and analyses of rotor-less geometries.

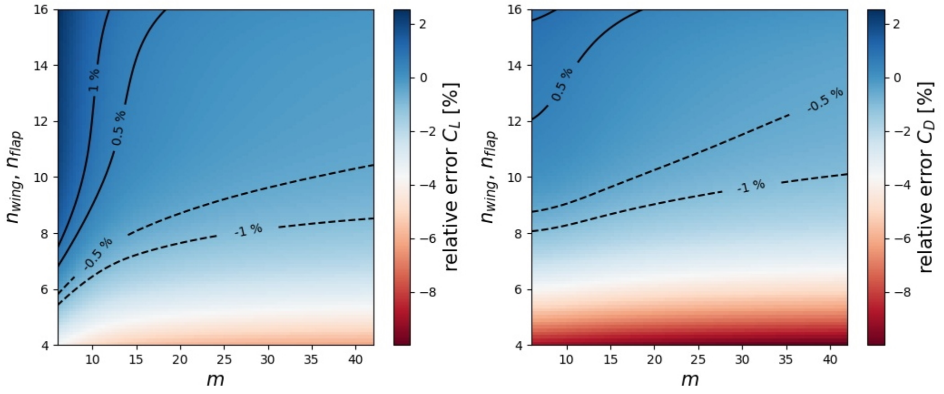

Figure 9.14: Relative error in wing lift coefficient (left) and drag coefficient (right) for different mesh settings compared to the most fine mesh. m denotes the amount of spanwise panels per semi-span and n the amount of chordwise panels on the wing and flap separately.

10

Convergence of integrated tool

The different modules of ORWFIS are integrated into a single analysis tool. In this chapter the convergence of the analysis tool is investigated. First, the convergence of the rotor-wing coupling is investigated in section 10.1. Thereafter, the convergence on the mesh size is studied in section 10.2. Lastly, the computational time for the different modules as function of mesh size is analyzed and presented section 10.3

10.1. Rotor-wing coupling convergence

The rotor inflow and forces, slipstream deflection, and wing loading are iteratively solved. The convergence on these iterations is validated by investigating the progression of the rotor thrust, torque, normal force, wing lift, and wing drag. Convergence is reached once the difference of these parameters with respect to the previous iteration is less than $1e-4$. The progression of these difference terms against iterations for a an ORWF geometry with with a leading edge rotor and a 30 degree deflected single-slotted flap at an angle of attack of five degrees is used and shown in Figure 10.1. It can be observed that convergence on all terms is reached with just three iterations.

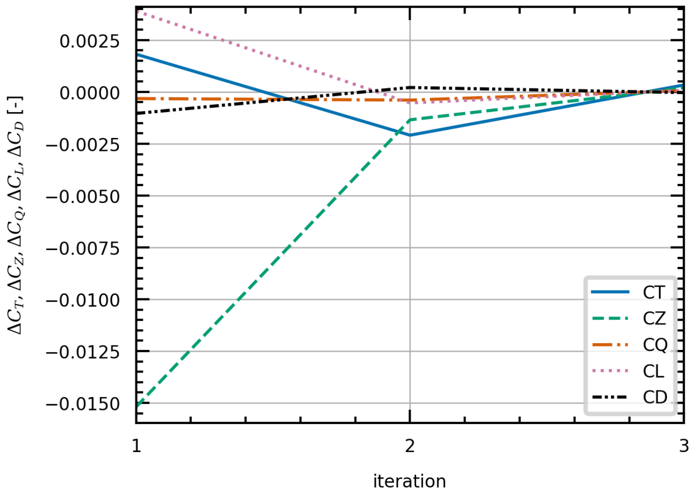

Figure 10.1: Progression of the difference in rotor and wing forces of each consecutive iteration in the ORWFIS rotor-wing coupling loop.

10.2. Mesh convergence

The convergence of the aerodynamic predictions with mesh refinement is studied for the complete analysis tool. For this purpose, an ORWF geometry with with a leading edge rotor and a 30 degree deflected single-slotted flap at an angle of attack of five degrees is used. The analysis ran with an infinite span analysis such that tip effects are avoided. The fineness of the wing mesh is dependent on four variables: the spanwise amount of panels, m, the chordwise amount of panels on the main wing, n_{wing}, and flap, n_{flap}, and the spanwise amount of panels for the slipstream immersed wing sections, m_{rotor}. The integration of the rotor slipstream changes the convergence to the mesh fineness compared to a wing without slipstreams. The amount of spanwise and chordwise panels in the slipstream determine how well the spatial variations in the slipstream induced velocity field are captured. Furthermore, the amount of spanwise panels in the slipstream also determines the accuracy of the finite slipstream correction. For this study, the amount of spanwise panels outside of the slipstream is fixed and kept at a value of 16 panels. The effect of the spanwise panels outside of the slipstream on the convergence is not expected to differ greatly from a wing without a rotor. In section 9.5 it was observed that a minimum of 12 spanwise panels is sufficient. The amount of spanwise panels outside of the slipstream is therefore set to 16 to be certain of convergence.

The relative error of the lift coefficient compared to the finest mesh is shown for different slipstream immersed mesh and chordwise mesh settings in Figure 10.2. The lift coefficient is shown to converge steeply beyond 30 spanwise panels in the slipstream. A minimum of 51 spanwise panels in the slipstream are required to prevent an overestimation of the lift and to achieve a relative error of less than 1%. Furthermore, at least 8 chordwise panels are required to limit the relative error to less than 1%. To guarantee convergence, 12 chordwise panels per element and 51 or more spanwise panels in the slipstreams are used.

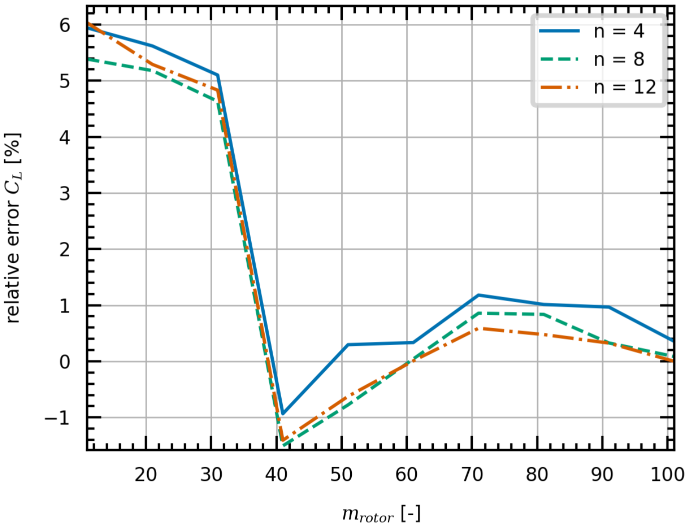

Figure 10.2: Relative error in system lift coefficient for different mesh settings compared to the most fine mesh. m_{rotor} denotes the amount of spanwise panels in each slipstream immersed wings section and n the amount of chordwise panels on the wing and flap separately.

10.3. Computational time

The computational time of the ORWFIS analysis tool for an ORWF configuration is investigated. The investigation has been ran on a computer with the following specifications:

- Processor: Intel(R) Core(TM) i7-4710MQ CPU @ 2.50GHz, 4 Core(s), 8 Logical Processor(s)
- Installed Physical Memory (RAM): 8,00 GB

A heatmap of the computational time against the amount of chordwise panels and spanwise panels is shown in Figure 10.3. It can be observed that the computational time is mostly dependent on the amount of panels in the slipstream (m_{rotor}). Furthermore, a computational time of less than 10 minutes can be achieved with the required mesh settings found in the mesh convergence analysis.

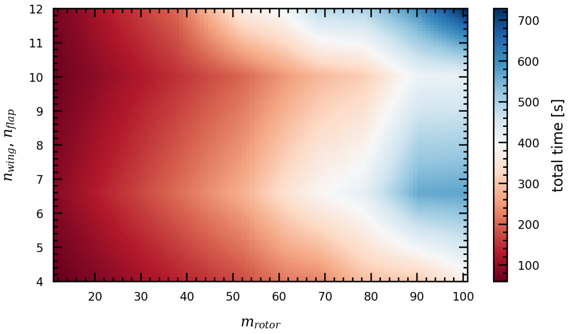

Figure 10.3: The computational time of the ORWFIS analysis tool for an ORWF configuration.

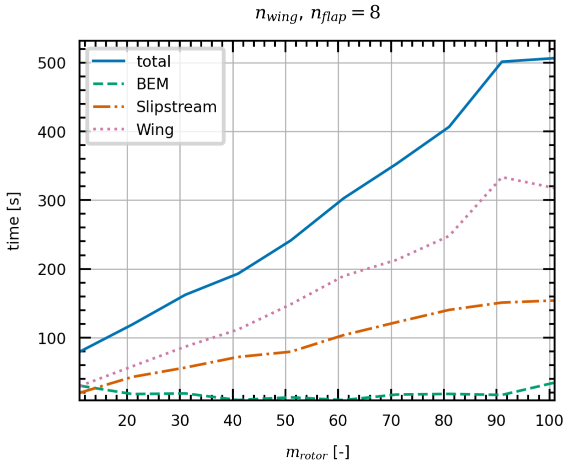

Figure 10.4: The computational time for the different modules in the ORWFIS analysis tool for an analysis of an ORWF configuration.

The computational time of the different analysis modules against m_{rotor} is shown in Figure 10.4. It can be seen that the computational time of the BEM is relatively constant with the amount of spanwise panels. The computational time of both the slipstream and the wing module increase linearly with the the amount of spanwise panels in the slipstream immersed wing section. This is as expected, as the increase in panels results in more points in the slipstream model to be evaluated. Furthermore, the increase in panels increases the finite slipstream correction computation, the decambering of the wing, and setting up the aerodynamic influence matrix and solving. The wing analysis module can be seen to be the largest contributor to the total computational time and, from further investigation, is largely attributed to the finite slipstream correction computation.

III

Validation & analysis

11

Validation

In this chapter the ORWFIS analysis tool is validated using experimental data from literature. First, the unpowered high-lift configuration is validated in section 11.1. Thereafter, are the modelling of the rotor and slipstream interactions on the wing validated for a wing in cruise configuration in section 11.2. Finally, the validation of the complete analysis tool for a wing in high-lift configuration is presented in section 11.3.

11.1. Unpowered high-lift configuration validation

The analysis tool is validated for an unpowered high-lift configuration using two different experimental datasets. The first dataset is used to validate the sectional lift coefficient as described in subsection 11.1.1. Thereafter, is the chordwise lift distribution validated of a section in a finite wing with the second experimental dataset from literature as described in subsection 11.1.2

11.1.1. Sectional lift coefficient comparison

The numerical analysis tool for a wing with nested flaps and without a leading edge rotor is validated. For this purpose the, as of yet unpublished, results of a wind tunnel experiment by Duivenvoorden et al. [64] are used. In this experiment a wall-to-wall unswept and untapered wing with a flap and possibility to install a leading-edge rotor is used. For the present validation, the dataset for the configuration with the rotor and nacelle disassembled is used.

The experiments were performed at the Low Turbulence Tunnel (LTT) at the Delft University of Technology. The LTT has a turbulence level of 0.015% at the velocity of 30 m/s used in these experiments.

The wing featured a NLF-Mod22(B) airfoil used in the experiments by Boermans and Rutten [89] with a span of 1.248 meters and a reference nested chord length of $0.3mm$. The comparison is performed with a 30 degree flap deflection, 0% overlap and 3% gap length with respect to the nested chord length. The wing features zigzag tape on the upper surface of the main wing at the 10% chord location for boundary layer tripping. Furthermore, pressure taps were located on the main and flap element at spanwise stations 0.3 chord lengths from the wing center at the port- and starboard side. The experiments used for this validation were ran at a Reynolds number of $5e6$. The measurements were taken over an angle of attack range between -5 and 15 degrees. The geometry of the model with the flap retracted is shown in Figure 11.1. Note that for the present validation the measurements of the wing with the rotor and nacelle detached are used and with the flaps deflected by 30 degrees.

The lift polar as predicted by ORWFIS is shown in Figure 11.2 together with the integrated lift coefficients of the experiment at both pressure tap locations. The nacelle is taken off for these measurements and wind tunnel wall corrections according to the method of Allen and Vincenti [90] have been applied. MSES was only able to converge between an angle of attack of 0 and 6 degrees. The predictions of ORWFIS beyond these angles are, therefore, calculated with extrapolated results from MSES and these are marked in by the red square markers.

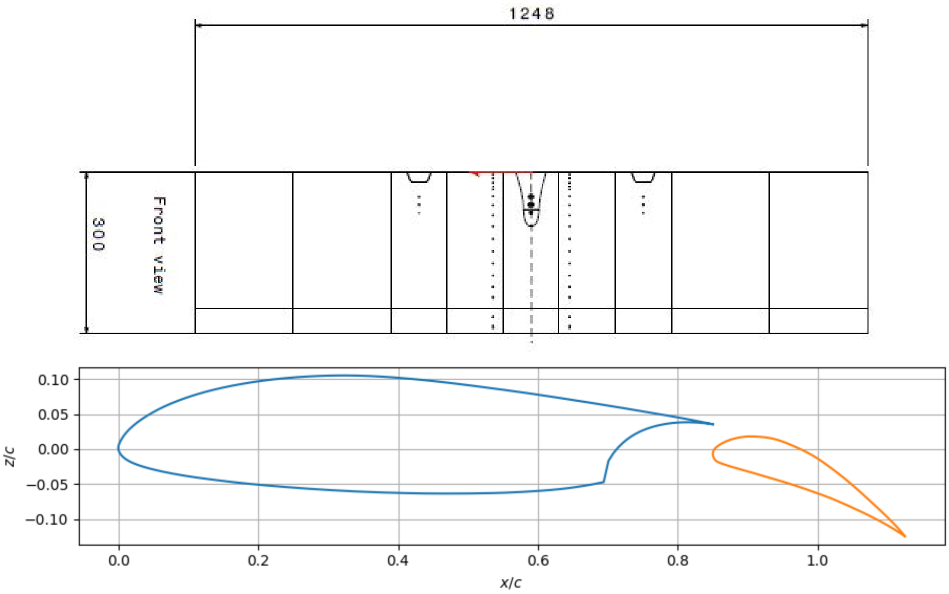

Figure 11.1: Wing and airfoil geometry of the experiments of Duivenvoorden et al. [64]. The configuration with the rotor detached is used for the present validation of the unpowered high-lift configuration. Top figure modified from Duivenvoorden et al. [64].

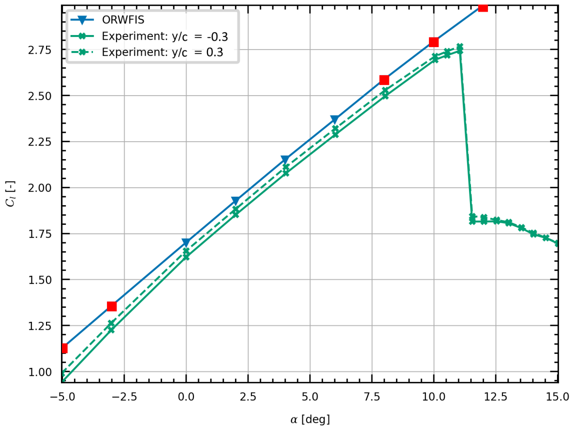

Figure 11.2: Sectional lift polar for rotor-off conditions as predicted by ORWFIS and as measured in the experiments at a distance of 35% diameter from the wing center starboard and port side. The red square markers indicate extrapolated results at which MSES was unable to converge.

The slight differences between the two integrated lift coefficients of the experiment are attributed to spanwise variations which were observed during the experiment [64]. The lift predicted by ORWFIS between 0 and 8 degrees is slightly higher than derived from the experiment with a discrepancy of 0.05. This is mainly due to a discrepancy in zero-lift angle of attack. This is likely MSES overestimating the lift. In the experiments of Coder, Maughmer, and Somers [91] a comparable airfoil with a slotted flap was tested at a similar Reynolds number of $7e6$ and compared with MSES. In this research the C_l was overestimated in a similar fashion as observed here. Coiro, Nicolosi, and Grasso [92] mentioned in as well that they observed over-predictions in lift by MSES, especially for gap values larger than 0.02. With a gap of 0.03 of the present airfoil studied, it is also expected to occur for this geometry. No definitive conclusion is drawn in the literature on why this is the case, but it could very well be due to limitations in the boundary layer modelling which causes the decambering in MSES to be underpredicted. Altogether, the prediction of lift by ORWFIS in this angle of attack regime is reasonably good.

At angles of attack below zero degrees, a larger discrepancy is observed due to a difference in lift curve slope. At negative angles of attack a higher lift curve slope is observed which could not effectively be captured by ORWFIS as MSES was not able to converge in this range of angles of attack. At angles of attack between 8 and 11 degrees the lift curve slope is shown to decrease in the experiments due to increased decambering as the stall angle of attack is approached. ORWFIS is unable to capture the full decambering effects at these angles as well as MSES was unable to converge beyond 6 degrees angle of attack. The stall point could, as a result, not be predicted by ORWFIS. The analysis has therefore been limited to 11 degrees angle of attack. The inability of MSES to converge beyond a certain angle of attack range has a major influence on the quality of the predictions at negative and high angles of attack, which directly limits the angle of attack range at which the predictions of the ORWFIS analysis tool are valid.

11.1.2. Chordwise lift distribution comparison

For the validation of the chordwise lift distribution, the results of the wind tunnel experiment of Applin and Gentry Jr. [93] are used. In this experiment a semi-span straight finite wing with a single slotted flap is tested at a Reynolds number of 3.33e6 and a Mach number of 0.14. A slightly modified version of the NASA Advanced Laminar Flow Control (LFC) airfoil section was used and is shown in Figure 11.3. The pressure distribution was measured at 44% of the semi-span length.

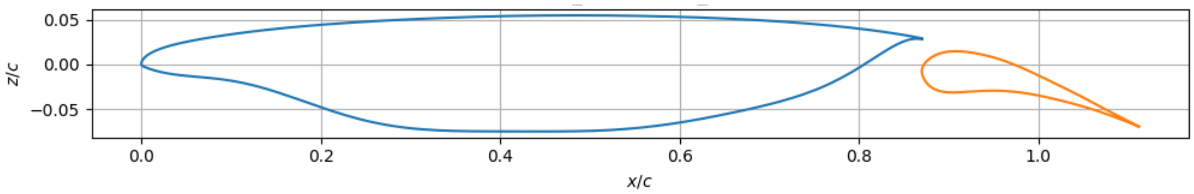

Figure 11.3: Airfoil used in the experiments of Applin and Gentry Jr. [93].

The predicted chordwise lift distribution at 44% semi-span length is compared with the chordwise lift distribution derived from the measurements of Applin and Gentry Jr. [93] as shown in Figure 11.4. The chordwise lift distribution of the experiment is derived by integrating the measured pressure coefficient around the profile surface.

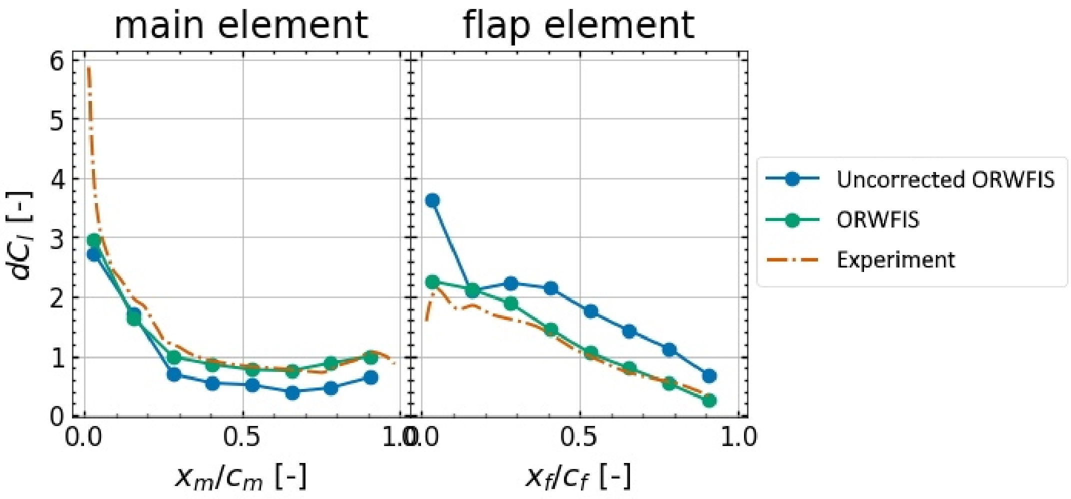

Figure 11.4: Chordwise lift distribution on main and flap element as predicted by the uncorrected (no decamber method applied) ORWFIS solution and the corrected ORWFIS solution as well as lift distributions derived from the experiment of Applin and Gentry Jr. [93]. Distribution is at spanwise strip of 44% semi-span with an angle of attack of 7.8 degrees.

The predicted chordwise lift distribution matches quite well with the measured distribution for the main element unlike the lift distribution predicted by ORWFIS without the decamber correction method, which underestimates the lift on the main element. The dC_l looks to be underpredicted at the leading edge of the main element on first sight. However, it should be noted that the correction matches the total lift of the leading edge panel (which is the dC_l value at the panel times the panel chord) with the total lift of MSES spanning the panel chord length (area under the dC_l curve spanning the panel chord). The dC_l of the leading edge panel is, therefore, by design lower than the local value of MSES. The local

dC_l can be matched closer with each other by refining the mesh, but this is intentionally not done as it increases the computational cost while it has marginal influence on the accuracy of the total sectional lift prediction of the wing as shown in subsection 9.5.2, which is the key objective of the present research.

For the flap, the local lift is seen to be slightly overpredicted near the leading edge of the flap at the second and third datapoint. However, much less than observed for the predictions without the decamber correction, for which the slat effect is not captured properly.

Concluding, the ORWFIS analysis tool is able to predict the total lift of a wing with deflected single-slotted flaps reasonably well but is as good as the quality of the solutions received from MSES. Furthermore, for a finite wing the chordwise lift distribution of section in the semi-span is predicted reasonably well by ORWFIS on both the main and flap element. This indicates that it is also able to perform with three-dimensional effects included which effectively alter the angle of attack seen at different spanwise stations.

11.2. Powered cruise configuration validation & analysis

The numerical analysis tool with rotor and wing interactions is first validated for a wing in cruise configuration without deployed flaps. The wind-tunnel experiments of Sinnige et al. [94] are used for the validation of a finite half-wing with one closely coupled rotor in a tractor configuration at an inboard spanwise position. The experiments are performed in the Low-Turbulence Tunnel at Delft University of Technology. The experiments were ran at a freestream velocity of 40 m/s, resulting in a wing Reynolds number of 650,000, and a turbulence level below 0.1%. Three different models were tested, however, for the present validation only the results of the conventional configuration are used. The propeller model features four blades with a diameter-to-(nested) chord ratio close to one and the wing model is a straight untapered wing with an aspect ratio of 6.2. The propeller is spanwise positioned at 44.4% semi-span length, chordwise oriented $0.853R$ in front of the wing leading edge and vertically positioned $0.042R$ lower than the wing chord line. Transition is fixed using strips with carborundum particles at a distance of 8% chord length from the leading edge on both upper and lower surface. Transition is equally forced at the same locations in MSES for usage as viscous correction. The experiments are performed at angles of attack between -8 and 10 degrees for a prop-off case where the propeller is uninstalled and for two prop-on cases at advance ratios of 0.7 and 0.9. The geometry of the wing model is shown in Figure 11.5

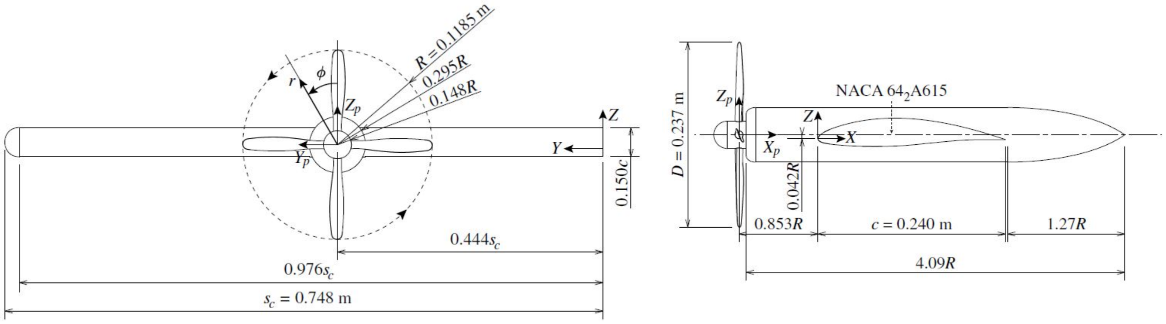

Figure 11.5: Wing and propeller geometry used in the validation of the powered clean wing configuration. Figure from Sinnige et al. [94].

The predicted total system lift polar for the unpowered configuration and two powered configurations are shown in Figure 11.6 together with the measured total lift in the wind tunnel experiments. The total system lift here includes the lift of the whole system including the forces of the rotor and wing. For the prop-off case, the zero-lift angle of attack is underpredicted contributing to a lift overestimation at lower angles of attack. The lift curve slope is overpredicted at low angles of attack, correctly predicted at medium angles of attack and underpredicted at higher angles of attack. As a result, the lift is slightly overpredicted at low angles of attack but matches better at higher angles of attack. This indicates that the inviscid-viscous coupling performs well at capturing the effects that are dominant at higher angles of attack. The discrepancy in the zero-lift angle of attack is likely due to the nacelle which produces zero lift at zero angle of attack and negative lift at negative angles of attack. As a result, the nacelle effectively slightly decambers the total wing.

The prop-on cases correctly show an increase in the lift curve slope. For an advance ratio of 0.9 a minimal increase in lift is observed in line with the lift increase of the validation data. At higher angles of attack the lift increase is slightly underpredicted. For an advance ratio of 0.7 a more considerable increase in lift curve slope is predicted which is also observed in the validation data. However, also for this advance ratio the lift augmentation is slightly underpredicted at higher angles of attack.

The predicted total system drag polar for the unpowered configuration and two powered configurations are shown in Figure 11.7 together with the measured drag in the wind tunnel experiments. The system drag here is of the whole system including the forces of the rotor and wing, with the rotor thrust essentially reducing the system drag. For the prop-off case the drag is slightly underpredicted with an increasing underprediction at higher absolute lift coefficients. This is due to the nacelle in the wind tunnel model which is not modeled in the numerical analysis. The nacelle increases the parasitic drag due to its larger chord than the regular wing and junction flows at the nacelle-wing interface. Furthermore, at higher angles of attack the profile drag is underpredicted by ORWFIS as larger regions of the wing stall, increasing the pressure drag locally.

For both prop-on cases the drag coefficient is predicted more closely to the validation although the discrepancies at higher angles of attack are here present as well. The closer match in total drag is therefore the result of an overestimation of the total drag increase due to the prop-on configurations as the underprediction in drag in prop-off configuration is compensated for. The overprediction in total drag is then either due to an underestimation of the rotor thrust, overestimation of the increase in wing drag due to the slipstream interactions or a combination of both. Willemsen [59] has validated the propeller analysis method that is used in the present theory for the same propeller geometry as used by Sinnige et al. [94]. Here it is shown that the thrust coefficient matches reasonably well at an advance ratio of 0.9 and that the thrust coefficient is slight under estimated at an advance ratio of 0.7. As a result, it is therefore likely that the overestimation in wing drag coefficient can be attributed to the slipstream interactions, specifically the profile drag as the overestimation is also observed at low lift coefficients. The overestimation in profile drag due to the slipstream interactions could be the result of an overestimation of the effective angles of attack due to the slipstream swirl effect which leads MSES to predict early onset of separation at the local spanwise strip. This could be aggravated by the inability of the numerical analysis method to model the delayed or prevention of separation in the slipstream immersed wing sections as observed in Sinnige et al. [94].

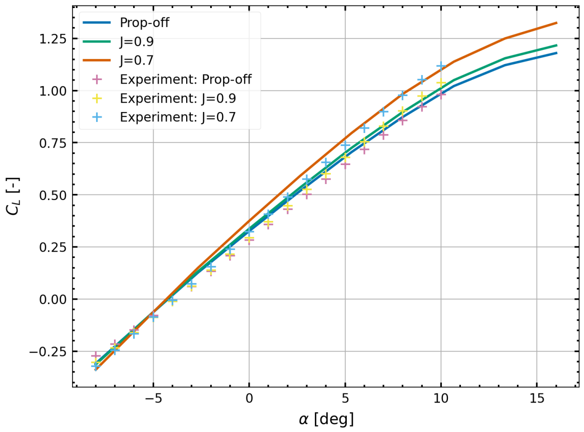

Figure 11.6: System lift polar for prop-off conditions and prop-on conditions at advance ratios of 0.9 and 0.7 as predicted by the analysis tool and measured in experiments of Sinnige et al. [94]. The system lift includes the contribution of the rotor forces.

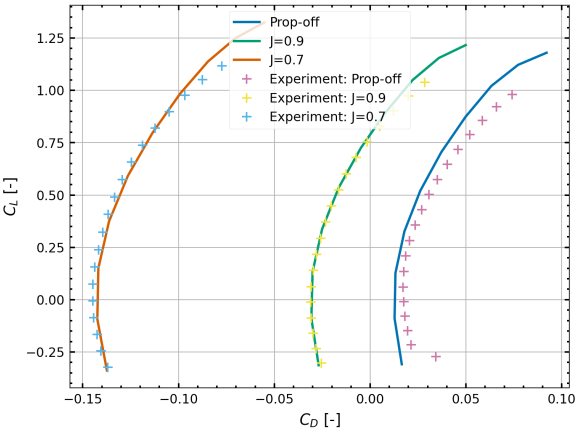

Figure 11.7: System drag polar for prop-off conditions and prop-on conditions at advance ratios of 0.9 and 0.7 as predicted by the analysis tool and measured in experiments of Sinnige et al. [94]. The system drag includes the contribution of the rotor forces.

11.3. Powered high-lift configuration validation & analysis

The numerical analysis tool for a wing with deployed trailing edge flaps deployed is validated to gain confidence in the analysis of ORWF configurations. For this purpose, the results of the same wind tunnel experiments as used in subsection 11.1.1 are used. In this experiment a wall-to-wall unswept and untapered wing with a single-slotted flap and an installed leading edge rotor are used.

11.3.1. Experimental setup

The same wing geometry as described in subsection 11.1.1 is used but with an installed leading-edge open rotor at the spanwise center of the wing. The open rotor used was the TUD-XPROP-S reference propeller with a diameter of $203.2mm$, resulting in a diameter-to-chord ratio of approximately 0.7 with the nested chord length as reference chord. The rotor is positioned 58% chord length in front of the leading edge at an incidence angle of 5 degrees downwards with respect to the flap retracted chord line. Furthermore, the blade pitch was set at 30 degrees at the 70% radial location. The experiments are ran at an advance ratio of 0.8, corresponding to a high thrust case, and an advance ratio of 1.0 corresponding to a medium thrust case. The comparison is performed with a 30 degree flap deflection, 0% overlap and 3% gap length with respect to the nested chord length. The experiments used for this validation were ran at a Reynolds number of $5e6$ and at an advance ratio of 1.0. The measurements were taken over an angle of attack range between -5 and 14 degrees. The geometry of the model with the rotor installed and flaps retracted is shown in Figure 11.8.

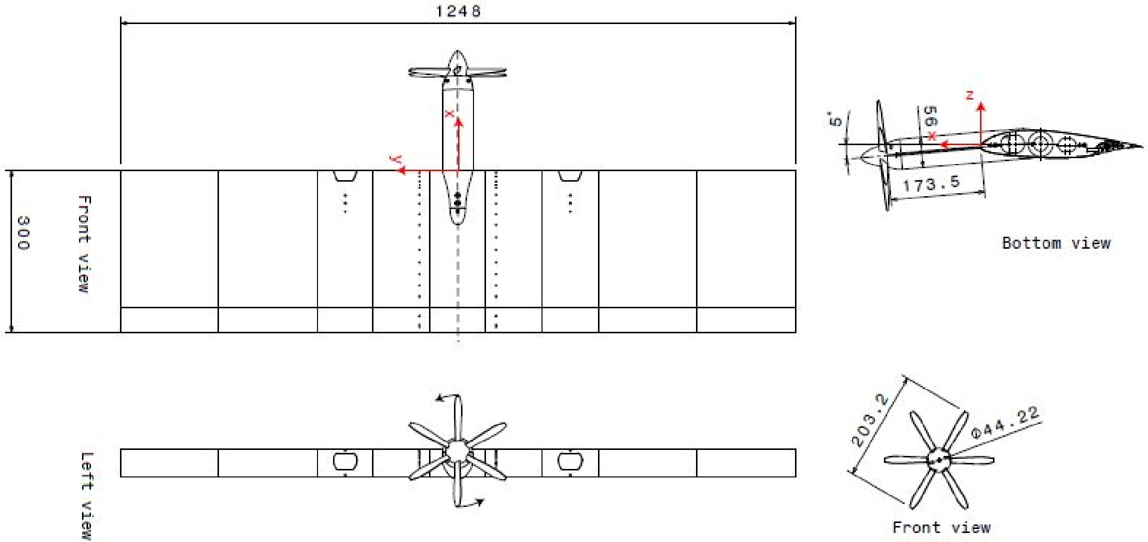

Figure 11.8: Wing geometry of the experiments of Duivenvoorden et al. [64]. The configuration with the rotor detached is used for the present validation of the unpowered high-lift configuration.

11.3.2. Sectional lift coefficient comparison

The lift polar for the rotor-on case with an advance ratio of 1.0 is shown in Figure 11.9 together with the integrated lift coefficients of the experiment at the 87% radius spanwise locations. The sectional lift for the blade-up going side (negative y) is observed to match very well with the sectional lift coefficient of the experiments between an angle of attack of -5 degrees and 2.5 degrees. The lift curve slope, and therefore lift augmentation, is shown to agree with the experiments at these angles. The sectional lift coefficient at the down-going blade side is shown to be structurally overpredicted, although the lift curve slope is also in agreement with the experiments between 0 and 4 degrees angle of attack.

The spanwise lift distribution of the total wing and of each element for angle of attack of 4 degrees is shown in Figure 11.9. In agreement with the lift polar, the lift at the blade up-going side is shown to match well with the experiments. The lift at the down-going blade side is shown to have a local

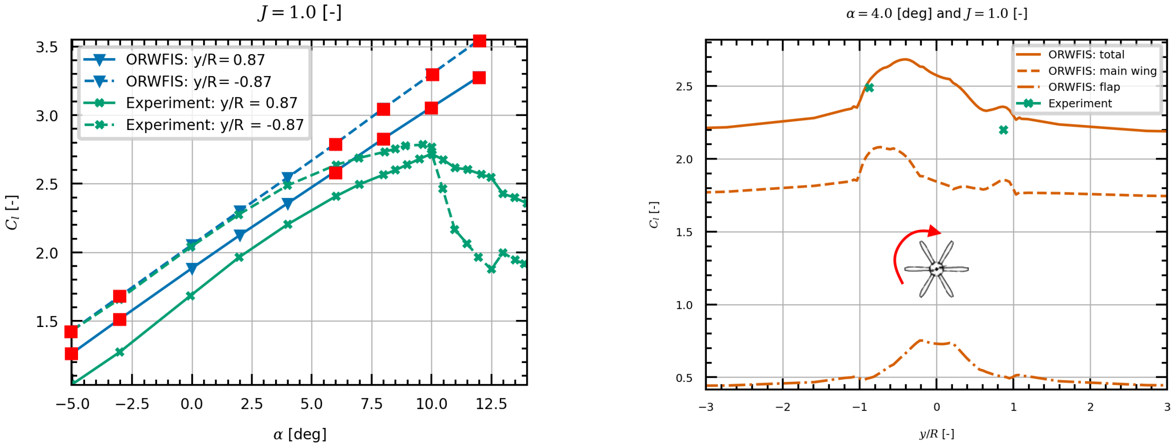

Figure 11.9: Sectional lift polar (left) and spanwise lift distribution (right) for prop-on conditions with an advance ratio of 1.0 as predicted by the analysis tool and as measured in the experiments of Duivenvoorden et al. [64]. Red square markers indicate solutions at which MSES was not able to converge.

maximum, indicating that the jet effect is predicted to counteract and overcome the swirl effect by ORWFIS while this is not the case for the experimental value. One other notable observation can be made from the lift distribution in Figure 11.9, which is the unconventional shape on the flap. Instead of observing lift peaks at the slipstream boundary, the maximum lift is at the spanwise center of the slipstream location. This is because the flap deflection causes it to extend radially outward towards the bottom of the slipstream, moving it out of the low velocity zone caused by the hub. The swirl effect is also reduced because of the position of the flap in the lower half of the slipstream. This is supported by observing the increase in jet velocity at the flap in the center of the wing in Figure 11.10. The swirl velocity is also shown to decrease at the flap here. The overprediction of the lift at the down-going blade side is, therefore, attributed to the reduction in swirl effect on the flap. Considerable slipstream distortion was observed by Duivenvoorden et al. [64] which is not captured by ORWFIS, resulting in an overestimation of the lift on the flap.

One other reason for the discrepancy could be due to the sensitivity of the local lift coefficient to the relative position within the slipstream. The slipstream is observed in this experiment as well as in various other experiments [34, 35, 24, 36, 16, 31] to shear in opposing direction on both the upper and lower surface These effects therefore cause considerable three-dimensional effects which makes a comparison with sectional (two-dimensional) results of ORWFIS difficult.

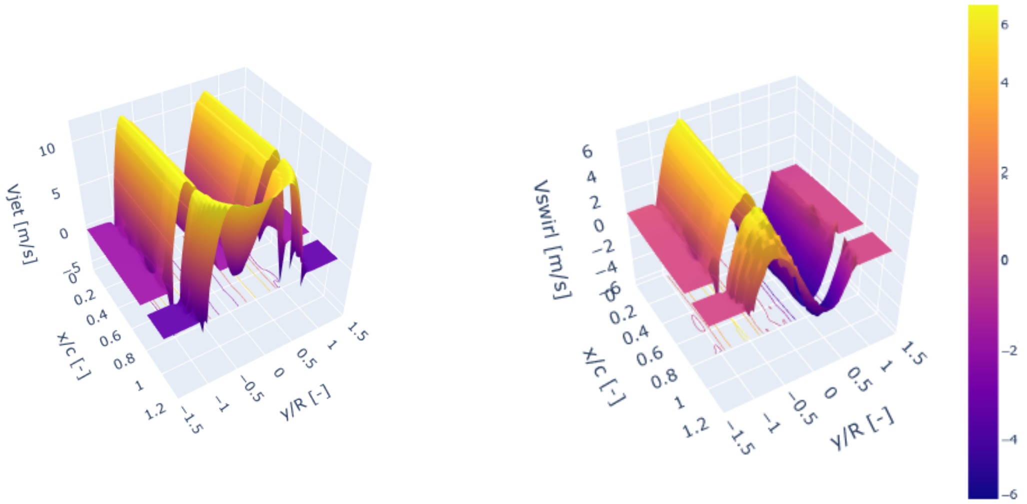

Figure 11.10: Slipstream induced velocities (jet (left) and swirl (right)) distribution over the wing and flap surface for an advance ratio of 1.0 at an angle of attack of four degrees.

12

Effect of rotor-wing coupling

Not only does a leading edge rotor have an influence on a trailing wing, the wing also has an influence on the rotor and consequential slipstream. The wing induced velocities provide an upwash effect on the rotor disk. The slipstream and, therefore, the induced velocities are wing are changed as well. The importance of the feedback coupling of the wing on the rotor is investigated in this chapter. The solution of an ORWF configuration with full interaction coupling is compared to a solution with one-way coupling between the rotor and wing. The investigation is performed on the ORWF geometry described in section 11.3 with a 30 degree flap deflection and a rotor incidence angle of 5 degrees pitch down. The surface exclusive application of the finite slipstream correction is used for this purpose. An angle of attack of five degrees and advance ratio of 1.0 is chosen as operating conditions.

The difference in the rotor effective angle of attack, thrust, and normal force between the one-way coupling and full-interaction coupling is shown in Table 12.1. The effective angle of attack of the one-way coupling solution is zero because the incidence angle of the rotor is -5 degrees with respect to the wing whilst the wing angle of attack is at exactly 5 degrees. It can be seen that the effective angle of attack of the rotor increases considerably by 4.4 due to the induced velocities of the wing and flap. As a result, the thrust increases as the rotor angle of attack increases which corresponds to the observations in literature [28]. Furthermore, the normal force is observed to increase, albeit minimally, due to the increased angle of attack. The increase in normal force due to the induced velocities of a trailing wing also corresponds to what is observed in literature [24, 16].

Table 12.1: Rotor forces for one-way coupling and full-interaction coupling of the rotor and wing in ORWFIS at an angle of attack of 5 degrees and an advance ratio of 1.0.

Rotor-wing coupling mode	$\alpha_{r_{eff}}$ [deg]	C_T [-]	C_Z [-]
One-way coupling	0.0	0.2023	0.0
Full interaction coupling	4.4	0.2051	0.0010

The spanwise lift distribution at an angle of attack of five degrees for both the one-way coupling and full-interaction coupling solution is shown in Figure 12.1. It can be noticed that the peaks of the lift coefficient at both the up-going blade side (negative y) and down-going blade are shifted radially outwards in combination with the reduction in lift at the slipstream center. The effective angle of attack increase on the rotor increases the azimuthal variation of blade circulation, with increased circulation on the rotor at the down-going blade side and decreased circulation at the up-going blade side. This asymmetric circulation distribution rotates in the slipstream model as it progresses along the slipstream axis towards the wing. The increased circulation azimuthal region of the slipstream is in the positive-y direction between the 20% and 60% chord location which covers the quarter-chord location of the wing. The increased circulation at the positive-y side could, therefore, be attributed to the increased slipstream circulation here. The increased slipstream circulation at the slipstream boundary increases the trailing vortex strength. The increased trailing vortex strength induces a downwash at the rotor center, which reduces the lift in this region.

Overall, the lift augmentation of the full interaction is lower than for the one-way coupling which agrees with the observations by Veldhuis [16]. Concluding, the full interaction has a non-negligible effect on the rotor and wing forces for a wing with deflected flaps and a closely-coupled rotor.

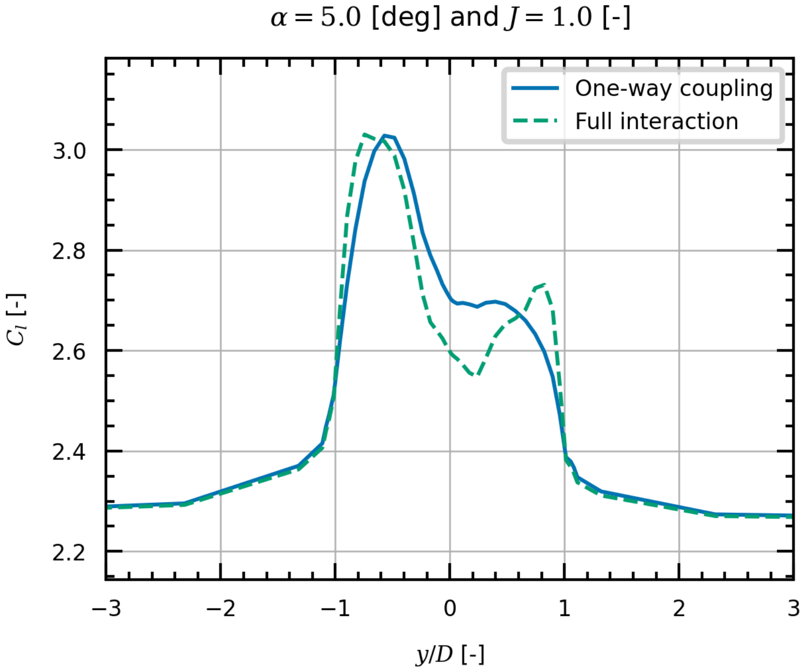

Figure 12.1: Spanwise lift distribution of an analysis with one-way coupling and full interaction coupling between a rotor and a flapped wing.

13

Conclusions & recommendations

The conclusions and recommendations following from the research are presented in this chapter. The conclusions are outlined in section 13.1 and the recommendations are outlined in section 13.2.

13.1. Conclusions

The rapid increase in air traffic and stringent environmental targets necessitates radical new aircraft configurations that are quieter, environmental friendly, and capable of landing on regional airports to relieve the major European hubs. With these radical new aircraft configurations, new physics-based analysis methods are needed to aid in the research and design. The present research focused on the aerodynamic analysis of a configuration with a tractor open rotor and a trailing wing with a flap, promptly called the Open Rotor-Wing-Flap (ORWF) configuration. The complex interactions present between the different elements in an ORWF configuration require a novel analysis method that is able to capture the governing aerodynamic phenomena while remaining relatively fast to solve. The objective of the research was, therefore:

> **”To develop and evaluate an aerodynamic analysis tool for an open rotor-wing-flap configuration by the use of low-fidelity aerodynamic methods”**

For this purpose, the Open Rotor-Wing-Flap Interaction Solver (ORWFIS) analysis tool has been developed. ORWFIS is a quasi-3D viscous analysis tool for ORWF configurations consisting of five coupled analysis modules, each analysing an element of the ORWF configuration. The rotor is analyzed using a vortex based Blade Element method with a modification to allow for non-uniform inflow. The slipstream is modeled by vortex tube derived from the circulation distribution on the rotor. The wing is modeled by a custom developed vortex ring lattice method (VLM) coupled to the two-dimensional viscous solver for multi-element airfoils MSES with a novel decamber method. The main research question is answered using the developed analysis tool which states:

> **”How well can low-fidelity aerodynamic analysis methods predict the lift and drag augmentation of an open rotor-wing(-flap) configuration?”**

One of the sub-questions derived from this question is regarding how the rotor, wing and flap could be coupled in the developed analysis method. The influence of the slipstream on the wing was able to be captured using the combination of the induced velocities of the vortex tube model with the finite slipstream correction applied. It was observed that the finite slipstream correction has a major influence on the accuracy of the lift distribution. Without such a correction, the lift is greatly overestimated. In the present method a finite slipstream correction using a full 3D image method based on a lifting line solution was used. It was observed that the finite slipstream correction method is highly sensitive to differences between the lifting line model of the finite slipstream correction method and the vortex model on which it is applied. The original correction led to erroneous results on the flap as it was not in-plane with the main wing. By modifying the original method to allow for non-planar evaluations of the corrective downwash satisfying results were achieved but minor discrepancies remained on the flap. The discrepancies are expected to grow as the flap positions deviate more from the planar assumption. This reveals the need for a VLM based formulation of the finite slipstream correction instead for an accurate prediction of the lift over a wide range of flap positions.

The coupling of the rotor with the wing also included the feedback of the induced velocities on the rotor and slipstream. The effect of the wing on the rotor could be captured by calculated the wing induced velocities at discrete radial and azimuthal stations on the rotor disk to account for the upwash profile of the wing. The effect of the wing was further coupled to the slipstream by vertically deflecting the slipstream according to the wing induced velocities calculated at the center of the slipstream axis for different axial positions.

The coupling between the rotor and the slipstream to the wing in a 'one-way' fashion was compared with the coupling between the rotor, slipstream and wing in a 'two-way'/'full-interaction' fashion. This revealed that the effect of the wing on the rotor and slipstream are not to be neglected for a wing with a deflected flap as the wing considerably increased the effective angle of attack of the rotor from -1 degrees to 9 degrees. The upwash at the rotor was seen to increase the rotor thrust and normal force, while decreasing the lift augmentation on the wing and flap.

Following the development of the method, it was investigated what governing aerodynamic phenomena can be captured by the low-fidelity aerodynamic methods.

The dynamic pressure effect and the swirl effect of the slipstream on the wing and flap are both able to be predicted by ORWFIS as was observed in the lift distributions of the wing. The dynamic pressure effect is shown to increase the lift coefficient at both the up-going and down-going blade side. The swirl further amplified the lift at the up-going blade side. At the down-going blade side, the swirl effect almost equally opposed the jet effect for the analysed geometry, resulting in a value close to the unpowered lift. However, this is not in general expected to be case and is dependent on the specific rotor characteristics. For a configuration with a deflected flap it was shown that the flap experiences much greater slipstream induced velocities in the axial direction at the center of the rotor as the flap turns radially outward of the minimum velocity area caused by the rotor hub. The swirl effect was also reduced on the flap as the flap was positioned within the lower side of the slipstream. This was shown to give a more constant lift distribution on the flap within the slipstream than for the main wing in which the axial and swirl velocities vary greatly along the span as its radial position within the slipstream changes. Furthermore, the slipstream is shown to deflect near the trailing edge and behind the wing due to the circulation of the wing and flap. However, the distortion of the slipstream shape is not able to be captured due to the limitations of the slipstream tube model which requires its cylindrical shape to be kept.

The thickness effects in multi-element airfoils were shown to have a considerable higher effect on the lift compared to single-element airfoils. The thickness of the elements has a greater effect on the lift due to the circulation effects between the main element and flap element which amplify the thickness-induced lift increase. Methods not accounting for the thickness, such as is the case for stand-alone Vortex Lattice Methods (VLM), are unable to correctly predict the lift of multi-element airfoils. However, in the present method was the thickness effect successfully captured by correcting the VLM with a novel decamber method through the coupling with MSES.

The effects of the slipstream on the viscous solutions were only accounted for by forcing transition at the leading edge in MSES. The original MSES is not able to account for the complex slipstream profiles observed in the tool and their effects on the boundary layer, signifying the limitations of a standard two-dimensional viscous solver in a slipstream. The decamber effect at higher angles of attack was shown to be correctly implement by the decamber method using the solution of MSES solution. The lift curve slope for a wing with retracted flaps was observed to decrease at higher angles of attack due to the decamber effect calculated by MSES. However, the stall point was unable to be predicted as MSES was not able predict this point as well. MSES was also not able to converge at angles of attack close to stall for the wing with a deflected flap, preventing ORWFIS to obtain solutions at these angles. The decamber method is, therefore, as good as the solutions of MSES its given. MSES is, therefore, a major limiter in the performance of the developed method for both the unpowered and powered case.

Finally, the capability of the developed method to predict the lift and drag augmentation was researched by comparing the predictions with experimental results.

The total system lift (including rotor contributions) of a configuration with a wing with flaps retracted and a leading edge rotor was validated by comparing with an experimental dataset. The lift was shown to have been reasonably well predicted up to angles of attack close to the stall angle of attack using the developed low-fidelity analysis tool. The discrepancies reduced at higher angles of attack, meaning that the decamber method is effective in capturing the effects that become dominant at higher angles. The analysis tool was restricted in its prediction for the stall angle of attack by MSES because it was unable to converge around stall and because it is unable to capture the resistance against separation due to the slipstream-induced boundary layer alterations. The predictions of the total system drag (including rotor contributions) of a wing with flaps retracted and a leading edge rotor were shown to have minor discrepancies with the experimental values. The drag was observed to be slightly underestimated for the unpowered configuration which is attributed to negligence of nacelle modelling. However, the drag is shown to predict more closely to the experimental values at higher thrust values. This is attributed to the overestimation of the drag in the powered configurations cancelling the underestimation of the drag in the unpowered case. The drag overestimation for the powered case is attributed to the inability of MSES to account for the delayed flow separation within the slipstream.

The sectional lift curve slopes at both the up-going blade side and down-going blade side were shown to match well with the experimental results for an angle of attack up to 4 degrees. The lift curve slope was overestimated at higher angles of attack due to the inability of MSES to converge here. The absolute lift was shown to match well with the blade-up going side but was overpredicted at the blade down-going side. This is partly attributed to the lack of slipstream distortion modelling which causes the lift on the flap to be overestimated. Furthermore, the shearing and distortion of the slipstream make it difficult to compare local sectional lift coefficients as it causes the sections to be in different positions within the slipstream for both the upper and lower side compared to the cylindrical slipstream model of ORWFIS.

13.2. Recommendations

The present thesis revealed certain areas for future research. The slipstream distortion over a wing with deployed flaps was shown to be cause the slipstream to deform considerably from its circular shape. Further efforts could, therefore, be made in the development of a slipstream model which is able to distort its shape as well as deflect and contract. The effect of the distortion on the spanwise lift distribution could then be investigated as well, to which the accuracy of the present cylindrical method could be quantified. It is also further recommended to investigate finite slipstream corrections based on a non-planar VLM instead of a lifting-line method which is able to perform well over a wider range of flap positions and deflections and is able to account for larger chordwise variations in jet velocity.

Another area of further research recommended would be the evaluation of a non-uniform slipstream on a two-dimensional airfoil to investigate the effects of a non-uniform slipstream on the boundary layer and lift distribution. This could be further expanded into research on a two-dimensional viscous method which is able to capture the slipstream effects while being compatible with an inviscid-viscous coupling scheme connected to a three-dimensional finite slipstream corrected method such as in the present method.

Bibliography

[1] Anon. *ACARE*. Report. Advisory Council for Aviation Research and Innovation in Europe, 2017.

[2] R. Henke, T. Lammering, and E. Anton. “Impact of an Innovative Quiet Regional Aircraft on the Air Transportation System”. In: *Journal of Aircraft* 47.3 (2010), pp. 875–886. DOI: `10.2514/1.45785`. URL: `https://arc.aiaa.org/doi/abs/10.2514/1.45785`.

[3] S. Biser et al. “Design Space Exploration Study and Optimization of a Distributed Turbo-Electric Propulsion System for a Regional Passenger Aircraft”. In: *AIAA Propulsion and Energy 2020 Forum*. Virtual Event, Aug. 2020. DOI: `10.2514/6.2020-3592`. URL: `https://arc.aiaa.org/doi/abs/10.2514/6.2020-3592`.

[4] T. Sinnige. *Provisional PhD research task mr. Bo Zhang*. Report. Delft University of Technology, 2020.

[5] M. D. Moore. “Misconceptions of Electric Aircraft and their Emerging Aviation Markets”. In: *52nd Aerospace Sciences Meeting*. National Harbor, MD, USA, Jan. 2014. DOI: `10.2514/6.2014-0535`. URL: `https://arc.aiaa.org/doi/abs/10.2514/6.2014-0535`.

[6] M. H. Snyder Jr. and G. W. Zumwalt. “Effects of wingtip-mounted propellers on wing lift and induced drag”. In: *Journal of Aircraft* 6.5 (1969), pp. 392–397. DOI: `10.2514/3.44076`. URL: `https://arc.aiaa.org/doi/abs/10.2514/3.44076`.

[7] L. Miranda and J. Brennan. “Aerodynamic effects of wingtip-mounted propellers and turbines”. In: *4th Applied Aerodynamics Conference*. San Diego, CA, USA, June 1986. DOI: `10.2514/6.1986-1802`. URL: `https://arc.aiaa.org/doi/abs/10.2514/6.1986-1802`.

[8] L. H. Smith Jr. “Wake ingestion propulsion benefit”. In: *Journal of Propulsion and Power* 9.1 (1993), pp. 74–82. DOI: `10.2514/3.11487`. URL: `https://arc.aiaa.org/doi/abs/10.2514/3.11487`.

[9] N. K. Borer et al. “Design and Performance of the NASA SCEPTOR Distributed Electric Propulsion Flight Demonstrator”. In: *16th AIAA Aviation Technology, Integration, and Operations Conference*. Washington, DC, USA, June 2016. DOI: `10.2514/6.2016-3920`. URL: `https://arc.aiaa.org/doi/abs/10.2514/6.2016-3920`.

[10] S. F. Yaros et al. *Synergistic Airframe-Propulsion Interactions and Integrations*. Report NASA/TM-1998-207644. National Aeronautic and Space Administration, 1998. URL: `https://ntrs.nasa.gov/citations/19980055126`.

[11] R. E. Kuhn and J. W. Draper. *An investigation of a wing-propeller configuration employing large-chord plain flaps and large-diameter propellers for low-speed flight and vertical take-off*. Report NACA-TN-337. National Advisory Comittee for Aeronautics, 1954.

[12] D. P. Raymer. *Aircraft design: A conceptual approach*. 2nd edition. AIAA education series. Washington, D.C., USA: American Institute of Aeronautics and Astronautics, Inc., 1989.

[13] J. D. Anderson Jr. *Fundamentals of Aerodynamics*. 6th edition. New York,USA: McGraw-Hill Education, 2017. ISBN: 978-1-259-25134-4.

[14] R. E. Pendley. *Effect of Propeller-Axis Angle of Attack on Thrust Distribution over the Propeller Disk in Relation to Wake-Survey Measurement of Thrust*. Report NACA-WR-L-517. National Advisory Committee for Aeronautics, 1945. URL: `https://ntrs.nasa.gov/citations/19930090927`.

[15] P. F. Yaggy and V. L. Rogallo. *A wind-tunnel investigation of three propellers through an angle-of-attack range from 0 deg to 85 deg*. Report NASA-TN-D-318. National Aeronautics and Space Administration, 1960.

[16] L. L. M. Veldhuis. “Propeller Wing Aerodynamic Interference”. Ph.D. thesis. Delft University of Technology, 2005.

[17] G. J. D. Zondervan. *A Review of Propeller Modelling Techniques Based on Euler Methods*. 1st edition. Delft, The Netherlands: Delft University Press, 1998. ISBN: 9040715688. URL: `http://resolver.tudelft.nl/uuid:e4378fce-7225-4bb7-ba90-6268def61d00`.

[18] H. Glauert. “Airplane Propellers”. In: *Aerodynamic Theory*. 1st edition. Berlin: Springer, 1935, pp 169–360.

[19] C. Alba. “A surrogate-based multi-disciplinary design optimization framework exploiting wing-propeller interaction”. MSc thesis. Delft University of Technology, 2017. URL: `http://resolver.tudelft.nl/uuid:e375fcb7-6c02-48d7-9fee-49b46197370e`.

[20] T. Theodorsen. *Theory of propellers*. 1st edition. New York: McGraw-Hill book company, Inc., 1948.

[21] J. T. Conway. “Exact actuator disk solutions for non-uniform heavy loading and slipstream contraction”. In: *Journal of Fluid Mechanics* 365 (1998), pp. 235–267. ISSN: 0022-1120. DOI: `10.1017/s0022112098001372`.

[22] H. S. Ribner. *Notes on the propeller and slipstream in relation to stability*. Report NACA-WR-L-25. National Advisory Comittee for Aeronautics, 1944. URL: `https://ntrs.nasa.gov/citations/19930092551`.

[23] L. Heidelberg and R. Woodward. “Advanced turboprop wing installation effects measured by unsteady blade pressure and noise”. In: *11th Aeroacoustics Conference*. Sunnyvale, CA, USA, Oct. 1987. DOI: `10.2514/6.1987-2719`. URL: `https://arc.aiaa.org/doi/abs/10.2514/6.1987-2719`.

[24] D. P. Witkowski, A. K. H. Lee, and J. P. Sullivan. “Aerodynamic interaction between propellers and wings”. In: *Journal of Aircraft* 26.9 (1989), pp. 829–836. DOI: `10.2514/3.45848`. URL: `https://arc.aiaa.org/doi/abs/10.2514/3.45848`.

[25] R. E. Kuhn and J. W. Draper. *Investigation of the aerodynamic characteristics of a model wing-propeller combination and of the wing and propeller separately at angles of attack up to 90 degrees*. Report NACA-TR-1263. National Advisory Committee for Aeronautics, 1956.

[26] B. W. McCormick. *Aerodynamics, Aeronautics, and Flight Mechanics*. 2nd edition. USA: John Wiley & Sons, Inc, 1995. ISBN: 0-471-57506-2.

[27] J. Cole, M. Maughmer, and G. Bramesfeld. “Aerodynamic Design Considerations for Tiltrotor Wing Extensions and Winglets”. In: *51st AIAA Aerospace Sciences Meeting including the New Horizons Forum and Aerospace Exposition*. Grapevine, TX, USA, Jan. 2013. DOI: `10.2514/6.2013-1088`. URL: `https://arc.aiaa.org/doi/abs/10.2514/6.2013-1088`.

[28] R. M. A. Marretta. “Different Wings Flowfields Interaction on the Wing-Propeller Coupling”. In: *Journal of Aircraft* 34.6 (1997), pp. 740–747. DOI: `10.2514/2.2252`. URL: `https://arc.aiaa.org/doi/abs/10.2514/2.2252`.

[29] R. E. Kuhn and J. W. Draper. *Investigation of Effectiveness of Large-chord Slotted Flaps in Deflecting Propeller Slipstreams Downward for Vertical Take-off and Low-speed Flight*. Report NACA-TN-3364. National Advisory Comittee for Aeronautics, 1955. URL: `https://ntrs.nasa.gov/citations/19930084526`.

[30] K. P. Spreemann and R. E. Kuhn. *Investigation of the Effectiveness of Boundary-layer Control by Blowing over a Combination of Sliding and Plain Flaps in Deflecting a Propeller Slipstream Downward for Vertical Take-off*. Report NACA-TN-3904. National Advisory Comittee for Aeronautics, 1956. URL: `https://ntrs.nasa.gov/citations/19930084788`.

[31] C. Lenfers, N. Beck, and R. Radespiel. “Numerical and Experimental Investigation of Propeller Slipstream Interaction with active High Lift Wing”. In: *35th AIAA Applied Aerodynamics Conference*. Denver, CO, USA, June 2017. DOI: `10.2514/6.2017-3248`. URL: `https://arc.aiaa.org/doi/abs/10.2514/6.2017-3248`.

[32] R. J. Huston and M. A. Winston. *Propeller Slipstream Effects As Determined From Wing Pressure Distribution Of A Large-Scale Six-Propeller VTOL Model At Static Thrust*. Report NASA-TN-D-1509. National Aeronautics and Space Administration, 1962. URL: `https://ntrs.nasa.gov/citations/19630000659`.

[33] B. W. McCormick Jr. *Aerodynamics of V/STOL Flight*. 1st edition. New York, USA: Academic Press Inc., 1967.

[34] A. S. Aljabri and A. C. Hughes. "Wind Tunnel Investigation of Propeller Slipstream Interaction with Nacelle/Wing/Flap Combinations". In: *AGARD Symposium of Aerodynamics and Acoustics of Propellers*. Toronto, Canada, Oct. 1984.

[35] R. T. Johnson, D. P. Witkowski, and J. P. Sullivan. "Experimental results of a propeller/wing interaction study". In: *SAE Transactions* 100 (1991), pp. 121–130. ISSN: 0096736X, 25771531. URL: `http://www.jstor.org/stable/44547585`.

[36] R. T. Johnston and J. P. Sullivan. "Unsteady wing surface pressures in the wake of a propeller". In: *Journal of Aircraft* 30.5 (1993), pp. 644–651. DOI: `10.2514/3.46393`. URL: `https://arc.aiaa.org/doi/abs/10.2514/3.46393`.

[37] L. Prandtl. *Applications of Modern Hydrodynamics to Aeronatucis*. Report NACA-TR-116. National Advisory Committee for Aeronautics, 1923. URL: `https://ntrs.nasa.gov/citations/19930091180`.

[38] G. Fratello, D. Favier, and C. Maresca. "Experimental and numerical study of the propeller/fixed wing interaction". In: *Journal of Aircraft* 28.6 (1991), pp. 365–373. DOI: `10.2514/3.46036`. URL: `https://arc.aiaa.org/doi/abs/10.2514/3.46036`.

[39] H. Aminaei, A. R. Mostofizadeh, and M. Dehghan Manshadi. "Experimental and numerical study of wing boundary layer behavior in propeller flowfield". In: *Journal of Visualization* 22.3 (2019), pp. 489–503. ISSN: 1343-8875. DOI: `10.1007/s12650-019-00553-w`.

[40] X. Fei, B. German, and M. D. Patterson. "Exploring the Effects of Installation Geometry in High-Lift Propeller Systems". In: *2018 AIAA Aerospace Sciences Meeting*. Kissimmee, FL, USA, Jan. 2018. DOI: `10.2514/6.2018-0277`. URL: `https://arc.aiaa.org/doi/abs/10.2514/6.2018-0277`.

[41] S. J. Miley, R. M. Howard, and B. J. Holmes. "Wing laminar boundary layer in the presence of a propeller slipstream". In: *Journal of Aircraft* 25.7 (1988), pp. 606–611. DOI: `10.2514/3.45630`. URL: `https://arc.aiaa.org/doi/abs/10.2514/3.45630`.

[42] E. Elsaadawy and C. Britcher. "Experimental investigation of the effect of propeller slipstream on boundary layer behavior at low Reynolds number". In: *18th Applied Aerodynamics Conference*. Denver, Colorado, USA, Aug. 2000. DOI: `10.2514/6.2000-4123`. URL: `https://arc.aiaa.org/doi/abs/10.2514/6.2000-4123`.

[43] F. M. Catalano. "On the Effects of an Installed PropellerSlipstream on Wing AerodynamicCharacteristics". In: *Acta Polytechnica* 44.3 (2004), pp. 8–14. DOI: `10.14311/562`. URL: `https://ojs.cvut.cz/ojs/index.php/ap/article/view/562`.

[44] M. Brenckmann. *Experimental investigation of the aerodynamics of a wing in a slipstream*. Report UTIA Technical Note No. 11. Institute of Aerophysics, University of Toronto, 1957.

[45] A. M. O. Smith. "High-Lift Aerodynamics". In: *Journal of Aircraft* 12.6 (1975), pp. 501–530. ISSN: 0021-8669. DOI: `10.2514/3.59830`.

[46] C. P. Van Dam. "The aerodynamic design of multi-element high-lift systems for transport airplanes". In: *Progress in Aerospace Sciences* 38.2 (2002), pp. 101–144. ISSN: 0376-0421. DOI: `10.1016/s0376-0421(02)00002-7`.

[47] L. E. Olson. *Optimization of multi-element airfoils for maximum lift*. Report N79-20044. National Advisory Committee for Aeronautics, 1979. URL: `https://ntrs.nasa.gov/citations/19790011873`.

[48] D. M. Driver and G. G. Mateer. "Wake flow in adverse pressure gradient". In: *International Journal of Heat and Fluid Flow* 23.5 (2002), pp. 564–571. ISSN: 0142-727X. DOI: `10.1016/s0142-727x(02)00152-2`.

[49] B. W. Pomeroy et al. "Study of Burst Wakes in a Multi-Element Airfoil Flowfield". In: *AIAA Journal* 52.4 (2014), pp. 821–831. ISSN: 0001-1452. DOI: `10.2514/1.j052680`.

[50] J. R. Chawner, J. Dannenhoffer, and N. J. Taylor. “Geometry, Mesh Generation, and the CFD 2030 Vision”. In: *46th AIAA Fluid Dynamics Conference*. Washington, DC, USA, June 2016. DOI: `10.2514/6.2016-3485`. URL: `https://arc.aiaa.org/doi/abs/10.2514/6.2016-3485`.

[51] R. H. Stone. “Aerodynamic Modeling of the Wing-Propeller Interaction for a Tail-Sitter Unmanned Air Vehicle”. In: *Journal of Aircraft* 45.1 (2008), pp. 198–210. DOI: `10.2514/1.15705`. URL: `https://arc.aiaa.org/doi/abs/10.2514/1.15705`.

[52] G. Ferraro et al. “Propeller-Wing Interaction Prediction for Early Design”. In: *52nd Aerospace Sciences Meeting*. National Harbor, MD, USA, Jan. 2014. DOI: `10.2514/6.2014-0564`. URL: `https://arc.aiaa.org/doi/abs/10.2514/6.2014-0564`.

[53] B. Bohari et al. “Conceptual Design of Distributed Propellers Aircraft: Non-Linear Aerodynamic Model Verification of Propeller-Wing Interaction in High-Lifting Configuration”. In: *2018 AIAA Aerospace Sciences Meeting*. Kissimmee, FL, USA, Jan. 2018. DOI: `10.2514/6.2018-1742`. URL: `https://arc.aiaa.org/doi/abs/10.2514/6.2018-1742`.

[54] M. D. Patterson and B. German. “Conceptual Design of Electric Aircraft with Distributed Propellers: Multidisciplinary Analysis Needs and Aerodynamic Modeling Development”. In: *52nd Aerospace Sciences Meeting*. National Harbor, MD, USA, Jan. 2014. DOI: `10.2514/6.2014-0534`. URL: `https://arc.aiaa.org/doi/abs/10.2514/6.2014-0534`.

[55] J. A. Cole et al. “Higher-Order Free-Wake Method for Propeller–Wing Systems”. In: *Journal of Aircraft* 56.1 (2019), pp. 150–165. ISSN: 0021-8669. DOI: `10.2514/1.c034720`.

[56] J. T. Hwang and A. Ning. “Large-scale multidisciplinary optimization of an electric aircraft for on-demand mobility”. In: *2018 AIAA/ASCE/AHS/ASC Structures, Structural Dynamics, and Materials Conference*. Kissimmee, FL, USA, Jan. 2018. DOI: `10.2514/6.2018-1384`.

[57] P. L. Pernas. “Effect of Flap Position on Propeller-Wing-Flap Aerodynamic Interaction For Distributed Propulsion Systems”. MSc thesis. Delft University of Technology, 2022. URL: `http://resolver.tudelft.nl/uuid:af6eaed9-906a-4aea-9280-431f0bcb9ceb`.

[58] K. A. Deere et al. “Computational Analysis of a Wing Designed for the X-57 Distributed Electric Propulsion Aircraft”. In: *35th AIAA Applied Aerodynamics Conference*. Denver, CO, USA, June 2017. DOI: `10.2514/6.2017-3923`. URL: `https://arc.aiaa.org/doi/abs/10.2514/6.2017-3923`.

[59] R. Willemsen. “A sensitivity study on the aerodynamic performance of a wingtip-mounted tractor propeller-wing system”. MSc thesis. Delft University of Technology, 2020. URL: `http://resolver.tudelft.nl/uuid:24e1b2a5-1616-48f1-8628-8216c0cbce94`.

[60] M. Drela. *QPROP Formulation*. Report. MIT Aero & Astro, 2006. URL: `https://web.mit.edu/drela/Public/web/qprop/qprop_theory.pdf`.

[61] J. N. Sørensen. *General Momentum Theory for Horizontal Axis Wind Turbines*. 1st edition. Vol. 4. Research Topics in Wind Energy. Switzerland: Springer, 2016. DOI: `10.1007/978-3-319-22114-4`.

[62] S. Goldstein. “On the vortex theory of screw propellers”. In: *Proceedings of the Royal Society of London. Series A, Containing Papers of a Mathematical and Physical Character* 123.792 (1929), pp. 440–465. ISSN: 0950-1207. DOI: `10.1098/rspa.1929.0078`.

[63] N. Van Arnhem et al. “Engineering Method to Estimate the Blade Loading of Propellers in Nonuniform Flow”. In: *AIAA Journal* 58.12 (2020), pp. 5332–5346. DOI: `10.2514/1.j059485`. URL: `https://doi.org/10.2514/1.J059485`.

[64] R. R. Duivenvoorden et al. “Experimental investigation of aerodynamic interactions of a wing with deployed fowler flap under influence of a propeller slipstream”. In: *AIAA AVIATION 2022 Forum*. Chicago, IL, USA. DOI: `https://doi.org/10.2514/6.2022-3216`. URL: `https://arc-aiaa-org.tudelft.idm.oclc.org/doi/10.2514/6.2022-3216`.

[65] J. T. Conway. “Analytical solutions for the actuator disk with variable radial distribution of load”. In: *Journal of Fluid Mechanics* 297.-1 (1995), pp. 327–355. ISSN: 0022-1120. DOI: `10.1017/s0022112095003120`.

[66] J. Katz and A. Plotkin. *Low-Speed Aerodynamics*. 2nd edition. New York, NY, USA: Cambridge University Press, 2001. ISBN: 978-0-521-66552-0.

[67] W. Bissonnette and G. Bramesfeld. “Effects of Wake Shapes on High-Lift System Aerodynamic Predictions”. In: *54th AIAA Aerospace Sciences Meeting*. San Diego, CA, USA, Jan. 2016. DOI: `10.2514/6.2016-2040`. URL: `https://arc.aiaa.org/doi/abs/10.2514/6.2016-2040`.

[68] D. O. Phillips W. F. a. S. “Modern Adaptation of Prandtl’s Classic Lifting-Line Theory”. In: *Journal of Aircraft* 37 (2000), pp. 662–670. DOI: `10.2514/2.2649`.

[69] L. L. M. Veldhuis and P. M. Heyma. “Aerodynamic optimisation of wings in multi-engined tractor propeller arrangements”. In: *Aircraft Design* 3.3 (2000), pp. 129–149. ISSN: 1369-8869. DOI: `10.1016/s1369-8869(00)00010-0`.

[70] M. Drela and H. Youngren. *AVL 3.40 User Primer*. 2022. URL: `https://web.mit.edu/drela/Public/web/avl/avl_doc.txt`.

[71] XFLR5. *XFLR5: analysis tool for airfoils, wings and planes operating at low Reynolds numbers.* URL: `http://www.xflr5.tech/xflr5.htm`.

[72] T. W. Feistel, V. R. Corsiglia, and D. B. Levin. “Wind-Tunnel Measurements of Wing-Canard Interference and a Comparison with Various Theories”. In: *Business Aircraft Meeting & Exposition*. Wichita, KS, USA. DOI: `https://doi.org/10.4271/810575`. URL: `https://doi.org/10.4271/810575`.

[73] I. Abbott and A. E. Von Doenhoff. “Theory of wing sections, including a summary of airfoil data”. In: 1st edition. New York: Dover Publications, Inc., 1959, p. 53.

[74] R. Nederlof. “Improved modeling of propeller-wing interactions with a lifting-line approach”. MSc thesis. Delft University of Technology, 2020. URL: `http://resolver.tudelft.nl/uuid:d952665d-475f-483d-94f5-2b929ea6e713`.

[75] S. C. Rethorst. “Aerodynamic of Nonuniform Flows as Related to an Airfoil Extending Through a Circular Jet”. In: *Journal of the Aerospace Sciences* 25.1 (1958), pp. 11–28. DOI: `10.2514/8.7479`. URL: `https://arc.aiaa.org/doi/abs/10.2514/8.7479`.

[76] R. K. Prabhu. “Studies on the interference of wings and propeller slipstreams.” Ph.D. thesis. Indian Institute of Science, 1984.

[77] M. Drela. “Newton solution of coupled viscous/inviscid multielement airfoil flows”. In: *21st Fluid Dynamics, Plasma Dynamics and Lasers Conference*. Seatle, WA, USA. DOI: `10.2514/6.1990-1470`. URL: `https://arc.aiaa.org/doi/abs/10.2514/6.1990-1470`.

[78] M. Drela and M. B. Giles. “Viscous-inviscid analysis of transonic and low Reynolds number airfoils”. In: *AIAA Journal* 25.10 (1987), pp. 1347–1355. ISSN: 0001-1452. DOI: `10.2514/3.9789`.

[79] J. L. v. Ingen. *A suggested semi-empirical method for the calculation of the boundary layer transition region*. Report VTH-74. Delft University of Technology, 1956. URL: `http://resolver.tudelft.nl/uuid:cff1fb47-883f-4cdc-ad07-07d264f3fd10`.

[80] J.H.M. Van den Berg B. a. G. *Low-speed surface pressure and boundary layer measurement data for the NLR 7301 airfoil section with trailing edge flap*. Report A9. North Atlantic Treaty Organization, Aug. 1994.

[81] C. P. v. Dam, J. C. V. Kam, and J. K. Paris. “Design-Oriented High-Lift Methodology for General Aviation and Civil Transport Aircraft”. In: *Journal of Aircraft* 38.6 (2001), pp. 1076–1084. DOI: `10.2514/2.2875`. URL: `https://arc.aiaa.org/doi/abs/10.2514/2.2875`.

[82] R. Mukherjee, A. Gopalarathnam, and S. Kim. “An Iterative Decambering Approach for Post-Stall Prediction of Wing Characteristics from Known Section Data”. In: *41st Aerospace Sciences Meeting and Exhibit*. Reno, NV, USA. DOI: `10.2514/6.2003-1097`.

[83] D. Hunsaker and D. Snyder. “A Lifting-Line Approach to Estimating Propeller/Wing Interactions”. In: *24th AIAA Applied Aerodynamics Conference*. San Francisco, CA, USA, June 2006. DOI: `10.2514/6.2006-3466`.

[84] C. Alba et al. “A Surrogate-Based Multi-Disciplinary Design Optimization Framework Exploiting Wing-Propeller Interaction”. In: *18th AIAA/ISSMO Multidisciplinary Analysis and Optimization Conference*. Denver, CO, USA, June 2017. DOI: `10.2514/6.2017-4329`. URL: `https://arc.aiaa.org/doi/abs/10.2514/6.2017-4329`.

[85] O. Şugar Gabor, A. Koreanschi, and R. M. Botez. “A new non-linear vortex lattice method: Applications to wing aerodynamic optimizations”. In: *Chinese Journal of Aeronautics* 29.5 (2016), pp. 1178–1195. ISSN: 1000-9361. DOI: `https://doi.org/10.1016/j.cja.2016.08.001`. URL: `https://www.sciencedirect.com/science/article/pii/S1000936116300954`.

[86] B. Van den Berg. *Boundary layer measurements on a two-dimensional wing with flap*. Report NLR TR 79009 U. National Aerospace Laboratory NLR, 1979.

[87] P. Zelst. “2D modeling approach for propeller-wing-flap interaction”. MSc thesis. Delft University of Technology, 2021. URL: `http://resolver.tudelft.nl/uuid:c5c1c090-6cd2-4134-8575-3adaf4d6bb90`.

[88] I. Abbott and A. E. Von Doenhoff. *Theory of wing sections, including a summary of airfoil data*. 1st edition. New York: Dover Publications, Inc., 1959.

[89] L. Boermans and P. Rutten. *Two-dimensional aerodynamic characteristics of airfoil NLF-MOD22 with fowler flap.* Report. Delft University of Technology, 1995.

[90] H. J. Allen and W. G. Vincenti. *Wall interference in a two-dimensional-flow wind tunnel, with consideration of the effect of compressibility*. Report NACA Technical Report 782. National Advisory Committee of Aeronautics, 1944.

[91] J. G. Coder, M. D. Maughmer, and D. M. Somers. “Theoretical and Experimental Results for the S414, Slotted, Natural-Laminar-Flow Airfoil”. In: *Journal of Aircraft* 51.6 (2014), pp. 1883–1890. DOI: `10.2514/1.c032566`.

[92] D. P. Coiro, F. Nicolosi, and F. Grasso. “Design and Testing of a Multi-Element Airfoil for Short-Takeoff-and-Landing Ultralight Aircraft”. In: *Journal of Aircraft* 46.5 (2009), pp. 1795–1807. DOI: `10.2514/1.43429`. URL: `https://arc.aiaa.org/doi/abs/10.2514/1.43429`.

[93] Z. T. Applin and G. L. Gentry Jr. *Experimental and theoretical aerodynamic characteristics of a high-lift semispan wing model*. Report NASA-TP-2990. NASA Langley Research Center, 1990. URL: `https://ntrs.nasa.gov/citations/19900010730`.

[94] T. Sinnige et al. “Wingtip-Mounted Propellers: Aerodynamic Analysis of Interaction Effects and Comparison with Conventional Layout”. In: *Journal of Aircraft* 56.1 (2019), pp. 295–312. ISSN: 0021-8669. DOI: `10.2514/1.c034978`. URL: `https://doi-org.tudelft.idm.oclc.org/10.2514/1.C034978`.